THE FLORIDA STATE UNIVERSITY

COLLEGE OF ARTS AND SCIENCES

MODEL STUDIES OF BLOCKING PREDICTABILITY USING THE ADJOINT SENSITIVITY FORMALISM

By

MANUEL S. F. V. DE PONDECA

A Dissertation submitted to the
Department of Meteorology
in partial fulfillment of the
requirements for the degree of
Doctor of Philosophy

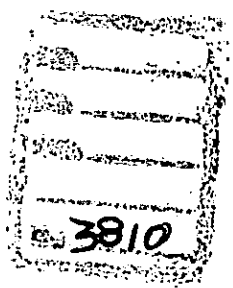

Degree Awarded:
Summer Semester, 1996

The members of the Committee approve the dissertation of Manuel S. F. V. de Pondeca defended on May 1, 1995.

Albert I. Barcilon
Professor Directing Dissertation

Jon E. Ahlquist
Committee Member

James B. Elsner
Committee Member

Jerry F. Magnan
Committee Member

Richard L. Pfeffer
Committee Member

Xiaolei Zou
Committee Member

I dedicate this dissertation to the memory of my father, Jossias F. Pondeca.

Acknowledgements

It is a pleasure to thank Dr. Albert Barcilon for his guidance as my major professor and stimulating interest throughout this work. I thank my committee members for valuable comments concerning the prospectus that preceded this dissertation. Special gratitude is due to Dr. Mark Borges for helpful comments regarding the 3-dimensional instability calculations. I am also grateful to Dr. Jeffrey Whitaker for providing the nonlinear model and making valuable comments regarding this work. The linear model and its adjoint were developed by Dr. Xiaolei Zou, who kindly put them to my disposal. I also acknowledge very gratefully the discussions that I had with Dr. Zou concerning the use of the adjoint sensitivity technique in this work. The assistance of Dr. Melvin Shapiro in evaluating the realistic nature of the nonlinear model output is gratefully acknowledged. I extend my gratitude to Scott Applequist for his diligent proof-reading of the manuscript.

The author was sponsored by the FINNIDA/WMO/SADC Meteorology Project, based in Maputo, Mozambique. Additional support came from the National Science Foundation Grant ATM-9415407. A significant part of this research was carried out in Boulder, Colorado, during the author's visit appointments with the Mesoscale and Microscale Meteorology Division of the National Center for Atmospheric Research (NCAR), and the Cooperative Institute for Research in the Environmental Sciences (CIRES).

TABLE OF CONTENTS

LIST OF TABLES

LIST OF FIGURES

Abstract

Adjoint sensitivity calculations of a blocking index to the sets of normal modes, adjoint modes and singular vectors growing on instantaneous basic state flows that precede the onset of blocks are performed. A two-layer isentropic primitive equation model on the hemisphere is used. The blocking index is a normalized L_2 dot product of the daily flow anomalies with a "mean blocking pattern." Two case studies are performed. The first case study features a block contained in the control run, while the second features a block excited by superposing a perturbation onto the control run during a period of time free of blocks.

A convenient method of evaluating the sensitivities is presented. The method is based on expanding the initial condition in terms of the structures of each set, whereby the concept of projectability of the normal modes is naturally incorporated. It is found that the mechanism of initial growth, which is distinct from that of the usual exponential growth, has to be taken into account in theories of error growth based on normal modes. The singular vectors are found to form the best set of precursors for the transition to blocks in a 3 to 4 day ensemble forecast. Extensions of the range of predictability to 6 days require proper account of nonlinearities in any optimization scheme designed to provide the perturbations of the ensemble.

It is proposed that the blocks presented in both case studies develop in a two-step manner. The first step features the Thorncroft-Hoskins-McIntyre LC1-type developing troughs, and the second step consists of a rapid intensification of the blocking ridge by exponential

growth of the leading normal modes.

CHAPTER 1

Introduction

1.1 Motivation

Following Baines (1983), "*Blocking may be loosely defined as consisting of a stationary synoptic feature (or features) which lasts at least several days, around which the westerly airstream with its own embedded synoptic structure is deflected. The stationary feature may take the form of a single ridge or anticyclone, but more commonly and significantly it consists of a cyclone-anticyclone pair oriented north-south.*" The buildup and maintenance of atmospheric blocking have been studied for almost a half century. The simple and somewhat disappointing reality that there is no universally accepted theory should perhaps be regarded as an indication of the existence of a variety of different physical processes by which a blocked state can be excited and maintained.

The inability of numerical models to correctly predict the transition to the blocked state and, to some extent, its duration, results in anomalies from the mean climate on time-scales of a week to a season. In studies aimed at assessing the skill of the ECMWF operational model, Tibaldi and Molteni (1990) found that the frequency of blocking is severely underestimated in medium-range forecasts. The numerical model consistently misses the onset of the block beyond forecast day 3 to 4. It shows reasonable skill when the block is already in the initial conditions, but again, it underestimates the duration of the episode.

Furthermore, the model tends to shift Euro-Atlantic blocks progressively eastward, while it shifts the Pacific blocks westward, with an accompanying loss of amplitude in both sectors, but mainly in the Pacific. This inability of the model to reproduce the observed blocking frequency maxima at the preferred longitudes directly impacts on the climate of the model, contributing to what is known as model climate drift. The latter denotes the tendency of Global Circulation Models to move towards a climate of "their own," characterized by increased mid-latitude westerlies and decreased amplitude of planetary scale quasi-stationary waves (*e.g.* Bettge 1983). Further work is thus needed to understand what processes initiate, maintain and destroy the blocked state. This research contributes towards that goal. By using a two-layer hemispherical model and the technique of the adjoint sensitivity analysis, we explore the theory of barotropic and baroclinic instability of three-dimensional basic state flows for the onset of blocking (Frederiksen 1982, 1983, 1984, 1989).

1.2 The Phenomenon of Blocking

Blocking was reported for the first time by Garriot (1904). Fig. 1, taken from Ji and Tibaldi (1983), represents a snapshot of the mature stage of an Atlantic block which took place during December 1978. Shown is the ECMWF FGGE analysis of the 500mb geopotential height field for 0000 GMT 25 December. A sharp transition in the westerlies from a zonal type to a meridional type is observed, with a blocking high established east of Greenland, around 30°W, 70°N, and a blocking cyclone south of it, at around 50°N.

Blocking occurs in preferential geographical locations. These are the northeast Atlantic and Pacific oceans in the Northern Hemisphere, and the eastern Australia, the Scotia Sea

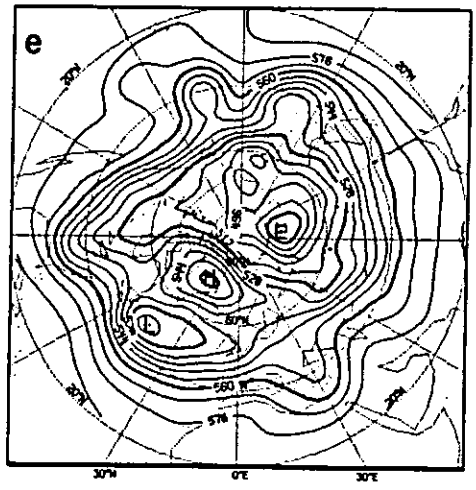

Figure 1: ECMWF FGGE analysis of 500 mb geopotential height for 0000 GMT 25 December. Isopleths are drawn every 8 dam. Taken from Ji and Tibaldi (1983).

and the region between Marion and Crozet Islands in the Southern Hemisphere.

Although it is a phenomenon which can be observed in all four seasons, blocking development shows a strong seasonal variability. For instance, Pacific blocks in the Northern Hemisphere have their seasonal maximum in the autumn/winter season (White and Clark, 1975).

Social and economic hardships can occur with spells of weather originated from a blocking situation. When blocking occurs over the Euro-Atlantic sector in the winter, very cold Arctic air to the south of the block often generates intensive small-scale depressions with strong winds and heavy snow-falls. When a block forms near the west coast of the United States, the warm moist air from the Pacific is diverted to the north, causing drought in the western states and high temperatures in the Arctic regions. On the other hand, the

anticyclonic flow associated with the high favors outbreaks of cold polar air to the south over most of the states east of the Rockies. Sometimes the jet is displaced as far south as Florida, causing citrus damage.

1.3 Theories of Blocking. Historical Overview

As more upper air observations became available, numerous observational and theoretical studies of blocking appeared in the literature. Pioneering works include those of Namias (1947), Berggren *et al.*, (1949), Elliot and Smith (1949), Rex (1950a, 1950b, 1951), Yeh (1949), Rossby (1950), van Loon (1956) and O'Connor (1963). For comprehensive reviews of some of the main theories that have been proposed, the reader is referred to Baines (1983) and Frederiksen and Webster (1988).

A good theory ought to explain the most salient features of blocks, namely the splitting of the jet upstream of the ridge, the persistence of the pattern, the preference for certain geographical locations and the strong seasonal dependence.

We describe in this section only briefly some of the main theories of blocking, without mentioning their merits and weaknesses. A critical review is beyond the scope of this work, and can be found elsewhere (*e.g.* Baines 1983, White and Clark 1975, Egger 1978).

Earlier theories where developed within the context of barotropic dynamics. In particular, Rossby (1950) and Rex (1950a,b) suggested that blocks where the rotating analogue of the hydraulic jump of single layer flow in open channels.

Subsequent theories often more distinctly took on either a "*global character*" or, alternatively, a "*local character.*"

In the global theories, the phenomenon is essentially modelled as a planetary wave response to the external forcing by orography and thermal heating. The concept of multiple equilibria was used by Charney and DeVore (1979), Charney and Strauss (1980), Charney, Shukla and Mo (1981), Källan (1982), Mitchel and Derome (1983) and others. Simulations in forced and dissipative barotropic and baroclinic models have shown that for appropriately large forcing, and when the system is close to the linear condition for resonance, two types of stable steady (or quasi-steady) states are possible: states with a high zonal index flow, or, conversely, states with a low zonal index flow, reminiscent of blocks. It is proposed that the time-varying atmosphere may alternate and spend some time in the "attractor basin" of each of these two types of states, a jumping phenomenon which was modelled by Trevisan and Buzzi (1980) through the equation for a nonlinear oscillator.

Nonlinear resonance of orographically and thermally forced planetary Rossby waves (Tung and Lindzen 1979a,b) and nonlinear interaction of forced waves and free waves (Egger 1978) are also some of the theories which concentrate on the large-scale aspect of blocking.

Tung and Lindzen (1979a,b), in an attempt to develop a "unified theory" of blocking and stratospheric sudden warming, were able to show in model studies that the stationarity condition, which is necessary for the resonant buildup of energy, was easily satisfied by a disturbance with a zonal wavenumber 4 under normal wind conditions. Under abnormal conditions (stronger than normal westerlies in the stratosphere and increased negative vertical shears), resonance was also found for wavenumbers 1 and 2. These were suggested to

be instrumental both in the development of blocking and the stratospheric sudden warming. The notion is that long waves amplify in the troposphere when conditions for them to be confined horizontally and vertically are met, so that a resonant forcing by topography and land-sea differential heating can take place. Furthermore, during winter, when the mean flow is favorable for vertical propagation, these waves can penetrate into the stratosphere before they become evanescent, and initiate the process of sudden warming. Shorter waves, such as wavenumber 4, although easier to resonate, are absorbed before reaching the stratosphere, and therefore cannot account for the stratospheric sudden warming. However, because these shorter waves still can be instrumental in the onset of blocking, this fact is used to account for higher frequency of blocking in the atmosphere than the frequency of stratospheric sudden warming.

Egger (1978) proposed that blocking was produced by the nonlinear interaction of forced waves and slowly moving free waves, *i.e.*, waves close to resonance. He showed that in quasi-geostrophic inviscid models on a channel, for properly chosen zonal basic state winds, orographically forced waves were able to interact with quasi-free waves and produce blocking highs, and that these had preferred positions with respect to the orography.

Kalnay-Rivas and Merkine (1981) regarded the initiation of blocking as due to the superposed effects of forced Rossby lee waves. They suggested that an enhancement in a nonlinear "closed flow" region, bearing the structure of a block, could result from the superposition of Rossby lee waves forced in different regions and having the appropriate phase relation.

Conversely, theories which regard blocking as a nonlinear local equilibrium were proposed.

For instance, McWilliams (1980), Baines (1983) and Haines and Marshall (1987) used the concept of solitary wave to explain the maintenance of the blocked state (see also Flierl *et al.*, 1980). Dipole-type solitary solutions were discovered by Stern (1975) and Larichev and Reznik (1976). Their structures are similar to that of a stationary quasi-geostrophic vortex pair, and show a rapidly vanishing amplitude away from the center. Baines (1983) generalized the theory to include thermal forcing to account for the different SST patterns.

The notion that synoptic scale eddies play an important role in the onset and maintenance of the blocked state serves as a motivation for a "local theory." A maintenance mechanism by high-frequency eddies was originally proposed by Green (1977) and further documented and substantiated by Shutts (1983), Illari and Marshall (1983), Hoskins *et al.*, (1985), Hoskins and Sardesmukh (1987) and others. In particular, Shutts (1983) used a barotropic model to demonstrate the compression in the east-west direction and stretching in the north-south direction of cyclone-scale eddies entering the strong deformation field of a pre-existing split-jet. These eddies were also shown to have a bowing configuration in their inclination with respect to each branch of the split-jet, thus resulting in eddy energy and momentum fluxes that counteracted the effects of dissipation and advection on the blocked flow. Shutts (1986) gave additional supporting evidence for the role played by the eddies in a diagnosis of the daily evolution of the isentropic potential vorticity field during a blocking episode.

A conceptually different approach to understanding blocking is based on the inherent hydrodynamical instability of atmospheric flows and of the coupled ocean-atmosphere system.

Namias (1950) postulated that the blocking ridge over the Pacific, in the Northern

Hemisphere, occurred in response to a buildup of cold air over the polar regions that was contained by strong midtropospheric westerlies. The formation of the block acted to discharge this cold air into subtropical regions, thereby maintaining the balance between heat gain at the equator and heat loss at the poles. In modern terminology, this is equivalent to stating that the blocking ridge is a manifestation of baroclinic instability.

Namias (1959) hypothesized that the mid-ocean blocking ridge could be a fundamental unstable mode of the coupled ocean-atmosphere system which derives its energy from thermal anomalies contained in the upper ocean.

White and Clark (1975) suggested that baroclinic instability of the atmospheric flow in the presence of sensible heat exchange might be the mechanism triggering blocking over the Pacific, in accordance with an instability study of Haltiner (1967).

More recently, Frederiksen (1982, 1983, 1984, 1989) generalized these ideas in his theory of mixed barotropic and baroclinic instability of three-dimensional flows. According to this theory, the instability of the three-dimensional flow should account not just for the commonly known cyclogenesis, but also for other larger scale phenomena, including blocking.

Observational evidence for the importance of baroclinic processes in the formation phase of blocks was reported by Dole (1986), who noted that anomalous centers developed and intensified with little phase propagation, and with substantial phase tilt with height, indicative of a baroclinic development.

Using hemispheric two-layer and multi-layer models linearized about realistic basic states, Frederiksen (1982, 1983, 1984) found that the meridional structure of the most

unstable mode changes as the flow is dragged closer to the threshold criterion for instability. The familiar monopole structure of classical baroclinic instability gives way to a dipole structure reminiscent of blocking.

Recent trends in the theory of linear instability of atmospheric flows also suggest that structure development may be regarded as an optimal barotropic/baroclinic development (Farrell, 1989).

1.4 Objectives

It appears very unlikely that a simple "unified theory" of blocking can be developed. Rather, the sample works of the preceeding section suggest that a blocked state can be excited by a variety of different mechanisms. Baines' (1981) critical review of the main theories suggests that although some of the proposed mechanisms are not sufficiently substantiated, they should not be singled out, and that different blocks, at different geographical locations, may be caused by distinct mechanisms. It is therefore not the goal of the this research to seek a unique explanation for blocking. Rather, it is aimed at furthering our understanding of the theory of the mixed barotropic and baroclinic instability of three-dimensional basic state flows. It was decided to explore this particular theory because it is the only one which takes into account the inherent unstable nature of atmospheric flows. It appears reasonable to hypothesize that it is a mechanism which often is instrumental in the realization of the blocked state.

Frederiksen (1982,1983,1984,1989) did remarkable work on this subject. However, as noted by Baines (1983), "although the theory is firmly substantiated and explains the

dipole structure and the locality of its occurrence, in a sense, it merely pushes the problem back one step. It is now necessary to identify processes which create the flow which goes unstable in this particular manner in the particular location."

In this investigation, a two-layer isentropic model on the hemisphere is used to gain insights into the dynamics of the onset of blocking. Detailed studies are performed on two episodes. Specifically,

1. The technique of adjoint sensitivity analysis is used to assess the sensitivity of a blocking index to the sets of normal modes, adjoint modes and singular vectors calculated from instantaneous three-dimensional basic state flows several days prior to the onset. The adjoint sensitivity technique is a powerful tool, for the effects of a large number of different initial conditions can be studied in computationally affordable times. The method yields first order values for the changes in the response function which are induced by changes in the initial conditions. In particular, the adjoint sensitivity analysis is used to give an indication of the most adequate set (among the three sets of perturbations mentioned above) of "precursors" for the transition to the blocked state in the context of an ensemble forecast.

2. The analysis of different normal modes is carried out in the light of the initial value problem that could in principle lead to their appearance. A theory of structure development based on normal modes must include an assessment of the chances of such structures actually emerging and being perceived observationally. Characteristic time scales for "the normal mode form achievement" have usually been estimated from their e-folding times. We now know that a more complete analysis has to incorporate the time scale associated with the initial growth. The concept of projectability, introduced by Zhang (1988), is used in this

context.

3. The role of the non-modal growth is assessed. Linear combinations of normal modes which maximize a specific norm over a finite time have been the subject of much attention in recent years (*e.g.* Farrell 1989, Buizza and Palmer 1995). Perturbations found by optimization in a well defined sense are certainly pertinent to the problem of structure development, since observed initial perturbations are of finite amplitude and not infinitesimally small, as assumed in some "normal mode based" approaches. Hence, it is necessary to assess the importance of non-modal growth relative to modal growth in block formation.

4. Different diagnoses in the framework of the PV-thinking are made.

The text is organized as follows:

In Chapter 2, we describe the two-layer isentropic model on the hemisphere. The method of the adjoint sensitivity analysis, including the derivation of the pertaining equations, is presented in Chapter 3. In Chapter 4, we describe the methods used to calculate the normal modes and adjoint modes. The ideas behind the concept of singular vectors are presented in Chapter 5, where we also formulate the equations for the singular vectors. The methodology used to calculate the sensitivity of the response function to the sets of normal modes, adjoint modes and singular vectors is presented in Chapter 6. In Chapter 7, we address the problem of blocking predictability within linear theory. Chapter 8 presents the results for the first case study and Chapter 9 for the second case study. Chapter 10 contains the discussion of the results of both case studies. In Chapter 11, we study the onset of block with initial conditions 6 days prior to the transition. Chapter 12 presents a block excited by mechanisms apparently different from those of case studies 1 and 2. The conclusions are

found in Chapter 13.

CHAPTER 2

The Model

In this study we use a two-layer primitive equation model. It is an isentropic spectral model on the hemisphere truncated at T31, which is driven by a Newtonian relaxation term. It includes a zonal wavenumber 2 orography, dissipation in the lower layer and a horizontal internal ∇^{12} hyperdiffusion. The potential temperatures in the lower and upper-layer were set to $280^{o}K$ and $320^{o}K$, respectively.

The predictive variables are the isentropic vorticity, ζ, the divergence, D, and the Exner-layer thickness, $\Delta\pi$, where $\pi \equiv c_p \left(\frac{p}{p_o}\right)^{R/c_p}$. The Exner-layer thickness can be thought of in terms of the geometric layer thickness. The state vector is the complex vector of all non-zero spectral coefficients of the predictive variables in both layers. Whenever convenient, however, a real state vector will be used. The latter is obtained by treating the real and imaginary parts of the spectral coefficients as distinct elements. Details of the model are given in Appendix A.

The driving is achieved by prescribing an equilibrium interface Exner-function and a relaxation time. The actual interface tends to relax towards the equilibrium (drive state). That approach to equilibrium is disrupted by barotropic and baroclinic instability which stir the eddies. These two competing effects (plus bottom friction and horizontal diffusion) produce the model output.

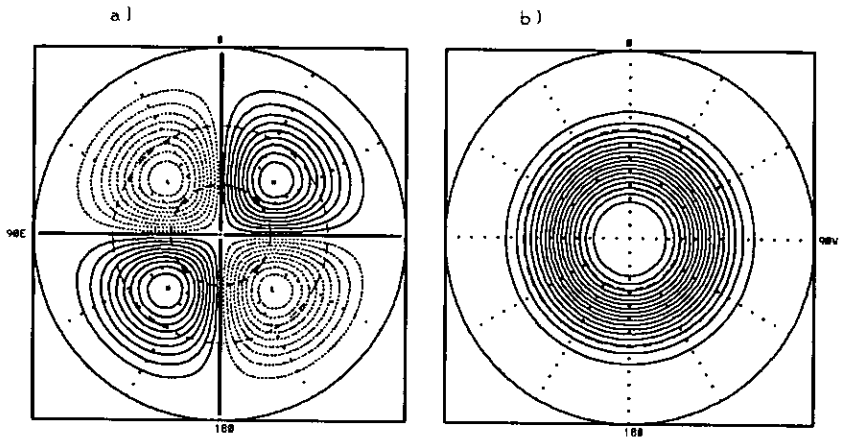

Figure 2: Panel a): Isopleths of the topography. Contour interval 200m. Panel b): Equilibrium interface geometric height for $\pi_\beta = 0.9$. Contour interval 500m. Dashed contours for negative values. The equilibrium interface geometric height increases monotonically with latitude.

The upper surface is a free surface, and the equilibrium interface has a zonal structure, with a north-south slope controlled by the parameter π_β (see Appendix A). As π_β is increased the vertical shear in the drive state increases and the eddies become more vigorous in the model. The mountain has ridges along $135°E$ and $45°W$ and valleys along $45°E$ and $135°W$. The height of the crests is 2000 m. Fig. 2 shows isopleths of the equilibrium interface geometric height for $\pi_\beta = 0.9$ and of the topography. The relation between the geometric height and the Exner-function is given by equation (69), in Appendix A.

The Rayleigh damping in the lower layer has a time scale of 5 days. The hyperdiffusion coefficient was chosen to give a decay rate of $3h^{-1}$ for the smallest retained scale. Terms responsible for gravity wave propagation in the prognostic equations are treated implicitly using the Crank-Nicholson scheme. All other terms are treated explicitly using the leapfrog scheme. A weak time filter is applied to all three prognostic variables to damp the

computational mode.

This model has proved to yield realistic blocking patterns and has been used in previous studies of blocking by Zou *et al.*, (1993). The linearized version of the model and its adjoint were also used in this investigation.

CHAPTER 3

Sensitivity Analysis

3.1 Introduction

The expression "*sensitivity analysis*" denotes the study of changes in a mathematical model output when initial conditions and parameters in the model are changed. The study more particularly focuses on the changes of à selected response function. That function is chosen so as to obtain sensitivity of a particular physical process.

This quantitative procedure is useful in the interpretation of the results of sophisticated and therefore complex models, for which, as it is often the case, the physics underlying the various processes is not well known.

Two alternative formalisms can be found : The *forward sensitivity analysis* and the *adjoint sensitivity analysis*. The former can be used advantageously to ascertain the effects of relatively few alterations in the initial conditions and parameters on many response functions, while the latter is computationally more economical for problems that involve many alterations in the initial conditions and parameters and comparatively few response functions.

We will be concerned with the adjoint sensitivity formalism in this study, but for the sake of completeness, a brief reference to the mathematical meaning of the forward sensitivity analysis will also be made.

3.2 Adjoint Sensitivity Analysis

3.2.1 Generalities

The use of adjoint techniques for sensitivity studies dates from the 1940's. Elucidating examples of the application of this technique in its early stage of development can be encountered, for instance, in Wigner (1945), Levine and Schwinger (1949) and Roussopolos (1953), while applications corresponding to the actual state-of-the-art are provided, for example, by Hall and Cacuci (1983), Zou *et al.*, (1993) and Le Dimet *et al.*, (1995).

As it is apparent from the above references, applications are found in a variety of fields, ranging from reactor theory to atmospheric modeling. The theoretical approaches in the formulation of the sensitivity equations have evolved from perturbation theory (Wigner 1945) and variational theory (Levine and Schwinger 1949, Roussopolos 1953) based approaches to incorporate the differential approach (Oblow 1978, Parks and Maudlin 1981), the nonlinear functional approach (Cacuci 1981a,b) and other approaches.

An extensive study of the mathematical foundations underlying the sensitivity theory for functional and operator-type response functions is found in Cacuci (1981a,b). By using nonlinear functional analysis, Cacuci has shown that the existence of the Gâteaux differentials (to be defined shortly) of the operators appearing in the model formulation equations was the necessary and sufficient condition for the validity of the forward sensitivity theory. The necessary and sufficient condition for the validity of the adjoint sensitivity formalism is more restrictive, namely, operators acting on the state vector must admit densely defined Gâteaux derivatives and the underlying normed spaces must to be complete.

3.2.2 The Adjoint Sensitivity Equations

The starting point is the system of K coupled nonlinear equations that describe the nonlinear evolution of the system. We will write them in vector form as:

$$\frac{d\mathbf{x}}{dt} = F(\mathbf{x}, \boldsymbol{\alpha}, t), \tag{1}$$

where $\mathbf{x} = (x_1, \cdots, x_K)^T$ is the state vector, $\boldsymbol{\alpha} = (\alpha_1, \cdots, \alpha_I)^T$ is the I^{th} dimensional vector of system parameters and $\mathbf{F} = (F_1(\mathbf{x}, \boldsymbol{\alpha}, t), \cdots, F_K(\mathbf{x}, \boldsymbol{\alpha}, t))^T$ represents all physical processes that can change the state vector. We assume that accompanying equations for the initial and boundary conditions are known.

A measure $R(\mathbf{r}, t)$ of the forecast aspect for which we desire to evaluate the sensitivity has to be chosen. Here, $\mathbf{r} = (x, y, z)$ is the position vector in physical space. In concrete applications, R can take the form of a scalar quantity, of a time dependent operator or of a time and space dependent operator. For example, in data assimilation problems R is usually defined as a time integrated, weighted, squared forecast error:

$$R = \sum_n (\mathbf{x}_n - \mathbf{x}_{obs})^T W_n (\mathbf{x}_n - \mathbf{x}_{obs}). \tag{2}$$

In (2), W is a diagonal matrix of weights and the subscript "obs" denotes values for a verifying analysis at time t_n (*e.g.* Le Dimet and Talagrand 1986). $R(\mathbf{r}, t)$ is called the response function or aspect measure.

The central concept in the definition of the sensitivity is the Gâteaux differential, VR, which represents the first order approximation to the variation of R due to changes in the

parameter and state vectors, $\delta\boldsymbol{\alpha}$ and $\delta\mathbf{x}$. For our purposes it suffices to consider only the state vector variations, *i.e.*, that the parameter vector $\boldsymbol{\alpha}$ is kept constant. In that case, we have:

$$VR_t(\mathbf{x}_o, \delta\mathbf{x}) = \left(\frac{\partial R}{\partial \mathbf{x}}\right)_{\mathbf{x}_o} \delta\mathbf{x}. \tag{3}$$

The derivative in (3) is to be evaluated at the nominal value ($\mathbf{x}_o$). Here, $\mathbf{x}_o$ is a time evolving reference trajectory, which is an exact solution of the model equation (1). The subscript "t" in VR_t indicates that the Gâteaux differential is taken at time t. Its evaluation requires, in principle, the knowledge of the departure from the basic state, $\delta\mathbf{x}(t)$.

Writing $\mathbf{x}(t) = \mathbf{x}_o(t) + \delta\mathbf{x}(t)$, we obtain from (1):

$$\frac{d}{dt}(\mathbf{x}_o + \delta\mathbf{x}) - \frac{d\mathbf{x}_o}{dt} = F(\mathbf{x}_o + \delta\mathbf{x}, t) - F(\mathbf{x}_o, t). \tag{4}$$

If $\mathbf{F}$ is a sufficiently smooth function of the components of $\mathbf{x}$, then for sufficiently small departures $\delta\mathbf{x}(t)$ a linearized version of (4) is valid:

$$\frac{d(\delta\mathbf{x})}{dt} = L(\mathbf{x}_o)\delta\mathbf{x}\,, \tag{5}$$

where

$$L = \left(\frac{\partial F}{\partial \mathbf{x}}\right)_{\mathbf{x}_o} \tag{6}$$

is *the linear evolution operator.* In our applications, L is to viewed as a matrix.

Equation (5), known as the "*equation of the tangent linear dynamics*," together with the initial condition, $\delta \mathbf{x}_o(t_o) = \delta \mathbf{x}_o$, allows the calculation of the deviation $\delta \mathbf{x}(t)$, and therefore the evaluation of the Gâteaux differential (3). This is the "forward sensitivity" method.

We see that such an approach is convenient only if we are interested in studying the relative effects of just a few changes in the initial condition. Should we wish to study the relative effects of a large number of changes in the intial condition, then the adjoint sensitivity formalism becomes much more advantageous.

An excellent derivation of the equations of the adjoint sensitivity for functional, time dependent and time-and-space dependent type-responses can be found in Zou *et al.*, (1993). Here, we present a derivation for a functional type response, chosen in the very specific way that pertains to the applications in this investigation.

Let us choose a response function R given at time t by

$$R_t = Const. < P(\mathbf{x} - \overline{\mathbf{x}}), P\mathbf{x}_b >, \tag{7}$$

where *Const.* is a constant, $< \cdots, \cdots >$ denotes an inner product in a Hilbert space, $\mathbf{x}$ is the actual state vector, $\overline{\mathbf{x}}$ is the climatological mean state and $\mathbf{x}_b$ is a pre-defined constant vector. P is a projection operator, and performs the operations of going from spectral space to grid-point space and setting to zero all grid-point values outside some chosen domain Σ. The norm in (7) is chosen according to the specific problem at hand. The response function so defined has the meaning of a regional projection of the anomaly pattern $(\mathbf{x} - \overline{\mathbf{x}})$ onto a fixed pattern $\mathbf{x}_b$.

A perturbation, $\delta \mathbf{x}(t_o) = \delta \mathbf{x}_o$, added to the initial condition $\mathbf{x}_o$, at time t_o, will evolve

to become $\delta\mathbf{x}(t)$, at time t. The change in the response function at time t is given by:

$$\begin{aligned}\delta R_t &= Const.\{< P(\mathbf{x}+\delta\mathbf{x}-\overline{\mathbf{x}}), P\mathbf{x}_b > - < P(\mathbf{x}-\overline{\mathbf{x}}), P\mathbf{x}_b >\} \\ &= Const. < P\delta\mathbf{x}, P\mathbf{x}_b > \\ &= Const. < \delta\mathbf{x}, P^*P\mathbf{x}_b >, \end{aligned} \tag{8}$$

where P^* is the adjoint to P.

Assuming a linear evolution over the time window of concern, $t - t_o$, we can write:

$$\delta\mathbf{x}(t) = A(t_o, t)\delta\mathbf{x}(t_o), \tag{9}$$

where

$$A(t_o, t) = e^{\int_{t_o}^{t} L dt} \tag{10}$$

is termed the propagator between t_o and t. We note that, in particular, if $t = t_o$, then $A = I$, where I is the unit operator. Equation (9), with $A(t_o, t)$ given by (10), follows immediately from formally integrating (5).

Taking (9) into account, we can rewrite (8) as:

$$\delta R_t = Const. < \delta\mathbf{x}(t_o), A^*(t, t_o)P^*P\mathbf{x}_b >, \tag{11}$$

where $A^*(t, t_o)$ is the adjoint to the propagator. Notice that δR_t, being linear in $\delta\mathbf{x}$, is the Gâteaux differential.

We can further rewrite (11) as:

$$\delta R_t = < \delta \mathbf{x}(t_o), \mathbf{q}(t_o) >, \tag{12}$$

where

$$\mathbf{q}(t_o) = A^*(t, t_o)\,(Const.\, P^* P \mathbf{x}_b) \tag{13}$$

is the adjoint vector at time t_o. In practice, $\mathbf{q}(t_o)$ is obtained by integrating the adjoint model backwards from time t to t_o, starting with the initial condition $(Const.\, P^* P \mathbf{x}_b)$ [1]

With this exercise we are now able to compute the Gâteaux differential without explicitly solving for the deviation $\delta \mathbf{x}$. Instead, we integrate the adjoint model, which is equivalent to solving the adjoint equation:

$$-\frac{d\mathbf{q}}{dt} = L^* \mathbf{q}, \tag{14}$$

subject to the condition

$$\mathbf{q} = \left(\frac{\partial R}{\partial \mathbf{x}}\right), \tag{15}$$

at final time t of the time window $t - t_o$. L^* is the adjoint operator to the linear evolution operator L.

Since the adjoint equation and the initial condition are independent of changes in the state vector, it suffices to solve equation (14) just once.

[1] It is an interesting and instructive exercise to show that the dot product (12) is invariant over the time window $t - t_o$. This can be done by using the property that the propagator between t_o and t can be written as the product of the propagator between t_o and t_n and the propagator between t_n and t, where $t_n \leq t$.

A generalization of the method to include variations in the parameter vector can be found in Zou *et al.*, (1993).

CHAPTER 4

Normal Modes and Adjoint Modes. Methods of Calculation

The T31 nonlinear model solution $\mathbf{x}_o$ at initial time t_o is the basic state on which the three-dimensional instability calculations were performed. *To fit the computational resources at our disposal, we computed the normal modes, adjoint modes (and singular vectors) on the T20 version instead of the T31 version of the tangent linear model.* The accuracy of the eigenanalysis with the reduced truncation is discussed in section 8.2.

Although the original model uses complex state vectors, linear instability calculations in the complex space add unnecessary complications to the problem. Hence, it is convenient to map the original complex vector onto a real vector made-up of all the real and imaginary parts of the predictive variables as distinct elements, and perform the calculations with real matrices. In this section, $\delta\mathbf{x}$ is a real state vector of dimension N, which contains the real and imaginary parts of all non-zero spectral coefficients of the relative vorticity, ζ, the divergence, D, and the Exner layer thickness, $\Delta\pi$. For zonal wavenumber $m = 0$, the "complex" spectral coefficient contributes to the state vector $\delta\mathbf{x}$ with just one element, since the imaginary part is always zero.

Under the assumption that $\mathbf{x}_o$ is a resting basic state, equation (5) becomes an autonomous first order differential equation.

Modal solutions to (5) which possess an exponential temporal dependence of the amplitude are obtained through the ansatz $\delta\mathbf{x} = e^{\sigma t}\mathbf{z}$. This leads to the eigenvalue problem:

$$L\mathbf{z} = \sigma\mathbf{z}, \tag{16}$$

where $\mathbf{z}$ is the eigenvector and $\sigma = \sigma_r + i\sigma_i$ is the eigenvalue. The real part of σ, σ_r, is the growth rate, and the imaginary part, σ_i, is the frequency.

To solve for the eigenvalue problem, we need to first construct the matrix L. This is done very easily with the help of the time-stepping tangent linear model. By setting the l^{th} component of $\delta\mathbf{x}$ to 1, zeroing all the other components, and making a one-time-step integration, we obtain the tendency $\frac{d(\delta\mathbf{x})}{dt}$, which is the l^{th} column of L. Repeating this process N times yields L. The procedure thus consists of generating L a column at a time. Finally, a standard eigenanalysis routine is used to compute all the eigenvectors $\{\mathbf{z}_n\}$ and corresponding eigenvalues $\{\sigma_n\}$.

The n^{th} normal mode $\mathbf{Z}_n$ is defined by:

$$\mathbf{Z}_n = Re\{e^{\sigma_n t}\,\mathbf{z}_n\}, \tag{17}$$

i.e.,

$$\mathbf{Z}_n = e^{\sigma_{nr} t}\{\mathbf{z}_{nr}\,cos(\sigma_{ni}t) - \mathbf{z}_{ni}\,sin(\sigma_{ni}t)\}, \tag{18}$$

where $\mathbf{z}_{nr}$ and $\mathbf{z}_{ni}$ are vectors of the real and imaginary parts of $\mathbf{z}_n$, respectively. We shall call $\mathbf{z}_{nr}$ *the real phase* of the n^{th} normal mode and $\mathbf{z}_{ni}$ *the imaginary phase*.

The calculation of the adjoint modes requires the prior definition of a norm for the linear space of the perturbations. Throughout this work we will use the *norm of the integrated total perturbation energy (energy norm, for short).* The justification for this choice is given in Chapter 5. Appendix B contains the derivation of the expression for the integrated total perturbation energy:

$$E = \int\int \{\sum_{k=1}^{2} (\frac{|\mathbf{u}_k'|^2}{2}) + \frac{\Delta\theta}{2\Delta\overline{\pi}_o}\pi_{3/2}'^2 + \frac{\theta_1}{2\Delta\overline{\pi}_o}\pi_{1/2}'^2\} dxdy, \tag{19}$$

where $\Delta\overline{\pi}_o$ is a reference Exner-layer thickness. The primes denote perturbation quantities. The reader is referred to Appendix A for the meaning of the quantities appearing in (19).

The squared norm of the state vector $\delta\mathbf{x}$ with respect to the integrated total perturbation energy will be denoted by:

$$\| \delta\mathbf{x} \|_E^2 = < \delta\mathbf{x}, \delta\mathbf{x} >_E . \tag{20}$$

We can write,

$$< \delta\mathbf{x}, \delta\mathbf{x} >_E = < \delta\mathbf{x}, \mathcal{D}\delta\mathbf{x} >_{L_2}, \tag{21}$$

where $< \cdots, \cdots >_{L_2}$ denotes the dot product in the Euclidian norm, and $\mathcal{D}$ is a real weight matrix derivable from (19), as shown in Appendix C.

By definition, the adjoint matrix L^* with respect to the energy norm satisfies the relation:

$$< \delta \mathbf{y}, L\delta \mathbf{x} >_E = < L^* \delta \mathbf{y}, \delta \mathbf{x} >_E, \tag{22}$$

where $\delta \mathbf{x}$ and $\delta \mathbf{y}$ are two arbitrary vectors of the linear space of the perturbations. Taking (21) into account, (22) can be rewritten as

$$< \delta \mathbf{y}, \mathcal{D} L\delta \mathbf{x} >_{L_2} = < L^* \delta \mathbf{y}, \mathcal{D}\delta \mathbf{x} >_{L_2}, \tag{23}$$

or, in conventional vector notation

$$(\delta \mathbf{y})^T \mathcal{D} L\delta \mathbf{x} = (L^* \delta \mathbf{y})^T \mathcal{D}\delta \mathbf{x}, \tag{24}$$

where the superscript "T" denotes the transpose. It follows from (24) that

$$L^{*^T} = \mathcal{D} L \mathcal{D}^{-1} \ . \tag{25}$$

If, for computational purposes, we redefine the state vector $\delta \mathbf{x}$ so as to include $\pi'_{1/2}$ and $\pi'_{3/2}$ in place of $\Delta\pi'_1$ and $\Delta\pi'_2$, respectively, the weight matrix $\mathcal{D}$ assumes a diagonal form. In that case, we can write:

$$L^* = \mathcal{D}^{-1} L^T \mathcal{D} \ . \tag{26}$$

The adjoint eigenvectors $\{\mathbf{g}_m\}$ are the eigenvectors of L^*, with corresponding eigenvalues $\{\beta_m\}$. As for the normal modes, the m^{th} adjoint mode is defined by:

$$\mathbf{G}_m = e^{\beta_{mr} t} \{ \mathbf{g}_{mr} \cos(\beta_{mi} t) - \mathbf{g}_{mi} \sin(\beta_{mi} t) \}, \tag{27}$$

where $\mathbf{g}_{mr}$ is the *real phase* of the m^{th} adjoint mode and $\mathbf{g}_{mi}$ the *imaginary phase.* According to (22), one can write

$$< \mathbf{g}_m, L\mathbf{z}_n >_E = < L^* \mathbf{g}_m, \mathbf{z}_n >_E \tag{28}$$

or,

$$(\alpha_n - \beta_m^{cc}) < \mathbf{g}_m, \mathbf{z}_n >_E = 0, \tag{29}$$

where the superscript "*cc*" denotes the complex conjugate. We note that the rules of calculation in the linear space of the perturbations are those of a Hilbert space. The last equation represents the *biorthogonality relation.* It states that for any eigenvector $\mathbf{z}_n$ and adjoint eigenvector $\mathbf{g}_m$ which are not orthogonal to each other, the corresponding eigenvalues must be complex conjugates to one another.

Notice that there is an arbitrariness in the definition of the phase and amplitude of any eigenvector $\mathbf{z}_n$ or adjoint eigenvector $\mathbf{g}_m$. We remove this arbitrariness by choosing the amplitudes and phases in the manner of Zhang (1988), *i.e.*, by imposing:

$$< \mathbf{z}_{nr}, \mathbf{z}_{ni} >_E = 0; \quad \| \mathbf{z}_{nr} \|_E = 1 \tag{30}$$

$$< \mathbf{z}_{ni}, \mathbf{g}_{nr} >_E = 0; \quad \| \mathbf{g}_{nr} \|_E = 1 \, . \tag{31}$$

It can be shown through simple algebra, and with help of (29), that this choice is consistent with the equality:

$$< \mathbf{z}_n, \mathbf{g}_n >_E = 2(1 - \frac{\delta_n}{2}) < \mathbf{z}_{nr}, \mathbf{g}_{nr} >_E = 2(1 - \frac{\delta_n}{2})\gamma_n^{-1} \ , \tag{32}$$

where $\delta_n = 1$ for eigenvectors with real eigenvalues and $\delta = 0$ otherwise, and

$$\gamma_n = < \mathbf{z}_{nr}, \mathbf{g}_{nr} >_E^{-1} \tag{33}$$

is a real quantity, termed the *projectability* by Zhang (1988). The latter is a measure of the inverse of the cosine of the angle subtended by the eigenvector and corresponding adjoint eigenvector in the linear space of the perturbations. For an orthogonal system $\gamma_n = 1$ for every n; it can reach values ~ 100 for non-orthogonal systems. As discussed by Zhang (1988), γ_n *is a measure of the potential for initial growth of norm that the* n^{th} *normal mode can experience.* Large values of γ_n imply a high potential for initial growth *i.e.*, for growth due to the initial projection of perturbations. Zhang (1988) found amplifications in the perturbation energy by a factor of about 50 in 10 days due to this mechanism of growth. He suggested that the projectability of the normal modes, together with the system of adjoint modes, should augment the list of tools associated with growth rate and frequency of the normal modes. We want to emphasize that the initial growth results from a mechanism distinct from that of the conventional barotropic and baroclinic instability. The importance of the orthogonality relations of the normal modes was clearly recognized by Farrell (1988), although no specific reference to the concept of projectability was made.

CHAPTER 5

Singular Vectors

5.1 Introduction

The works of Charney (1947) and Eady (1949) played a major part in the development of the field of dynamic meteorology over the last four or five decades. Various aspects of the atmospheric circulation, in particular cyclogenesis, were modeled with appreciable success through the Charney-Eady approach of baroclinic instability of the large scale flows. Exponentially growing modes of the linearized dynamics are the central piece in this theory. The horizontal scale, vertical structure and growth rate associated with some of these shape-preserving solutions are in good agreement with observations of typical mid-latitude cyclones.

The theoretical understanding of (structure) development has proceeded from the assumption that small perturbations to the large scale flow amplify as a result of flow dependent instabilities, and that the exponential mode of largest growth rate ultimately dominates the evolution, masking the details of the structure of the initial perturbation, and naturally setting the scale of the observed disturbance. For a long time, the focus has been on the exponential mode of maximum growth rate, or at best, on the few most rapidly growing modes, as interference effects have long been known to be important.

Studies aimed at ascertaining the role of nonlinearities in cyclogenesis have in general supported the concept that they are important in the mature and decay stages of the cyclone life-cycle (Simmons and Hoskins 1978), producing equilibration and decay of the wave, but that cyclone initiation and intensification can be described by linear theory. The same is believed to be applicable to other scales of motion, as the linear approach can be regarded as a first order approximation in a perturbation expansion of the pertaining evolution equations.

While the linearized dynamics is indisputably a useful approach, modal analysis, as vigorously pointed out in recent years, falls short in some aspects. For instance:

1. Basic state flows derived from analysis of the real atmosphere are not solutions of any kind to the model nonlinear evolution equations. However we know that, strictly speaking, modal instability theory is only valid on resting basic states. In many studies, realistic basic state flows are artificially forced into being stationary solutions by introducing a fictitious forcing. Theoretically, this can be done in many different ways; perhaps the easiest one is to assume a forcing which renders the basic state stationary without interacting with the perturbation. However, as shown by Andrews (1984), the instability characteristics are crucially dependent upon the forcing. This raises doubts regarding the validity of the results from normal mode computations in the context of the real world.

2. Linear theory predicts that an autonomous system which supports exponentially growing modes will be ultimately dominated by the exponential mode of maximum growth rate. This asymptotic behavior is independent of the form of the initial perturbation. It seems, however, that the required time, when estimated from the e-folding time of the

discrete normal modes, is in most cases too large compared with physically relevant time scales of interest (say, one to ten days). This strongly suggests that more attention must be given to the transient evolution.

3. The theory of baroclinic instability of Charney and Eady fails to account for neutral retrograde Rossby waves which are observed in the atmosphere (*e.g.* Deland 1964, Madden 1979, Ahlquist 1985). Theoretical considerations as to the mechanisms of excitation of such large amplitude planetary scale waves include periodic or stochastic forcing (Hirota 1971, Madden 1975, Garcia and Geisler 1981) and the inverse cascade of energy in the framework of the two-dimensional turbulence theory (Charney 1971).

4. In the context of meteorology, until the beginning of the 1980's little attention was paid to the details of the initial value problem that leads to the eventual settling of an exponential mode, even though some fundamental work with idealized flows had long indicated that analysis based solely on exponential modes could not account for the full linear instability behavior of the flow (Orr 1907, Case 1960). The idea is that, while the concept of a "Fourier-type" of synthesis of an arbitrary perturbation through a complete set of discrete orthogonal normal modes can be mathematically substantiated and applied to initial value problems, in practice we are faced with the fact that, except for very special cases, basic state flows do not support a complete set of such modes. The system of normal modes has to be augmented with the continuous spectrum in order to render it complete, and, in general, no orthogonality properties exist. The existence of the continuous spectrum has been known for a long time, but over the years, it was in general ignored, on the assumption that it decays algebraically with time. In the Couette problem this decay is of

the form t^{-2}, as originally shown by Orr (1907).

It wasn't until the work of Farrell (1982) that the relevance of the transient evolution in shear flows and the important role played by the continuous spectrum were shown. The complete analysis of the linear instability problem reveals the existence of an additional mechanism of growth, which is distinct from that of the traditional barotropic and baroclinic growth. The latter is associated with the existence of exponentially growing modes. These are structures that, once excited, draw energy from the mean flow for an unlimited period of time, and do not need the presence of "auxiliary" structures in order to grow. Farrell (1982), in revisiting the Couette problem, stressed that although the Couette flow does not support any normal modes, properly configured disturbances can interact with the continuous spectrum and the mean flow, drawing energy from the latter and producing a transient burst in amplitude and energy over physically relevant time scales (see also Boyd 1983). Although such growth cannot be sustained in the context of linear theory, it is tempting to think that it can be saturated in the atmosphere by nonlinear processes, thus preventing the otherwise inevitable linear decay (*e.g.*, Illary and Marshall 1983, Holopainen and Fortelius 1987). Simmons and Hoskins (1979) found in experiments of upstream and downstream development that nonlinear integrations could produce a cutoff of the linear growth long before normal mode form settled. Pedlosky (1964) and Burger (1966) studied the initial value problem for the more realistic Eady and Charney models, respectively. They showed the existence of a continuous spectrum that complements that of the discrete modes. Due to the mathematical complexity of the solutions, formally written as the inverse Laplace transform of Green's functions, they were forced to restrict the analysis to the long

time asymptotic limit. This showed, nonetheless, a very interesting behavior of the Eady neutral waves and the isolated neutral points of the Charney problem. An $O(1)$ asymptotic contribution was found, resulting from the interaction of these neutral waves with the continuous spectrum and the mean flow. Farrell (1982) found a similar asymptotic behavior in numerical integrations of initial value problems on the Eady and Charney models. He also found the vertical wavenumber of the perturbation to be crucial to the early stages of growth. As an example, with an initial perturbation of vertical wavenumber 4 superposed to the Eady basic state, the neutral wave at $k = 2.4$ was found to grow as rapidly as the most unstable wave at $k_m = 1.6062$, over much of the geostrophically relevant time interval. These results show that *flows which do not support exponentially growing modes, but support neutral modes, can behave like unstable flows.* In the parameter range that allow for exponentially growing modes, the degree of their excitation was also found to crucially depend on the initial conditions. This suggests that if structure development in cyclogenesis, blocking and other phenomena has its precursor on finite amplitude disturbances, rather than on infinitesimal perturbations, then the structure of the initial perturbation is crucial to the subsequent evolution. Indeed, *for appropriately chosen initial conditions of finite amplitude, the growth can be so "explosive" that nonlinear equilibration will be reached without the normal mode form having ever settled.* Farrell (1982) suggests that "the total amplification of a disturbance to a geophysical flow may be only a few e-foldings, say in going from a 2 mb depression to a 20 mb surface cyclone." An interesting application of these ideas to Alpine cyclogenesis (Buzzi and Tibaldi 1978) and to rapid cyclogenesis (Sanders and Gyakum 1980) is outlined by Farrell (1982).

Farrell (1988) obtained a similar overall picture in a truncated barotropic model and hypothesized, in particular, that the alternate method described above of exciting normal modes could be the mechanism at work in the excitation of the planetary scale retrograde neutral Rossby waves.

In truncated models of the atmosphere the continuous spectrum is approximated by a set of discrete exponential modes, so that the picture of the mechanism described above has to be revisited. Here, one must bear in mind that shears in the flow generally cause the operator of the linear evolution to loose its self-adjointness (say, with respect to the energy norm). As a result, small perturbations can have large projections onto some of the exponential modes, and also , the modes are now allowed to exchange energy among themselves. The growth of exponential modes due to the initial projection of perturbations was discussed in Chapter 4. A different mechanism of growth that must be considered is that associated with the exchange of energy among the normal modes. As a result of the exchange of energy, certain linear combinations of normal modes can growth faster than any individual normal mode. The latter statement is expressed mathematically by "*the breakdown of the Parseval relation*" (Jeffrey and Jeffrey 1956), *i.e.*, we are no longer able to partition the domain integrated energy among the exponential modes and obtain the total as the sum over the individual mode energies. In fact, the total energy is not a conservative quantity in such cases. Stated inversely, the conservation of a domain averaged quadratic quantity yields a norm under which the modes are orthogonal (Held 1985).

In view of the above points 2, 3, and 4, it seems meaningful to seek initial perturbations which exhibit maximum growth in a well defined sense.

Farrell (1982, 1989) looked at the best possible choice of perturbations of unit amplitude that most efficiently excite a given normal mode in the limit of time approaching infinity. The now well-known answer is the adjoint mode to the targeted normal mode.

Another very appealing problem tackled by Farrell (1988, 1989) is that of seeking the initial condition that exhibits maximum growth of a chosen norm after a prescribed optimization time τ. Such initial perturbations are called *optimal perturbations* or *singular vectors*. Their importance was suggested for the first time by Lorenz (1965) in the context of atmospheric predictability. Calculations for the actual atmosphere were performed, among others, by Borges and Hartmann (1992), using a barotropic model, Molteni and Palmer (1993), using a T21 barotropic and a T21 three-level quasi-geostrophic model and by Buizza *et al.*, (1993), using a 19-level primitive equation model.

The approach of optimal vectors shifts the scenario from the normal mode analysis to the non-modal analysis. The underlying assumption is that a spectrum of small but finite amplitude disturbances exists in the flow, and that some subset of this spectrum will have the right phase relative to the shear of the large scale flow to rapidly transform the large source of barotropic and baroclinic energy of the basic state into perturbation energy. Buizza and Palmer (1995) interpreted the energy growth of optimal vectors on the ECMWF primitive-equation model in terms of wave activity being propagated into the jet.

5.2 Mathematical Aspects of Singular Vectors

The starting point is the linear evolution equation in integral form, (9). No restriction to resting basic state trajectories is needed in this derivation.

The energy norm is used throughout; its justification is given at the end of section 5.3. Notice, however, that the derivation to follow could have been presented without any prior assumption of a specific norm.

The total integrated perturbation energy at a time τ can be written as

$$E(\tau) = < \delta \mathbf{x}(\tau), \delta \mathbf{x}(\tau) >_E, \tag{34}$$

or, taking (9) into account,

$$E(\tau) = < \delta \mathbf{x}(t_o), A^*(\tau, t_o) A(t_o, \tau) \delta \mathbf{x}(t_o) >_E, \tag{35}$$

where $A^*(\tau, t_o)$ is the adjoint of the propagator with respect to the energy norm.

Our task consists of determining the initial perturbation which maximizes the total energy (35) at finite time τ, with the constraint that it possesses a unit energy at the initial time.

We note that the operator (A^*A) is self-adjoint by construction. Hence, its eigenvectors, $\{\boldsymbol{\nu}_i\}$, form a complete set of orthogonal vectors in the energy sense, and its eigenvalues, λ_i^2, are real and positive. The positiveness of the eigenvalues follows from the fact that the norm is introduced through a positive definite matrix.

Expressing an arbitrary perturbation $\delta \mathbf{x}(t_o)$ as a linear combination of the eigenvectors of (A^*A), and using their orthogonality properties, one can easily show that the maximum of (35) is obtained if $\delta \mathbf{x}(t_o)$ is chosen as the eigenvector with largest eigenvalue. By induction, the second largest eigenvalue will be associated with the initial pattern that produces

the second largest growth over the time interval τ, and so on. In other words, *we seek the singular vectors (SV's) of* $A(t_o, \tau)$, *which are defined through*

$$A^*(\tau, t_o)A(t_o, \tau)\boldsymbol{\nu}_i = \lambda_i^2 \boldsymbol{\nu}_i. \tag{36}$$

The square roots $\{\lambda_i\}$ *of the eigenvalues are by definition the singular values of A (e.g. Noble and Daniel 1977).*

The total energy of a singular vector $\boldsymbol{\nu}_i$ at time τ is given by

$$< \boldsymbol{\nu}_i(\tau), \boldsymbol{\nu}_i(\tau) >_E = \lambda_i^2 \ < \nu_i(t_o), \nu_i(t_o) >_E \tag{37}$$

i.e., the singular values $\{\lambda_i\}$ give the amplification factors of the norm over time interval τ.

The singular vectors form an orthogonal basis which evolves in orthogonal patterns (Nobel and Daniel 1977).

In this work we will be interested in regional SV's, *i.e.*, in SV's constrained to grow over a local area, Σ. To obtain those, we introduce a projection operator T as:

$$T = S^{-1}GS, \tag{38}$$

where S is the transform matrix from spectral to grid-point space, S^{-1} is its inverse and G is a matrix which sets to zero all grid-point values that lie outside Σ. Notice that T does not coincide with the projection operator P introduced in Chapter 3, since the latter does not involve the final transformation back into spectral space.

It is clear that the perturbation energy inside Σ, E_Σ, is given at time τ by:

$$E_\Sigma(\tau) = < TA\delta\mathbf{x}(t_o), TA\delta\mathbf{x}(t_o) >_E, \tag{39}$$

or

$$E_\Sigma(\tau) = < \delta\mathbf{x}(t_o), (TA)^*(TA)\delta\mathbf{x}(t_o) >_E . \tag{40}$$

In other words, *the regional SV's are the eigenvectors of* $(TA)^*(TA)$. They also form a complete set of orthogonal patterns in the sense of the *hemispherically* integrated total energy, and the orthogonality is preserved during their evolution.

In practice, for time evolving reference trajectories, or for large and sparse problems, a few dozen of the "most explosive" SV's can be found by using iterative methods. The iterative Lanczos method is often referred to in this regard (*e.g.* Lacarra and Talagrand 1988 and Buizza *et al.*, 1993). It is an algorithm which does not require the knowledge of the matrix elements of the operator $(TA)^*(TA)$, and can be used in conjunction with the direct and adjoint linear models.

For a resting basic state, the propagator can be calculated exactly, so that the operator $(TA)^*(TA)$ can be obtained. Once the propagator has been calculated, the product (TA) can be readily obtained by using the model built-in routines for the Fourier-Legendre direct and inverse transforms. If the system is not too large, standard eigenanalysis routines can then be used to obtain all the singular values and singular vectors. In this study, calculations where performed solely on resting basic states. Appendix D describes how the

propagator $A(t_o, \tau)$ was calculated. A standard EISPACK routine was used to calculate all the eigenvalues and eigenvectors of (A^*A).

We note that the answer represented by (36) to the question of finite-time optimization growth was found without any reference to modal solutions, exponential growth or time invariant basic states. This is particularly fortunate in view of point 1, in section 5.1.

SV's are also used by the ECMWF to construct a set of initial conditions in ensemble forecasting (Molteni *et al.*, 1995). Since they define, in the linear context, the directions in phase space of largest instability, they are the natural candidates to provide an estimation of the predictability of the atmosphere in the early stages of the forecast.

As discussed by Buizza and Palmer (1995), the singular vectors can be regarded as a natural extension of the Charney-Eady theory of baroclinic instability. It is intuitively clear that, for resting basic states, as the optimization time is made larger and larger, the structure of the dominant singular vector will approach that of the most unstable normal mode at optimization time and that of the corresponding adjoint mode at initial time. Perhaps less apparent is that, for time varying reference trajectories, as the optimization time is increased, the singular vectors approach the Lyaponov vectors. In a sense, the latter are the perturbations produced by the so-called breeding method (Toth and Kalnay 1993), which are used in ensemble forecasts at NMC.

5.3 Choosing a Norm

In Chapter 6 we calculate perturbations that produce the largest change in the direction of phase space that corresponds to a blocking pattern after a prescribed time interval.

Resulting perturbations are of sub-synoptic scale. They subsequently evolve to larger scales, a behavior typical of the upscale transfer of energy in the atmosphere. For this reason, the energy norm is used throughout this work for both the SV's and for the adjoint modes.

CHAPTER 6

Sensitivity to Normal Modes, Adjoint Modes and Singular Vectors. Methodology

As mentioned in section 1.4, we gain insights into the dynamics of blocking by studying the sensitivity of a response function to sets of structures which we tentatively postulate to be of physical significance in the evolution of atmospheric flows. Such sets are the normal modes, adjoint modes and singular vectors.

We proceed by expanding the T31 model state vector, $\mathbf{x}_o$, at time $t = t_o$, in terms of the complete set of the T20-structures of concern. That is, we write the initial conditions as a linear combination of the normal modes, adjoint modes or singular vectors obtained from the T20 version of the tangent linear model. We recall from Chapter 4 that the instability analysis is performed with the reduced truncation, T20. For convenience, we regard $\mathbf{x}_o$ as a real state vector, written in the manner described in Chapter 4.

In particular, if $\{\mathbf{z}_j\}$ is the complete set of the T20 (complex) eigenvectors that define the normal modes (see eqs. (16), (17) and (18)), we write:

$$\mathbf{x}_o = \sum_j (c_j \mathbf{z}_j + d_j \mathbf{z}_j^*) + \Delta \mathbf{x}_o, \tag{41}$$

where c_j and d_j are complex expansion coefficients, and $\Delta \mathbf{x}_o$ is the residual, which stems

from the fact that the eigenvectors are calculated with a lower truncation in wavenumber space than that of the basic state $\mathbf{x}_o$.

Also from Chapter 4 we recall that the eigenanalysis is performed on real matrices. For real matrices, if $\mathbf{z}_j$ is an eigenvector with the complex eigenvalue α_j, then its complex conjugate $\mathbf{z}_j^*$ is also an eigenvector with the eigenvalue α_j^*. Both, $\mathbf{z}_j$ and $\mathbf{z}_j^*$, are needed in order to render the base set complete.

Using the biorthogonality relation (29), with the adjoint eigenvectors $\{\mathbf{g}_i\}$ computed in the sense of the energy norm, we find that

$$c_j = < \mathbf{g}_j, \mathbf{x}_o >_E \; / \; < \mathbf{g}_j, \mathbf{z}_j >_E \; . \tag{42}$$

Taking (32) into account, (42) yields

$$c_{jr} = < \mathbf{g}_{jr}, \mathbf{x}_o >_E \; / \; \{2(1 - \frac{\delta_j}{2})\gamma_j^{-1}\} \tag{43}$$

and

$$c_{ji} = < \mathbf{g}_{ji}, \mathbf{x}_o >_E \; / \; \{2(1 - \frac{\delta_j}{2})\gamma_j^{-1}\} \tag{44}$$

for the real and imaginary parts of the expansion coefficient c_j, respectively. Recall that γ_j is the projectability of the j^{th} normal mode and that δ_j is one for eigenvectors with real eigenvalues and zero otherwise.

Since $\mathbf{x}_o$ is real, it follows that $d_j = c_j^*$, and, therefore, (41) yields

$$\mathbf{x}_o = \sum_j 2\,(1 - \frac{\delta_j}{2})\,(c_{jr}\mathbf{z}_{jr} - c_{ji}\mathbf{z}_{ji}) + \Delta\mathbf{x}_o. \tag{45}$$

We can rewrite (45) as

$$\mathbf{x}_o = \sum_j (\tilde{c_{jr}}\mathbf{z}_{jr} + \tilde{c_{ji}}\mathbf{z}_{ji}) + \Delta\mathbf{x}_o, \tag{46}$$

where, according to (43) and (44),

$$\tilde{c_{jr}} = 2\,(1 - \frac{\delta_j}{2})c_{jr} = < \mathbf{g}_{jr}, \mathbf{x}_o >_E \ \gamma_j \tag{47}$$

and

$$\tilde{c_{ji}} = -2\,(1 - \frac{\delta_j}{2})c_{ji} = - \ < \mathbf{g}_{ji}, \mathbf{x}_o >_E \ \gamma_j. \tag{48}$$

Relation (46) can be interpreted as the real representation of $\mathbf{x}_o$ in terms of the normal modes, very much in the manner of a Fourier expansion. Note that the real and imaginary phases of a given normal mode enter the expansion as two independent elements of the base set. *The effect of the projectability is that of "amplifying" the expansion coefficients*, as seen in (47) and (48).

It is obvious that (46), (47) and (48) can also be used with the eigenvectors $\{\mathbf{z}_j\}$ and adjoint eigenvectors $\{\mathbf{g}_j\}$ interchanged, in which case we obtain the representation of $\mathbf{x}_o$ in terms of the adjoint modes.

The representation of $\mathbf{x}_o$ in terms of the singular vectors $\{\boldsymbol{\nu}_l\}$ is straightforward. Since $\{\boldsymbol{\nu}_l\}$ forms a complete orthogonal base set, we can immediately write

$$\mathbf{x}_o = \sum_l \tilde{c}_l \boldsymbol{\nu}_l + \Delta\mathbf{x}_o, \tag{49}$$

where $\tilde{c}_l = < \boldsymbol{\nu}_l, \mathbf{x}_o >_E$. It is assumed that the singular vectors have been normalized to have a unit norm.

Relation (46) or (49) can be written in matrix form as

$$\mathbf{x}_o = E\,\tilde{\mathbf{c}}, \tag{50}$$

where E is the real matrix

$$E = (\phi_1, \phi_2, \cdots, \phi_N, \Delta\mathbf{x}_o). \tag{51}$$

The real (column) vectors $\phi_1, \phi_2, \cdots, \phi_N$ are the vectors of the real and imaginary phases of the eigenvectors, or of the adjoint eigenvectors, or the N singular vectors. N is the dimension of the matrix of the linear evolution operator cast in real representation.

In (50), $\tilde{\mathbf{c}}$ is a real $(N+1)$ column matrix. It is made-up of the N real expansion coefficients and the additional element $\tilde{c}_{N+1} = 1$, *i.e.*,

$$\tilde{\mathbf{c}} = (\tilde{c}_1, \tilde{c}_2, \cdots, \tilde{c}_N, \tilde{c}_{N+1})^T. \tag{52}$$

Any change in the initial condition, $\mathbf{x}_o$, is equivalent to a change in the vector of expansion coefficients, $\tilde{\mathbf{c}}$. A change in the initial condition results in a change δR_t in the response function at a time t. Within linear theory, the change in the response function can be evaluated with help of the adjoint sensitivity analysis. As shown in section 3.2.2, δR_t is given by equation (12). For the purpose of studying the relative importance of individual normal modes, adjoint modes and singular vectors it is convenient to use the vector of expansion

coefficients as the control variable. The convenience of such a choice of the control variable will become transparent shortly. Writing $\delta \mathbf{x}(t_o) = E\,\delta\tilde{\mathbf{c}}$, we can rewrite equation (12) in a way such that $\tilde{\mathbf{c}}$ becomes the control variable:

$$\begin{aligned} VR(\mathbf{x}_o, \delta\tilde{\mathbf{c}}) &\equiv \delta R_t \\ &= < E\,\delta\tilde{\mathbf{c}}, \mathbf{q} > \\ &= < \delta\tilde{\mathbf{c}}, E^T\mathbf{q} > \quad . \end{aligned} \tag{53}$$

E^T is the transpose of E.

We define the relative sensitivity to the i^{th} expansion coefficient, $\tilde{c}_i$, as

$$RS = \frac{\delta R_t(\mathbf{x}_o, \delta\tilde{\mathbf{c}})}{\delta\tilde{c}_i}\,|_{\delta\tilde{\mathbf{c}}=(0,\cdots 0,\delta\tilde{c}_i\neq 0,0,\cdots,0)^T}. \tag{54}$$

Computing the relative sensitivity (54) is equivalent to perturbing the initial state with *one* phase of a given normal mode or adjoint mode, or perturbing it with *one* singular vector, performing the model integration, and evaluating the change in the response function at the final time. The relative sensitivity is simply the change in the response function *per* unit change in the expansion coefficient. Various authors, *e.g.* Mureau *et al.*, (1993), have studied the importance of normal modes and singular vectors in triggering a blocked state by actually integrating the model with various perturbed initial states. Clearly, such a procedure is impractical if we want to ascertain the importance of all and each one of these structures. The adjoint sensitivity technique is very powerful in this regard, for it allows us to compute the relative importance of these structures in a computationally affordable time,

without actually integrating the model. Limitations come from the use of linear theory, *i.e.*, the results of the adjoint sensitivity technique are strictly valid only for perturbations that evolve linearly during the time interval of concern.

Once the "most dangerous" structures are identified, one can proceed to superpose these structures onto the control run at initial time, integrate the nonlinear model and study the physical reasons as to why they produce the largest changes in the response function.

CHAPTER 7

Blocking Predictability

An objective measure of a blocked state is necessary. We define the blocking index, R, as the normalized L_2 inner product on the sphere of the daily upper-layer streamfunction anomaly $\psi_u - \overline{\psi_u}$ with the streamfunction of a "mean blocking pattern," ψ_b. Note that ψ_u represents the actual upper layer streamfunction and $\overline{\psi_u}$ is the upper layer climatological mean streamfunction, both given in grid-point space. The latter was obtained by averaging over a 2000-day run with sampling twice daily, from t=101 days to t=2100 days. The first 100 days of the integration were disregarded.

Fig. 3 shows the upper and lower-layer climatological streamfunctions for $\pi_\beta = 0.9$ and $\pi_\beta = 0.7$. We recall from Chapter 2 that the parameter π_β measures the north-south slope of the drive state interface. It is therefore a measure of the strength of the drive state's upper-layer jet. In this investigation, detailed analysis will be presented only on blocks obtained with $\pi_\beta = 0.9$. A reference to blocks excited with $\pi_\beta = 0.7$ will however be made. We found that the blocking patterns appear to be excited by different mechanisms if we use these two values of the parameter π_β. Both upper-layer maps show an approximate wavenumber 4 structure of the mid-latitude jet, especially in the case of $\pi_\beta = 0.9$. Observational mean climatological streamfunctions at upper layers (say at 500 mb) have a predominant wave number 3 structure. The idealized topography used in this work seems to be the main

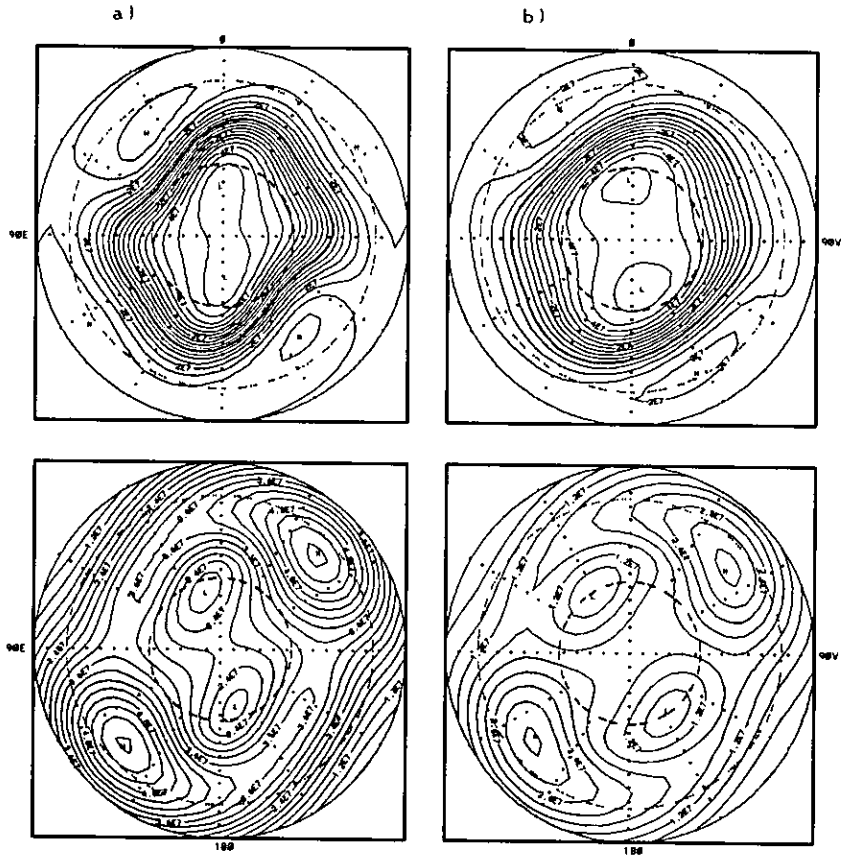

Figure 3: Upper (top-panels) and lower-layer (bottom panels) mean climatological stream-function for $\pi_\beta = 0.9$ (column a) and $\pi_\beta = 0.7$ (column b). Contour interval $5 \times 10^6 m^2 s^{-1}$ for upper-layer and $3 \times 10^6 m^2 s^{-1}$ for lower-layer. The boundary circle is 20°N and interior circles are 30°N and 60°N.

reason why the model yields a wave number 4 climatology.

A hat function defined in grid-point space allows us to restrict the inner product to a chosen geographical region, Σ. This is meaningful, since we will be individually studying blocking episodes that occur in a specific geographical region. The hat function is defined to have a value 1 inside Σ and 0 outside.

The blocking index can be mathematically expressed as:

$$R = Const. < \mathcal{P}(\mathbf{x} - \overline{\mathbf{x}}), \mathcal{P}\mathbf{x}_b >_{L_2}, \tag{55}$$

where $Const =< \psi_b, \psi_b >^{-1}$, $\mathbf{x}_b$ is the vector of the "mean blocking pattern," $\mathbf{x}$ is the actual state vector and $\overline{\mathbf{x}}$ is the climatological state vector. All vectors are given in spectral space. We recall from Chapter 2 that they are made-up of the spectral coefficients of the vorticity, ζ, divergence, D, and Exner-layer thickness, $\Delta\pi$, in each layer. $\mathcal{P}$ is a projection operator which performs the operation of going from spectral $\{\zeta, D, \Delta\pi\}$ to grid-point $\{\psi, D, \Delta\pi\}$, and then setting to zero all grid-point values except those of the upper-layer streamfunction in the specified geographical region, Σ. Thus, $\mathcal{P}$ contains implicitly the hat function explained above. Note that definition (55) differs slightly from (7), in section 3.2.2, in that $\mathcal{P}$ is more restrictive then the operator P. We avoided going into excessive details in the characterization of the response function in section 3.2.2, in order not to divert the reader from the main purpose of the section, namely, the presentation of the method of the adjoint sensitivity analysis.

The dot product $< x, y >_{L_2}$ is to be interpreted as

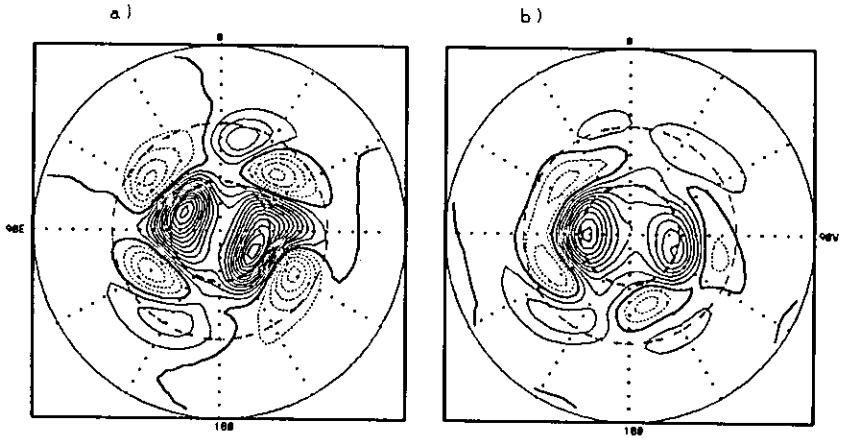

Figure 4: Streamfunction of the "mean blocking pattern" for $\pi_\beta = 0.9$ (panel a) and $\pi_\beta = 0.7$ (panel b). Contour interval $1.6 \times 10^6 m^2 s^{-1}$. Dashed contours for negative values. The boundary circle is the equator and interior circles are 30°N and 60°N.

$$< x, y >= \frac{1}{4\pi} \int \int x\, y\, dS, \tag{56}$$

where dS is the element of surface on the sphere.

The "mean blocking" pattern was obtained as the time average of those 1000 upper-layer streamfunction anomalies which possessed the largest positive anomalies at 60°N. A similar blocking index was introduced for the first time by Liu (1994) and Liu and Opsteegh (1994), and used in sensitivity studies of blocking by Oortwijn and Barkmeijer (1994), henceforth referred to as OB.

Fig. 4 shows the mean blocking pattern for $\pi_\beta = 0.9$ and $\pi_\beta = 0.7$. These patterns suggest that blocking in this model occurs preferentially near $90°E$ and near $90°W$, *i.e.*, upstream of the mountain ridges. The pattern for $\pi_\beta = 0.9$ in both regions and, to some extent, that for $\pi_\beta = 0.7$ in the vicinity of $90°W$, remind us of an omega-type of block, with

a strong positive anomaly north of 50^oN, flanked by two weaker negative anomalies to the south. The pattern for $\pi_\beta = 0.7$ in the vicinity of 90^oE is more reminiscent of a jet-split type of block, possibly a Rex type (Rex 1950a,b), with just one negative anomaly to the south of the blocking high.

A portion of the time series of the blocking index R for $\pi_\beta = 0.9$, with Σ defined to be the semi-hemisphere 0^o-90^oW-180^o, is shown in Fig. 5. We adopted the empirical rule of considering the flow to be blocked if $R \geq 0.75$ and zonal otherwise. In particular, for $R \leq -0.75$ the flow is said to be strongly zonal. With this criteria, a visual inspection of individual streamfunction maps gives a firm impression that the phenomena identified by this objective index would also be identified by synopticians as blocked flows. Certainly, persistence is an additional necessary criteria used to classify an episode as a block. In this research, we classify as blocks those episodes of blocked states which last for at least 5 days.

Fig. 5 shows the occurrence of several blocks, for example, between days 1507 and 1513, and between days 1812 and 1824. The streamfunction pattern at the time of the onset of one of the blocks, day 1507, is shown in Fig. 6.

Following OB, we next compute a time series corresponding to the optimal linear excitation of a blocking pattern in a prescribed time interval τ. For a given time, t_o, we seek the best initial perturbation which, when superposed onto the control run, will produce at time $t_o + \tau$ the largest change in phase space in the direction corresponding to the "mean blocking pattern." We further assume that the perturbations evolve linearly between time t_o and $t_o + \tau$.

From section 3.2.2 (see equation (13)), one sees that the adjoint vector $\mathbf{q}$ represents the

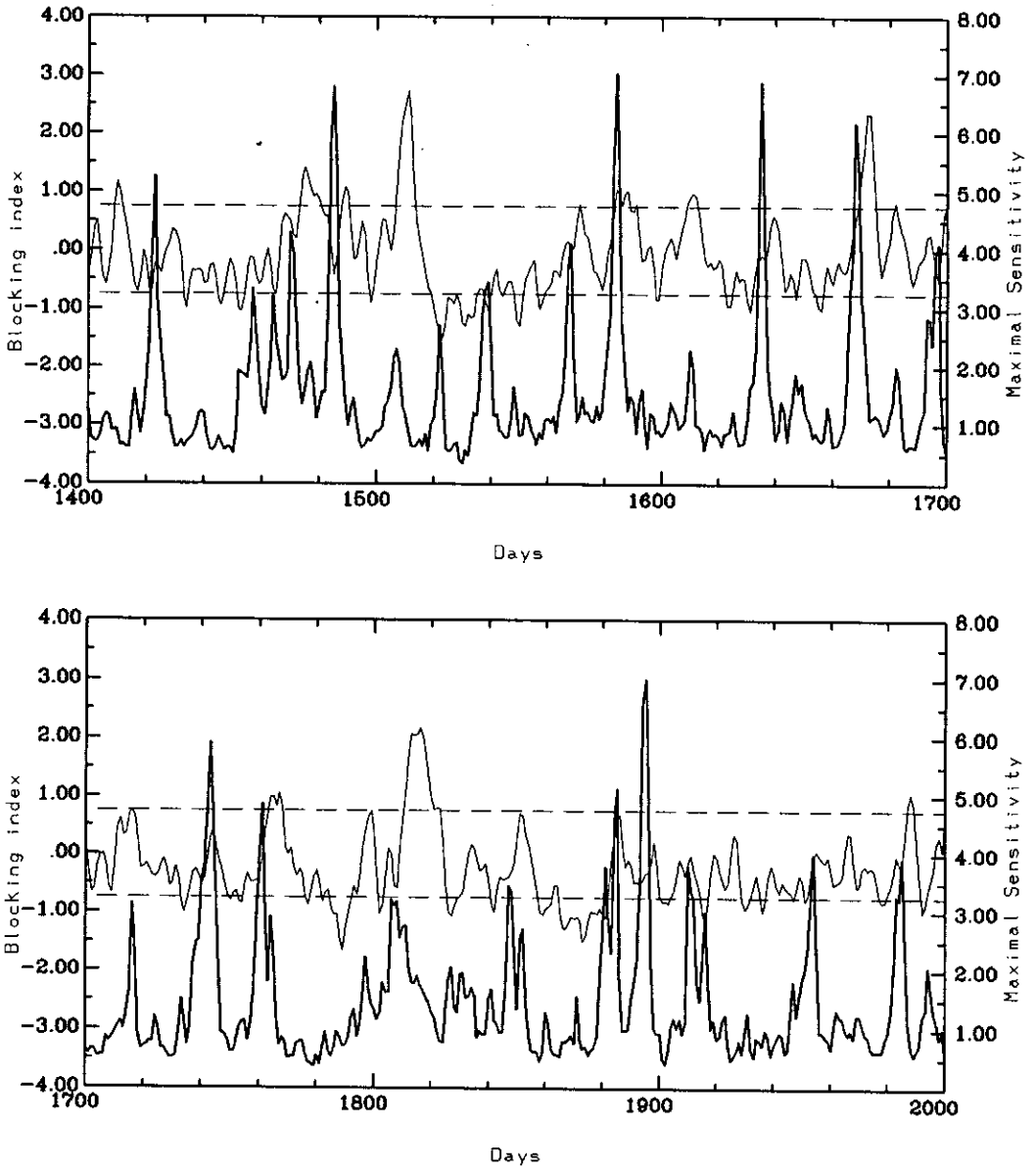

Figure 5: Time series of the blocking index (light line) and maximal sensitivity (dark line) between days 1400 and 2000. The geographical region considered is the semi-hemisphere 0°-90°W-180°. The value of π_β is 0.9. Values of the maximal sensitivity, as defined by eq. (59), are in units of $100 \times m^{-2}s$.

gradient of the response function (at the initial time, t_o). *Per* definition of the gradient, the maximum change in the response function occurs, in the L_2 norm, when the initial perturbation is aligned with the gradient, *i.e.*,

$$\delta \mathbf{x}_{opt}(t_o) = C\, \mathbf{q}(t_o), \tag{57}$$

where the subscript "*opt*" stands for "optimal" and C is a positive constant, determined by specifying the initial norm (amplitude) of the perturbation. We shall call $\delta \mathbf{x}_{opt}(t_o)$ the *optimal-block-triggering-perturbation.* Note that, to be exact, the operator P in (13) must be replaced with $\mathcal{P}$.

With the specific initial perturbation $\delta \mathbf{x}_{opt}(t_o)$, it follows from (12) and the Cauchy-Schwarz inequality that

$$\delta R_{t_o+\tau} = \| \mathbf{q}(t_o) \|_{L_2} \| \delta \mathbf{x}_{opt}(t_o) \|_{L_2} . \tag{58}$$

We define the maximal sensitivity $S_{max}(t_o)$ as:

$$S_{max}(t_o) = \frac{\delta R_{t_o+\tau}}{\| \delta \mathbf{x}_{opt}(t_o) \|_{L_2}} = \| \mathbf{q}(t_o) \|_{L_2}. \tag{59}$$

This quantity is termed "linear sensitivity" by OB. Fig. 5 also shows a portion of the time series of the maximal sensitivity for $\tau = 3$ days. A time interval of 3 to 4 days corresponds to the *approximate limit of practical validity of the linear theory* for initial perturbations with realistic amplitudes (*e.g.* Errico *et al.*, 1993). By "realistic amplitudes" we mean values up to roughly 15 m in the perturbation geopotential height. This range of

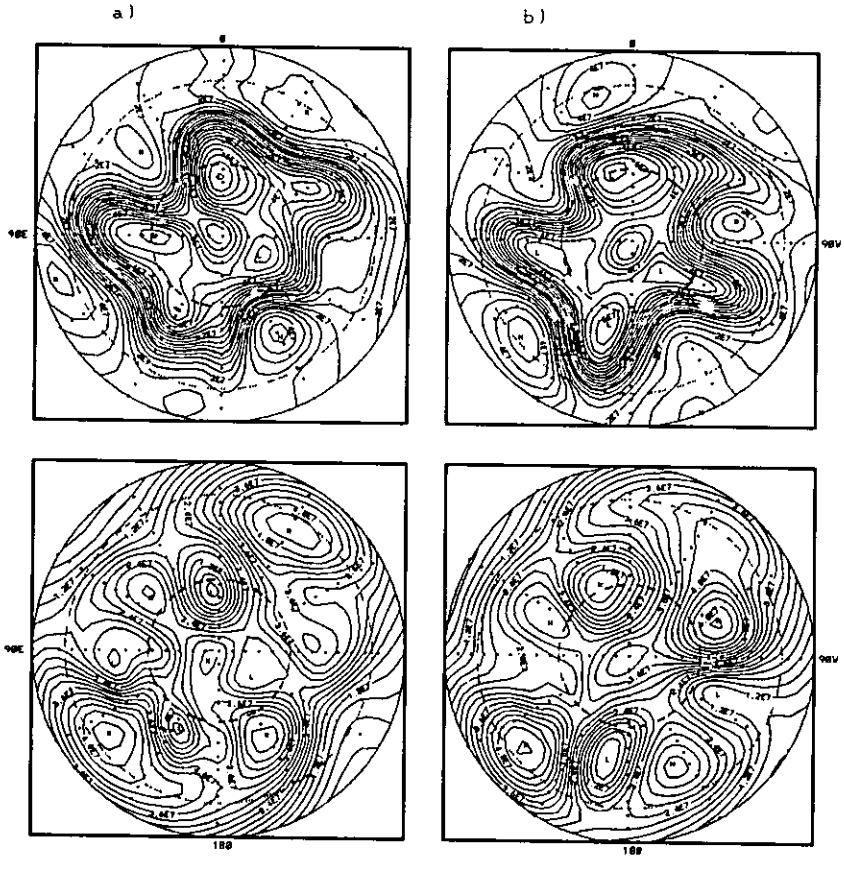

Figure 6: Upper (top panels) and lower-layer (bottom panels) streamfunction of day 1504 (column a) and day 1507 (column b). Contour interval $5 \times 10^6 m^2 s^{-1}$ for upper-layer and $3 \times 10^6 m^2 s^{-1}$ for lower layer. Boundary circle is 20°N and interior circles are 30°N and 60°N.

values corresponds to typical analysis errors of the upper levels (say 500 *mb*) in operational forecasts. Large values of $S_{max}(t_o)$ indicate that initial disturbances with large projection onto $\delta \mathbf{x}_{opt}(t_o)$ will cause large changes in the blocking index τ days later, while (very) small values of $S_{max}(t_o)$ indicate that the flow τ days later is (highly) predictable. If the flow is zonal, it will remain zonal, and if it is blocked, it will remain blocked, irrespective of the perturbation added to the control run at the initial time, as long as that perturbation evolves linearly between t_o and $t_o+\tau$. We see from Fig. 5 that *there are blocking episodes that are predictable*, for instance, the blocks which start on days 1507 and 1812. On page 52, we already referred to Fig. 6, which shows the upper and lower-layer streamfunction of day 1507. The streamfunction 3 days before the onset, *i.e.*, at day 1504, is also shown in the same figure. Fig. 5 also shows that there are *zonal regimes that are predictable*, for instance, between days 1770 and 1799. Fig. 7 shows the streamfunction pattern of day 1771, when the zonal regime has already set, and the streamfunction of day 1769, when the flow still contains a ridge around longitude 90° W. Very interestingly, Fig. 5 also shows that *there are blocked regimes and zonal regimes with a high potential to change from one type to the other*. For example, the optimal-block-triggering-perturbation superposed to the control run on day 1896 has a high probability of causing a block a few days later. Blocks excited by superposing perturbations onto the flow at day 1896 are the subject of a detailed study in Chapter 9. The streamfunction of the block-triggering-perturbation as well as the total streamfunction of the perturbed and unperturbed runs for this case are given in Figs. 20, 21 and 23, in Chapter 9.

Those days like 1584 and 1668, which are associated with large values of S_{max}, and for

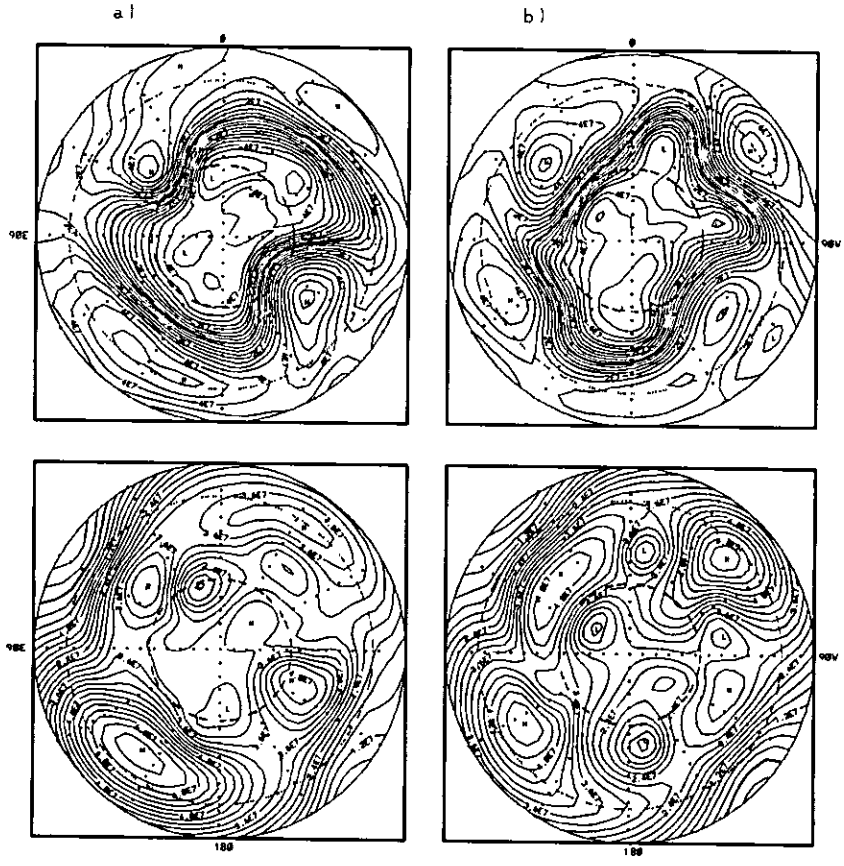

Figure 7: As in Fig. 6, except for days 1769 (column a) and 1771 (column b).

which the control run already shows a block, have a large potential to change from the blocked to the zonal regime. Within linear theory, it is obvious that the best initial perturbation to induce such a regime transition is the negative of the optimal-block-triggering-perturbation. Case study 1, to be presented in Chapter 8, features a block that occurs in the control run during a period of time of large sensitivity.

The overall picture presented here was found to hold for both values of π_β used in this work, and for blocks in both preferred geographical regions. This supports the notion that *some transitions to blocks are well predictable while others may be hard to predict.*

CHAPTER 8

Case Study 1. A Pre-Existing Episode. *Block*1750

Our first case study was performed on the block that occurs in the semi-hemisphere 0°-90°E-180°, starting on day 1750. The value of π_β is 0.9. The episode will be henceforth referred to as *Block*1750.

The trend of the maximal sensitivity for this semi-hemisphere (Fig. 8) indicates that, during the onset, the flow is very sensitive to perturbations with large projection onto the optimal-block-triggering-perturbation. Fig. 9 shows the upper and lower-layer streamfunction of the optimal-block-triggering-perturbation at the intial time, chosen to be day 1747, and at the final time. The optimization time is $\tau = 3$ days, and it was chosen in accordance with the discussion towards the end of the preceding Chapter, concerning the limits of practical validity of the linear theory. At the initial time, the perturbation is of sub-synoptic scale. The lower-layer is characterized by a wave train in the midlatitudes, between 60°W and 0°. At the end of the wave train, we see a high-low dipole centered around 60°E. The upper-layer features zonally elongated multipole structures between 90°W and 40°E. The structure, in both layers, resemble those found by Zou *et al.*, (1993) for the sensitivity of a Lejenäs-Økland (1989) type blocking index to 1% changes in the amplitude of the streamfunction at each grid point. At the final time, the perturbation has evolved into a larger scale pattern, reminiscent of an omega-type of blocking anomaly, and reveals a barotropic

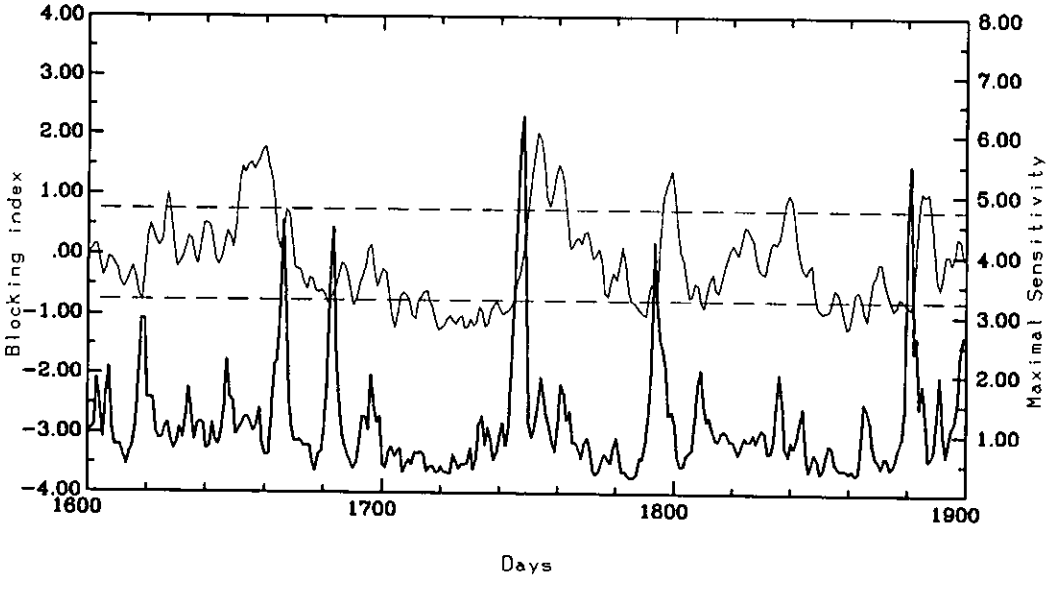

Figure 8: Time series of the blocking index (light line) and maximal sensitivity (dark line) between days 1600 and 1900. The geographical region considered is the semi-hemisphere 0°-90°E-180°. The value of π_β is 0.9. Values of the linear sensitivity are in units of $100 \times m^{-2}s$.

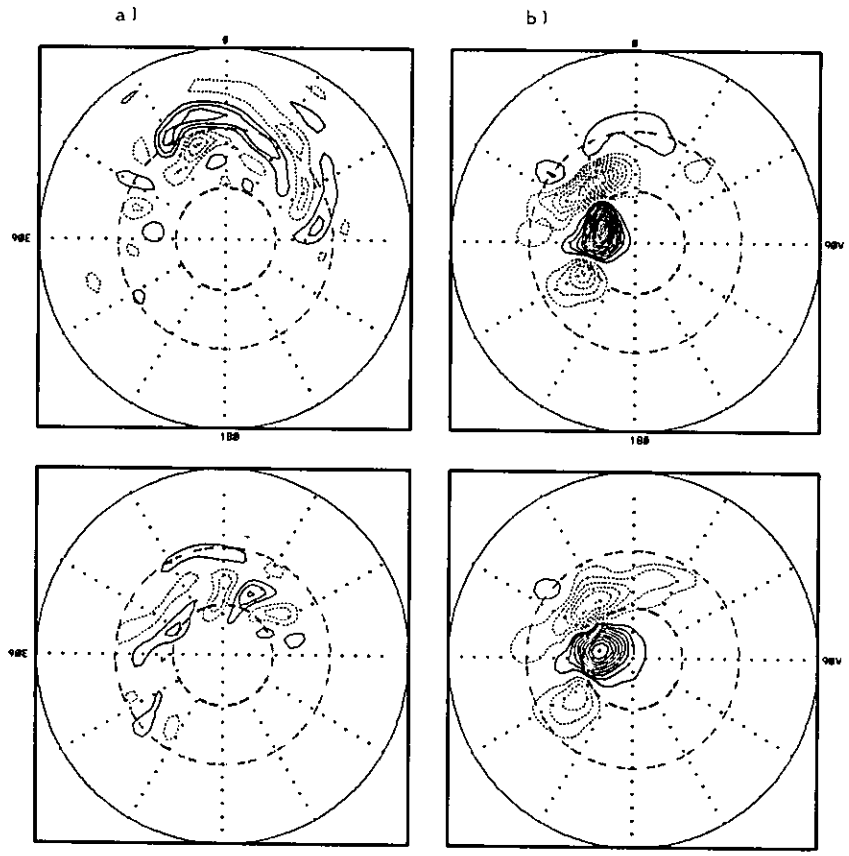

Figure 9: Upper (top panels) and lower-layer streamfunction (bottom panels) of the optimal-block-triggering perturbation at: initial time (day 1747) (column a, contour interval $5 \times 10^6 m^2 s^{-1}$ and $1 \times 10^5 m^2 s^{-1}$ for upper and lower-layer, respectively), final time (day 1750) (column b, contour interval $8 \times 10^6 m^2 s^{-1}$ and $4 \times 10^6 m^2 s^{-1}$ for upper and lower-layer, respectively). Zero line omitted, and dashed contours for negative values. The boundary circle is the equator and interior circles are 30°N and 60°N.

structure.

Oortwijn and Barkmeijer (1994) also found that the optimal-block-triggering-perturbations have, at the initial time, baroclinic structures with their energy concentrated in the sub-synoptic scales, and that this energy is transferred to lower wavenumbers within one day. They also found the structures to be barotropic at the optimization time.

As discussed by Buizza and Palmer (1995), singular vectors obtained in the energy norm (kinetic or total) are generally of smaller scale compared to those obtained by maximizing the enstrophy. The optimization is achieved through growth to larger scales, in accordance with the upscale cascade of energy, a result from the theory of two-dimensional turbulence. At this point, this allows us to speculate that the leading SV's calculated in the sense of the energy norm might capture most of the spatial variance of the optimal-block-triggering-perturbations, thus making them particularly useful in blocking predictability, in the context of an ensemble forecast. We will come back to this point in case study 2.

8.1 Synoptic Description of *Block*1750

Figs. 10 and 11 show the evolution of the upper and lower-layer potential vorticity (PV) (see Appendix A) and streamfunction, respectively, between days 1744 and 1761.

On day 1744, the upper-layer flow is fairly zonal in the semi-hemisphere 0°-90°E-180°, and shows an incipient ridge around 75° E, 60° N. This developing ridge is associated with the buildup of an upstream trough, at 40° E, 60° N. The latter results from the cyclonic PV-anomaly seen at the northernmost part of the trough. Downstream, at 100° E, 50° N, a well developed trough is present. It originated from the cyclonic wrap-up of a high PV-anomaly,

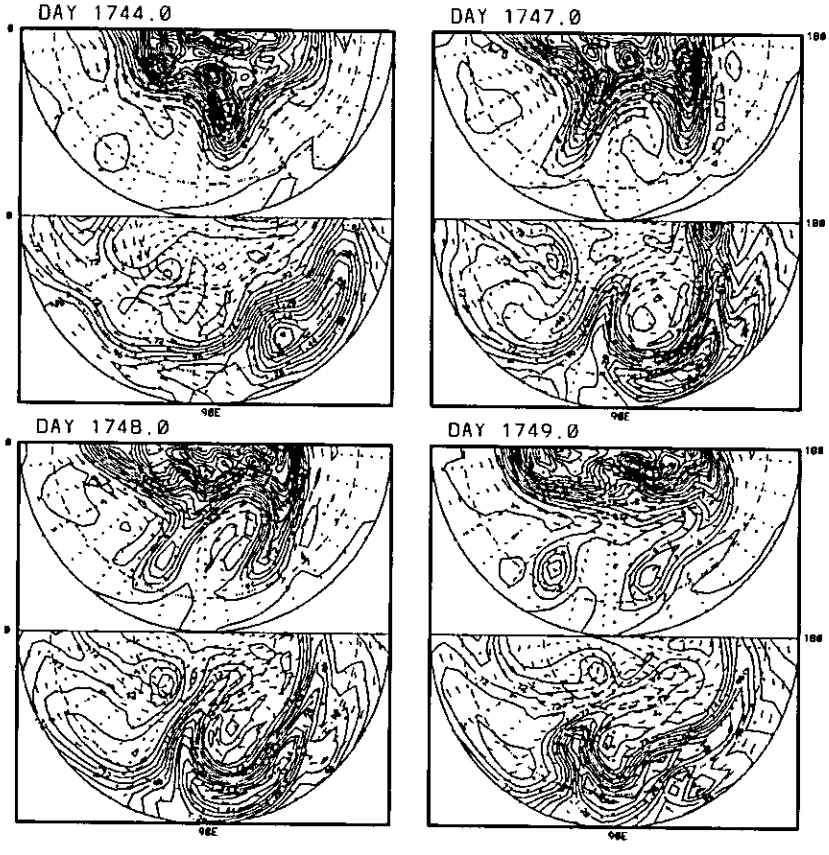

Figure 10: Time evolution of the PV of *Block*1750 between days 1744 and 1761. For each day shown, upper and lower-map are for upper and lower-layer, respectively. Fields have been multiplied by 1×10^6. Contour interval $0.2 m^2 s^{-1} K kg^{-1}$ for upper layer and $0.08 m^2 s^{-1} K kg^{-1}$ for lower layer. Also shown are arrows indicating the direction of the horizontal component of the velocity vector, with lengths proportional to the modulus of the velocity. The boundary circle is 20° and interior circles are 30°N and 60°N. Sectors are for the semi-hemisphere 0°-90°E-180°. Fields have been rotated 90° to the east with respect to Fig. 9.

accompanied by equatorward penetration of the PV-contours. A strong high PV-anomaly is also seen at 90° E, 70° N. The most intense PV-gradients are in the northernmost part of the jet, where it connects with the high PV-anomalies. We note that the upstream and downstream troughs have a meridional orientation at this time. In the lower-layer, there is a PV-ribbon between 30° N and 45° N that extends from roughly 20° E to 180° E. The largest PV-gradients in this layer occur north of the high PV-anomaly seen at 120° E, 30° N. In the course of the following 3 days, the upper-layer system of trough-ridge-trough moves some 30°downstream, and becomes more conspicuous. By day 1747, the troughs show signs of thinning and tendency for a $NE-SW$ orientation. The development of the westernmost trough in the upper layer is accompanied by a northeastward intrusion of the PV-ribbon in the lower layer, at 90° E. The $NE-SW$ orientation of the upper-layer troughs is more visible on day 1748. Their thinning and anticyclonic bend already suggests the formation of cutoff high PV-anomalies. In the westernmost trough, a closed contour of high PV has formed. By day 1749, the two high PV-anomalies associated with the equatorward breaking of the upper layer troughs are only umbilically connected to the main jet. The latter has an almost perfectly rectilinear shape around 60° N, between 30° E and 150° E.

The maps of the streamfunction show a weak high in the upper-layer at 90° E, 45° N, almost detached from the main jet, and a cutoff low both upstream and downstream. By day 1749.5 (not shown), the upstream high PV-anomaly, in the upper-layer, cuts off at 60° E, 40° N, while the downstream high PV-anomaly becomes attached to the main jet by only one contour line. Also on this day, lower PV from the southernmost part of the jet at about 30° E, along with debris of low PV from subtropical regions, are advected

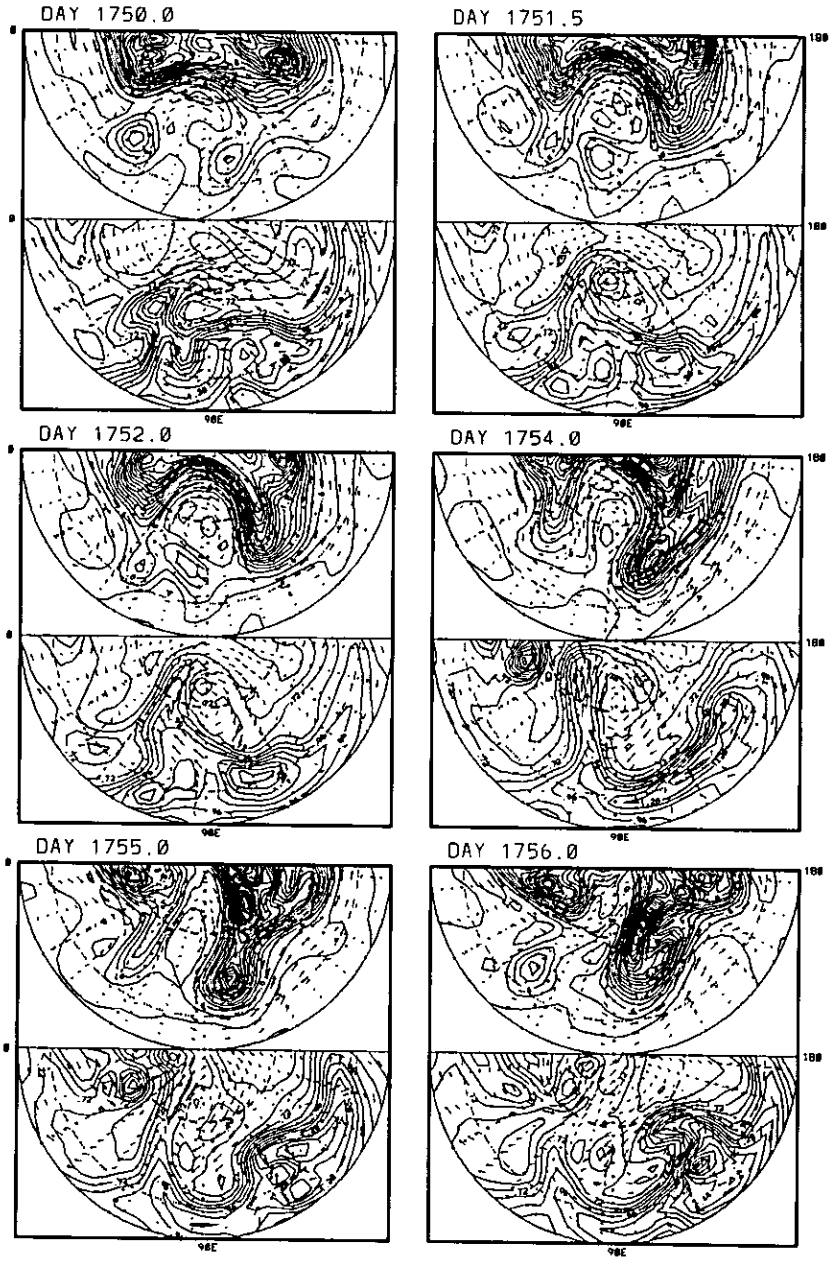

Figure 10: Continued.

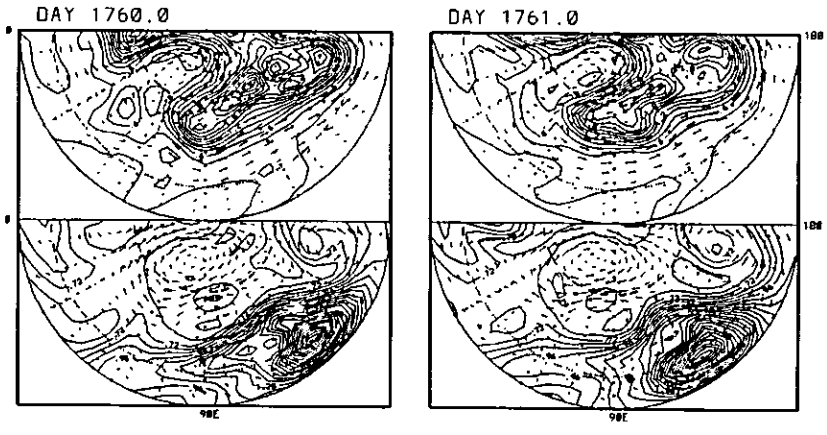

Figure 10: Continued.

into around 90° E, 65° N. This causes a rapid development of a ridge at 90° E, 65° N, starting on day 1750. In the following 24 hours the upstream cutoff cyclone in the upper-layer re-attaches to the main jet, while the downstream high PV-anomaly retrogrades. The latter connects to the upstream PV-anomaly and forms a perfect blocking dipole with the intense ridge that has developed at 90° E, 65° N (see PV and streamfunction charts of day 1751.5). The streamfunction charts show a highly barotropic structure throughout most of the duration of the blocking episode. As the cutoff process is in progress in the upper layer, the northeastward intruded PV-ribbon near 90° E in the lower layer breaks, and the PV contours form a mushroom type of frontal zone at 50° E, 45° N (day 1750). The intense upper-layer ridging that starts on day 1750 is accompanied by lower-layer advection of high PV, resulting in the PV-ribbon intruding as far as 85° N. On day 1754, the lower layer PV at 75° E, between 30° N and 85° N, shows a structure resembling baroclinic zones commonly seen on surface pressure and potential temperature charts, but with a reversed

T-bone bending. The blocking ridge has now a slight NE-SW orientation, as seen in the streamfunction charts. The PV-charts of day 1755 show that the upstream and downstream troughs in the upper layer start anew the process of thinning. However, while the upstream through again detaches from the main jet (day 1756.5, not shown), the downstream high PV reconnects strongly to the main jet, as seen on day 1756. By day 1758 (not shown), the upstream cutoff high PV-anomaly is re-attached to the main jet, and forms later the new blocking cyclone (*e.g.* streamfunction chart of day 1760). The block persists until roughly day 1762, while rotating westward.

The buildup of Block 1750, *as described above, seems to consist of two main stages.* In the first stage, we witness the formation of a cutoff (or near cutoff) upper layer cyclone at midlatitudes, both upstream and downstream of the location where the blocking ridge will form. This proceeded as the result of intense upper-layer cyclogenesis at the northernmost part of the regions of trough development. Also, a trough thinning with an anticyclonic bending takes place. As the process of upper-layer high PV cutoff is in progress, the lower layer PV-ribbon intrudes poleward. During the onset, a persistent advection of high PV, beneath the upper-layer blocking ridge, takes place in the lower layer.

The second step consists of a rapid intensification of the upper layer ridge, preceeded by advection of low PV by the mean jet to the location of the ridge. A retrogression of the easternmost (nearly) cutoff high PV-anomaly and eventual connection with the upstream cutoff high PV-anomaly occurs to form, together with the intense ridge, a classical blocking pattern. Alternatively, the upstream cutoff high PV can per se form the high PV of the blocking dipole (*e.g.* day 1760).

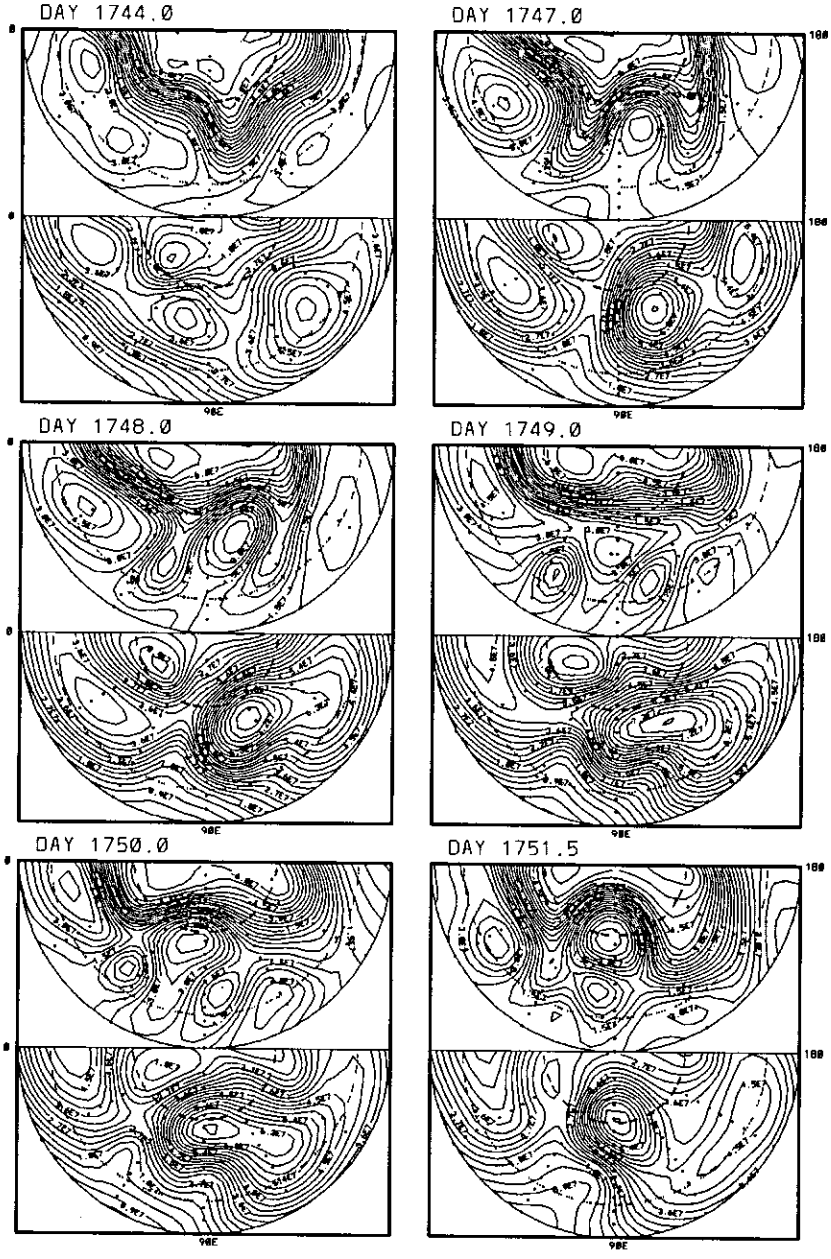

Figure 11: As in Fig. 10, except for the streamfunction. Contour interval $5 \times 10^6 m^2 s^{-1}$ for upper-layer and $3 \times 10^6 m^2 s^{-1}$ for lower-layer.

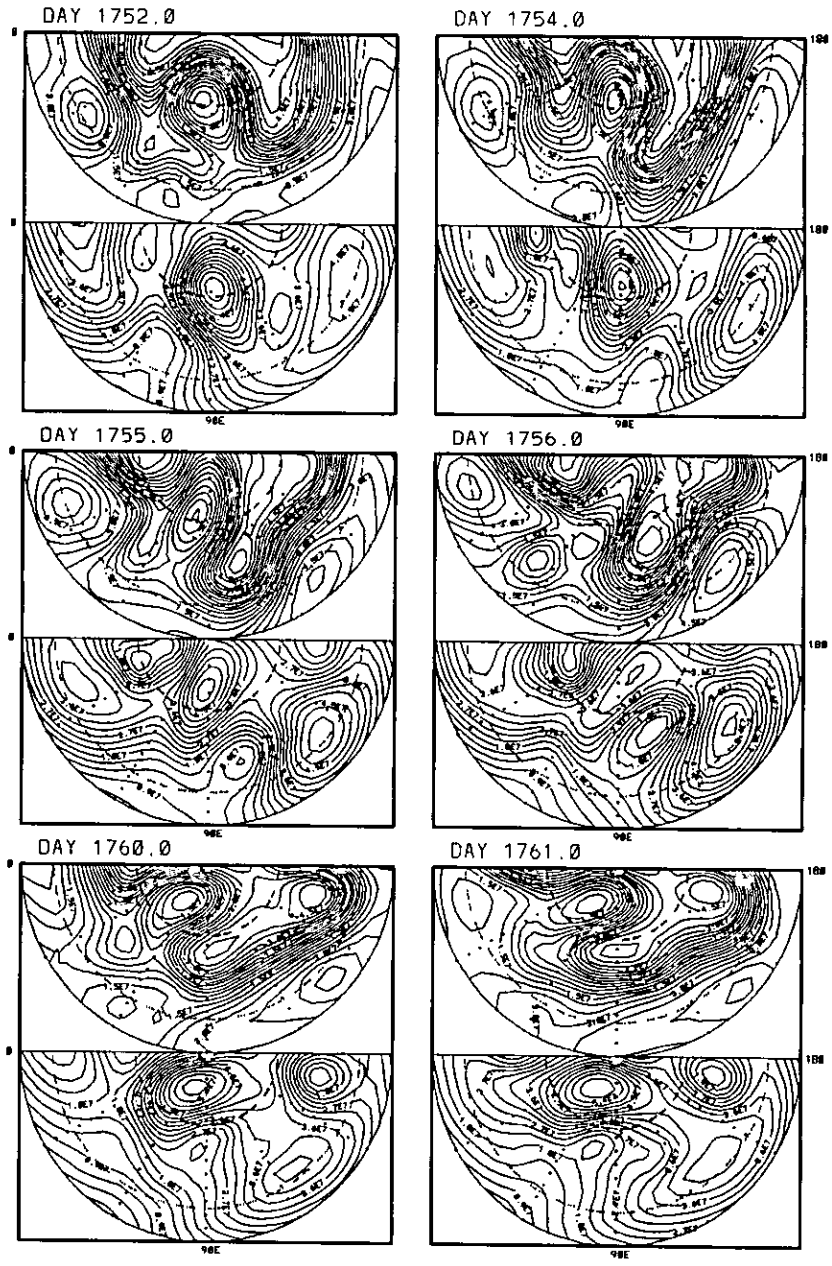

Figure 11: Continued.

8.2 Normal Modes of Day 1747

The nonlinear solution at day 1747 was extracted, and an eigenanalysis was performed. Day 1747 corresponds to roughly 3 days back in time, before the onset of the block. The justification for performing linear theory on time intervals of 3 to 4 days was given towards the end of Chapter 7.

Fig. 12 shows the eigenvalue spectrum in complex space for periods greater or equal to 0.6 days. A total of 14 growing modes is obtained with a T20 truncation. Here *caution must be exercised.* Calculations with the full T31 truncation show that the model truncated at T20 in general yields normal modes with smaller growth rates and larger periods than the T31-counterparts. Variations of up to 20% in both the growth rate and the period were found. This result is not new. Mak and Cai (1989) found similar variations with truncation in a barotropic quasi-geostrophic model on a β-plane. They found, however, no severe changes in structure. In our model, the first few modes have virtually the same structure in both truncations. The correctness of the eigenanalysis was checked by superposing selected normal modes onto the basic state, and integrating the linear model with time invariant basic state over one period of the normal mode. By definition of a normal mode, apart from a multiplying factor on the envelope amplitude, the structure has to repeat itself every period. This was found to hold extraordinary well in our calculations. Integrations of the T20-normal modes on the model truncated at T31 also revealed that the most rapidly growing modes are, to a good approximation, normal modes of the T31 truncated model. One should bear in mind, however, that T20-modes which are slightly decaying might be

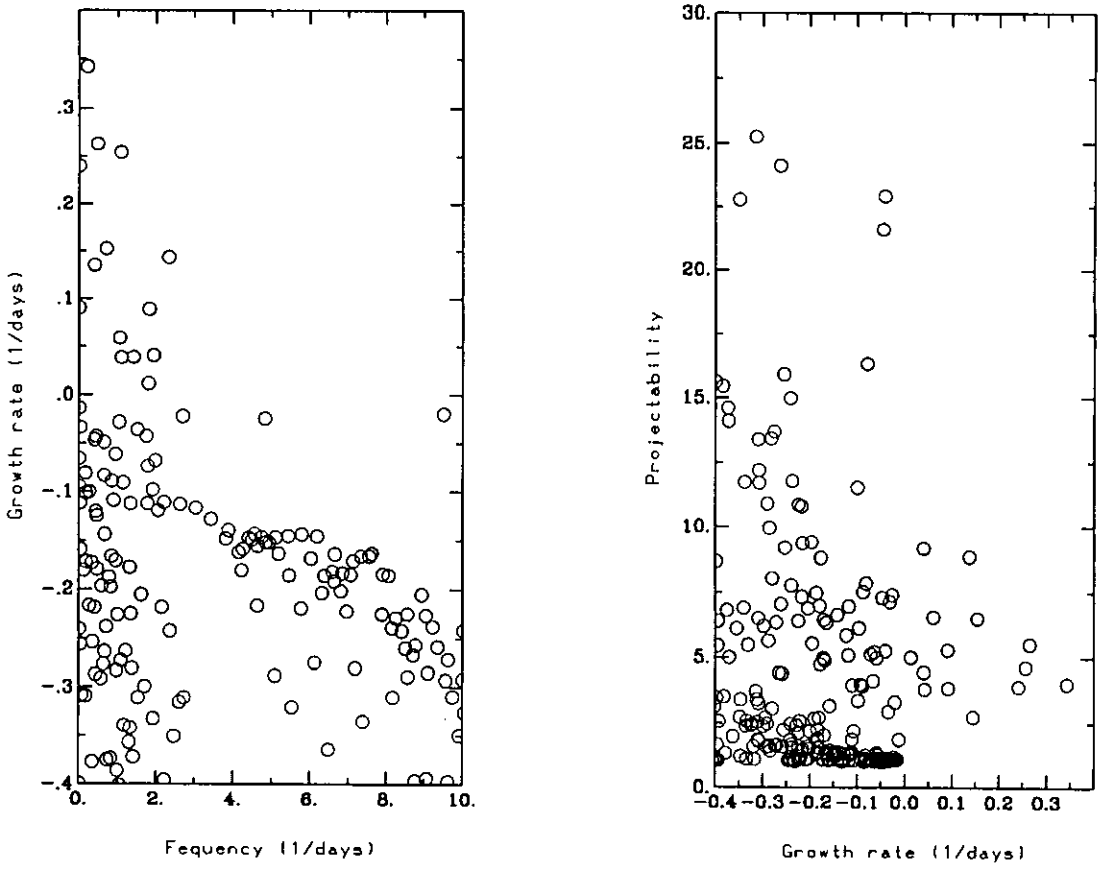

Figure 12: Left panel: The eigenvalue spectrum for the primitive equation model linearized about day 1747, with $\pi_\beta = 0.9$ and a T20 resolution. The abscissa spans a portion of the total frequency range which corresponds to periods greater or equal to 0.6 *days*. Right panel : The projectability vs the growth rate.

substantially growing in the model truncated at T31.

Fig. 12 also shows the projectability of each normal mode. We see that some of the normal modes which are far distant in the spectrum, *i.e.*, when ordered by decreasing order of the growth rates, are likely to be important in eigenvalue problems. We also see that a very large number of normal modes have projectabilities close to 1. Whether or not this is of any physical consequence needs further investigation. We recall that, according to the

concept of projectability, *these modes form a subset which is close to being orthogonal in the sense of the total energy.* These modes practically do not exchange energy with other modes, and therefore do not participate in the growth phase of perturbations other than by exponential growth or decay.

The fastest growing normal mode (FGNM) has a growth rate of 0.3425 day^{-1}, a period of 30.12 days and a projectability of 4.02. In view of its relatively small projectability, if this mode is to be excited in an eigenvalue problem, then exponential growth is likely to be the dominant mechanism of growth at all stages of the excitation. Fig. 13 shows the upper and lower-layer streamfunctions of the real and imaginary phases of this normal mode. Notice the well defined dipole structure in the imaginary phase at the location of block formation some 3 days later.

The FGNM is an example of what Frederiksen and Bell (1990) call an onset-of-blocking mode (see also Frederiksen and Bell 1987). These authors have classified the instability modes growing on instantaneous basic states for January 1978 on the basis of their periods, scales and structures. Cyclogenesis modes were classified as small-scale westward tilting shallow disturbances which tended to have a single maximum in their amplitude in the meridional direction and which had periods between 1 and 5 days. Onset-of-blocking modes were slightly larger-scale, less shallow disturbances, with some vertical tilt, with dipole or multipole structures in the meridional direction in some regions, and with periods between 5 and 10 days. Mature anomaly modes were the largest-scale equivalent barotropic modes with periods larger than 20 days. Intermediate modes were modes with periods and scales intermediate between the onset-of-blocking and the mature anomaly modes.

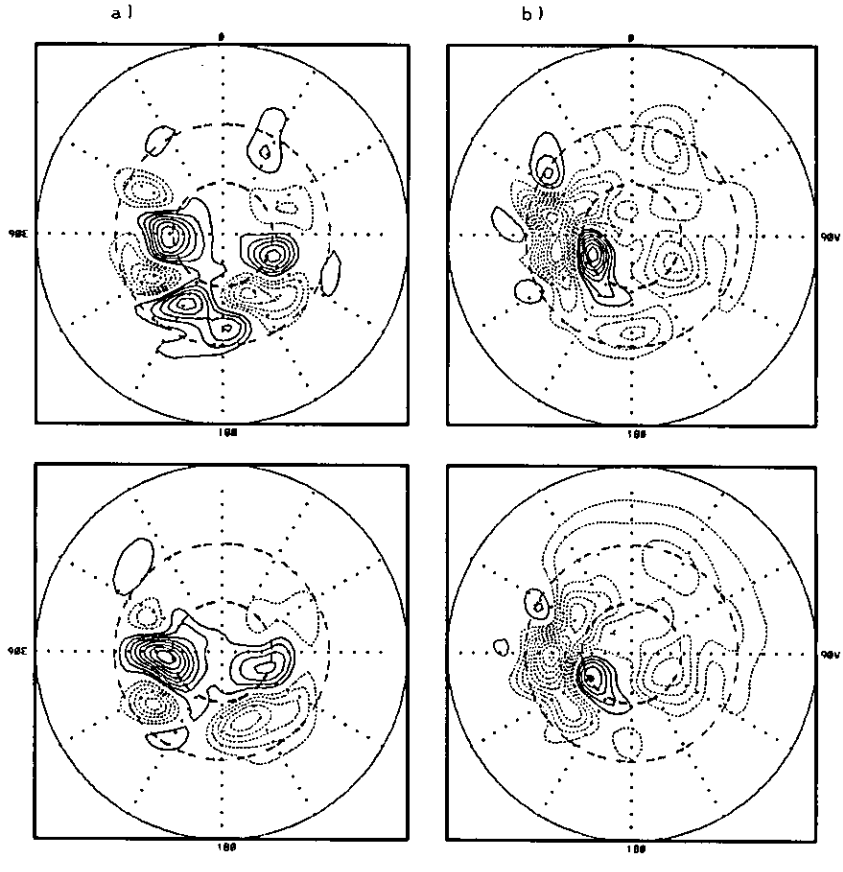

Figure 13: Upper (top panels) and lower-layer streamfunction (bottom panels) of the real phase (column a) and imaginary phase (column b) of the FGNM of day 1747, with $\pi_\beta = 0.9$. Both phases have been normalized to have an integrated total energy of 1 $Jkg^{-1}m^2$. Contour interval $7 \times 10^5 m^2 s^{-1}$ for the upper-layer and $3.5 \times 10^5 m^2 s^{-1}$ for the lower-layer. Zero contour omitted, and dashed contours for negative values. The boundary circle is the equator and interior circles are 30°N and 60°N.

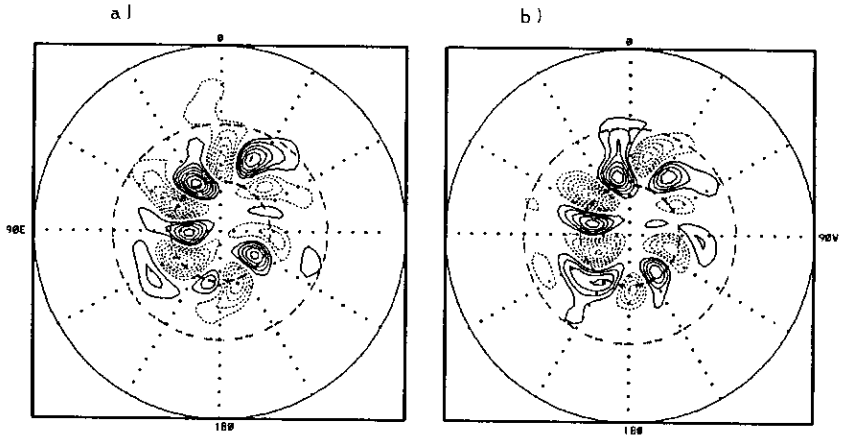

Figure 14: Upper-layer streamfunction of the a) real and b) imaginary phase of the sixth normal mode. Both phases have been normalized to have an integrated total energy of $1\,Jkg^{-1}m^2$. Contour interval $5\times10^5 m^2 s^{-1}$. Zero line omitted, and dashed lines for negative values. Boundary circle is the equator and interior circles are 30°N and 60°N.

The various calculations performed on our model yield an overall picture which agrees well with that of Frederiken and Bell (1990). Shortcomings are in the actual magnitudes of the periods, as discussed above. A better agreement requires that the eigenanalysis be performed with the full T31 truncation. To make the point that a rich variety of structures and scales is also obtained with the T20-truncation, we show in Fig. 14 the two phases of the upper-layer streamfunction of mode 6. This mode has a period of 2.71 days and a growth rate of 0.1439 day^{-1}. It represents a cyclogenesis mode. For later convenience, we show in Figs. 15 and 16 the streamfunctions of the FGNM and second mode of day 1749, respectively. In Fig. 17 we show the streamfunction of the FGNM of day 1750 and of its adjoint. These modes are discussed in Chapter 10.

A detailed characterization of all and each one of the normal modes is not the objective of this work. Rather, we perform a sensitivity study to identify the modes that more strongly

impact on the formation (or demise) of the block. A few general remarks are however useful:

With the actual parameter set, all T20 growing modes calculated on different basic states, during this investigation, where found to possess a barotropic structure. Baroclinic structures were only found in some decaying modes, distant in the spectrum. Also, all initial value problems performed with initially baroclinic perturbations (not necessarily of modal form) resulted in barotropic structures in less than 24 hours of integration. However, the eigenanalysis on the drive state, *i.e.*, on the state defined by prescribing the equilibrium interface Exner-thickness (see Appendix A), revealed that this state is baroclinically unstable. The most unstable mode possesses a wavenumber 7 in the zonal direction. This suggests that the upscale energy transfer, which leads to the barotropization of the disturbances occurs in a rather quick fashion in this model. Furthermore, in all cases analysed, the largest amplitudes of the normal modes were found in the upper-layer, suggesting, in particular, that the phenomenon of surface explosive cyclogenesis is not likely to be seen in this model. This may be due to an intrinsic deficiency of this model.

8.3 Sensitivity Analysis on *Block*1750. The Mechanism of Initial Growth

Tables 1, 2 and 3 show the relative sensitivity (RS) of the blocking index to the normal modes of day 1747. The RS was calculated at days 1749, 1750 and 1751, respectively. For the definition of the relative sensitivity we refer the reader to equation (54), in Chapter 6. The projectabilities, expansion coefficients, and the phases of the normal modes are also shown in the tables. We recall that a non-stationary normal mode contributes with two

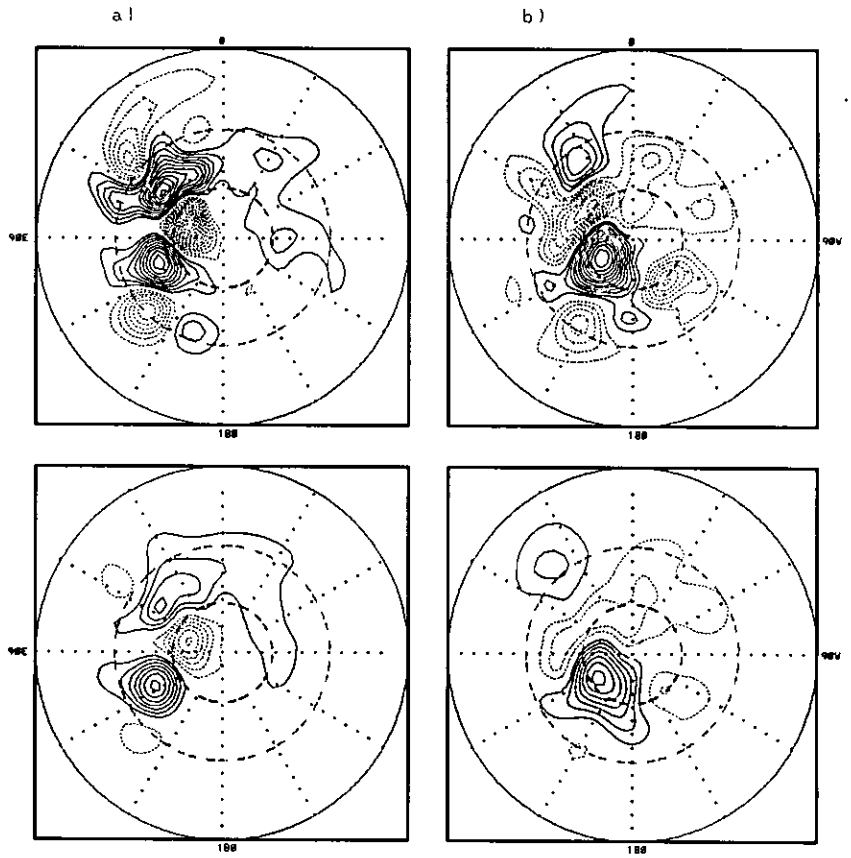

Figure 15: As in Fig. 13, except for the FGNM of day 1749. Contour interval $5 \times 10^5 m^2 s^{-1}$.

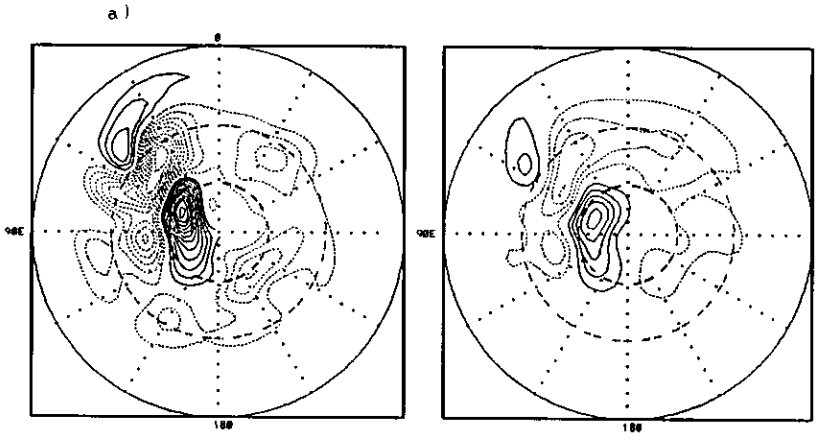

Figure 16: As in Fig. 15, except for the second normal mode of day 1749. This mode is stationary. Left panel represents upper-layer and right panel displays lower-layer. Contour interval $5 \times 10^5 m^2 s^{-1}$.

orthogonal phases (functions) to the expansion base, while a stationary mode contributes with just one phase.

All three tables reveal that only one phase of a given non-stationary mode is associated with a large value of the RS. This leads to the conclusion that, in general, the initial phase is crucial in asserting whether or not a normal mode is capable of producing large changes in the direction of phase space corresponding to a block. In particular, this suggests that conclusions drawn upon averaged quadratic quantities computed from the normal modes, a procedure referred to as the *Random Phase Ensemble Average (RPEA)* (*e.g.* Frederiksen 1979), are not of much utility in the problem at hand. It must be mentioned that in most cases analysed here the real and imaginary phases of the normal modes contained

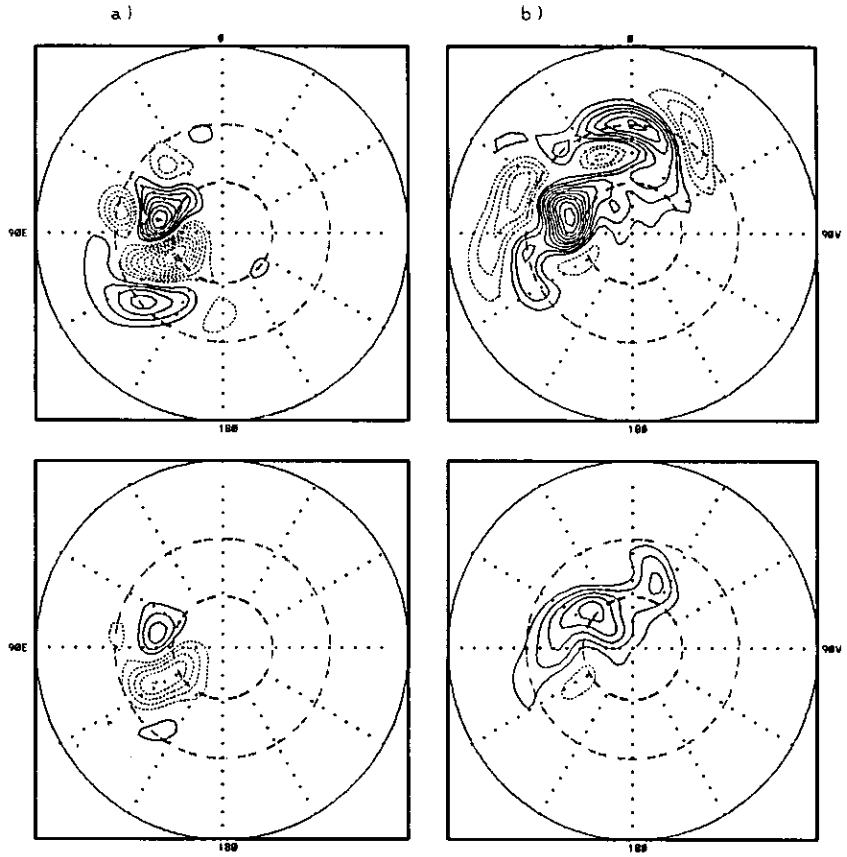

Figure 17: Left panels: streamfunction of the FGNM of day 1750. This mode is stationary. Right panels: streamfunction of the corresponding adjoint. Upper panels represent upper-layer and lower-panels display lower-layer. Contour interval $1 \times 10^6 m^2 s^{-1}$.

Table 1: Values of the relative sensitivity (RS) to the normal modes of day 1747 calculated on day 1749. In the first column, from left, are the normal mode numbers (ordered by decreasing values of the growth rates), in the second column the basis function numbers, in the third column the phase of the normal mode (R for real phase, I for imaginary phase and S for stationary mode), in the fourth column the expansion coefficients, in the fifth column the values of the RS and in the sixth column the projectabilities. Only cases in which $|RS| > 0.05$ are shown.

Nmode	function	phase	Exp. coeff.	RS	γ
1	1	R	+4.70	+0.0576	4.02
5	9	I	+27.62	-0.0652	6.51
15	27	S	-27.14	-0.3166	1.88
50	97	I	-87.82	+0.0892	7.14
67	131	I	+183.61	-0.0672	22.94
72	141	I	+67.02	-0.0877	1.14
78	153	I	+222.85	+0.0837	21.61
88	172	R	-20.76	-0.0744	7.30
146	286	R	+89.55	+0.0681	3.96
180	355	I	-18.37	+0.1014	3.17
232	458	R	+12.94	+0.0554	6.40
369	730	I	-7.82	-0.0879	6.16
436	863	I	+53.28	-0.0788	46.12
669	1318	I	+0.06	-0.0796	2.54

Table 2: Same as in Table 1, except for the sensitivity on day 1750. Only cases in which $|RS| > 0.1$ are shown.

Nmode	function	phase	Exp. coeff.	RS	γ
5	9	I	+27.62	-0.1146	6.51
7	12	R	+27.06	-0.1063	8.86
15	27	S	-27.14	-0.3372	1.88
67	131	I	+183.61	-0.1038	22.94
78	153	I	+222.85	+0.1412	21.61
88	172	R	-20.76	-0.1303	7.30
180	355	I	-18.37	+0.1256	3.17
262	518	I	-5.77	+0.1036	13.44
306	605	R	+19.35	-0.1174	15.46
369	730	I	-7.82	-0.2161	6.16
552	1091	I	-7.69	+0.1095	8.67
612	1208	I	-1.28	+0.1133	7.48
669	1318	I	+0.06	-0.3583	2.54

Table 3: Same as in Table 1, except for the sensitivity on day 1751. Only those 18 cases of largest $|RS|$ are shown.

Nmode	function	phase	Exp. coeff.	RS	γ
5	9	I	+27.62	-0.1620	6.51
15	27	S	-27.14	-0.3184	1.88
78	153	I	+222.85	+0.1640	21.61
136	267	R	-12.46	+0.1732	3.94
191	376	R	-22.32	+0.1654	4.90
262	518	I	-5.77	+0.1650	13.44
306	605	R	+19.35	-0.1971	15.46
369	730	I	-7.82	-0.2246	6.16
496	982	R	+0.92	+0.1508	7.92
552	1091	I	-7.69	+0.2209	8.67
561	1108	I	-0.06	-0.1595	7.76
605	1194	R	-3.04	+0.1792	12.43
612	1208	I	-1.28	+0.2231	7.48
628	1238	I	+0.34	-0.1694	2.97
656	1293	I	+0.95	+0.2205	3.08
662	1303	R	-0.65	-0.1565	1.85
663	1305	R	-0.50	-0.1711	2.43
669	1318	I	+0.06	-0.8269	2.54

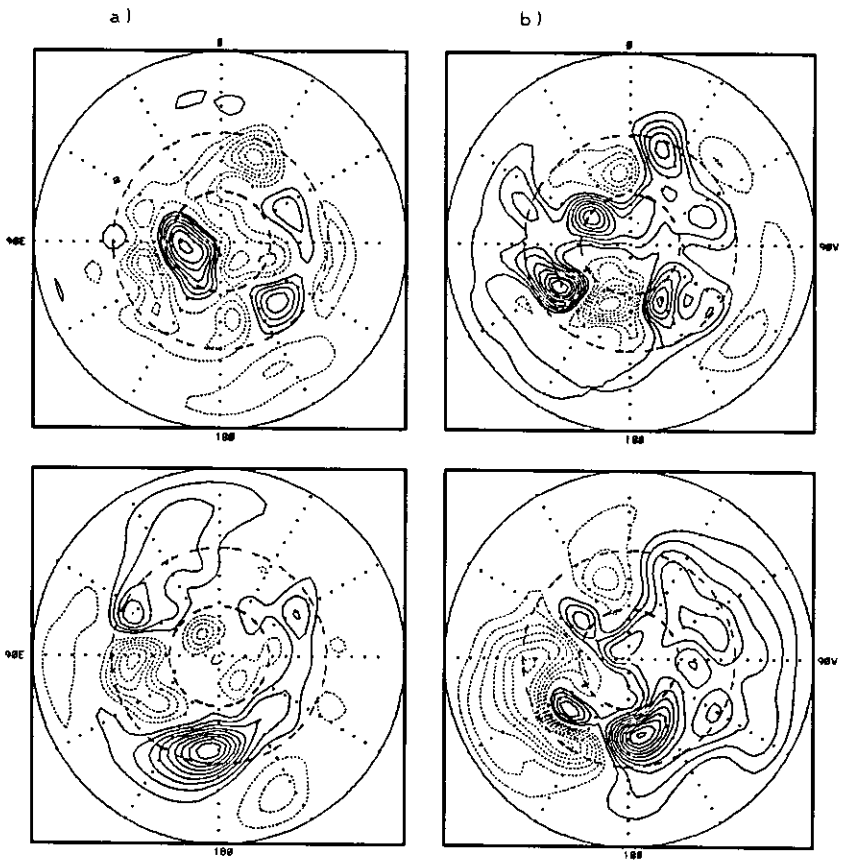

Figure 18: As in Fig. 13, except for the 78^{th} normal mode. Contour interval $5 \times 10^5 m^2 s^{-1}$ for upper-layer and $2.5 \times 10^5 m^2 s^{-1}$ for lower-layer.

comparable maxima in the amplitude. Since the RPEA is obtained by simply squaring the amplitudes in the two phases and adding them together, it follows that both phases give comparable contributions to the RPEA.

We also note that there are some phases of a given normal mode which appear in the three tables (*e.g.* functions 27 and 153), while others do not (*e.g.* functions 1 and 180), and that the relative importance of the different functions can vary from day to day (*e.g.* function 27 induces a larger change in the response function on day 1749 than function 1318,

but the reverse takes place on days 1750 and 1751).

It is very remarkable that modes well distant in the spectrum can be dominant (or nearly dominant) in their relative importance (as defined by the RS). For instance, this is the case of mode 180 on day 1749 and mode 669 on days 1750 and 1751.

If a certain normal mode plays a major role in the transition to the blocked state, then it is reasonable to expect that it can also prevent the formation of the block if excited with the opposite sign. Integrations of the model with the initial condition (flow of day 1747) perturbed by some of the structures found in Tables 1, 2 and 3 were performed. It was found that those structures that successfully prevented the formation of the block had to have an initial amplitude corresponding to maximum perturbations winds of $5ms^{-1}$ or stronger. We took the value of $10ms^{-1}$ as the upper limit in our experiments. It corresponds to the observational maximum zonal wind anomalies of Dole and Black (1990) prior to their composite onset. Initial maximum perturbation winds in the range of $5ms^{-1}$ to $10ms^{-1}$ are associated, in our model, with a linear evolution of the perturbations for not more than 72 hours. Perturbation winds of this magnitude are to be considered strong. Assuming a random distribution of initial error, in a forecast context, one should not expect large projections onto the normal modes to occur very often. The concept of projectability is useful in this regard. In view of the fact that strong initial perturbation winds are needed in order to prevent the formation of the block, one should be looking at those structures that are present in the three Tables 1, 2 and 3, and that possess large projectabilities. Clearly, when it comes to the leading modes, exponential growth should be carefully considered, independently of the projectability.

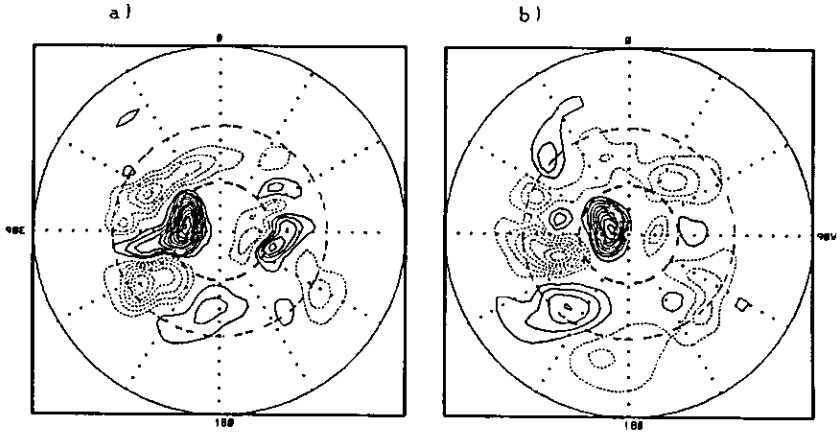

Figure 19: Evolution of the imaginary phase of the 78^{th} normal mode of day 1747 integrated on the nonlinear model, starting on day 1747. The initial perturbation was normalized to have maxima of $2.5ms^{-1}$ in the wind field. Shown are the upper-layer streamfunctions of the perturbation on day 1750 (panel a, contour interval $6 \times 10^5 m^2 s^{-1}$) and day 1752 (panel b, contour interval $1.2 \times 10^6 m^2 s^{-1}$). Boundary, interior circles and dashed lines as in Fig. 9.

We have concentrated on the imaginary phase of mode 78 (function 153). In the T20 truncated model this mode has a growth rate of $-0.04591\, day^{-1}$, a period of 15.61 days and a projectability of 21.61. Fig. 18 shows the upper and lower-layer streamfunctions of the real and imaginary phases of this mode. Baroclinicity is apparent in both phases.

The initial amplitude of the imaginary phase was chosen by imposing a $2.5ms^{-1}$ maximum initial perturbation wind. This ensured a linear evolution for the first 4 to 5 days. Fig. 19 shows the upper-layer streamfunction of the perturbation at days 1750 and 1752. The structure is barotropic, with less amplitude in the lower-layer (not shown).

It is important to mention that although the 78th normal mode is slightly decaying on the T20 truncated model, it is largely growing in the T31 version. We see how amazingly well the perturbation at day 1750 resembles the optimal-block-triggering-perturbation at

the optimization time (Fig. 9). This strongly suggests that this mode might have been crucial in the buildup of the block. Additional support to this inference is the fact that blocking onset is prevented if we repeat the initial value problem, but with the reverse sign for the initial perturbation, and with an initial amplitude corresponding to a $5ms^{-1}$ maximum perturbation wind. Notice also the very large value of the expansion coefficient for the imaginary phase of this normal mode (222.85). It is the largest (absolute) value for the whole set of basis functions. It is necessary to bear in mind that although the projectability acts to "amplify" the expansion coefficient (see equations (47) and (48)), its value *per se* is insufficient to characterize the trend of expansion coefficients. In our case, for instance, the largest projectability occurs for mode 442 and has a value of 68.70 (not shown in the tables). However, the expansion coefficient corresponding to this mode (real phase) is -117.86, which has an absolute value smaller than that for the imaginary phase of the 78^{th} normal mode.

It must be stressed that a sensitivity study can only pinpoint the relative importance of the structures that we are studying, but that the real effect on the flow evolution can only be determined by actually integrating the model. It happened in this case study that the real phase of the FGNM, which is not present in neither Table 2 nor 3, was successful in preventing the block formation, when integrated with an initial amplitude corresponding to a maximum perturbation wind of $10ms^{-1}$. Clearly, this is indicating that, in this example, values of the RS smaller than the values presented in Tables 1, 2 and 3 must be considered if one is interested in isolating all the normal modes which can produce or destroy a block in the course of a three to four-day integration.

The normal modes growing on the flows of day 1746 and day 1748 were also calculated, and the sensitivity of the response function to these structures was evaluated. The findings were very similar to those for the normal modes of day 1747. *These findings can be summarized as following:*

The model truncated at T20 yields a variety of modes which correspond fairly well to the modes obtained by Frederiksen and Bell (1990) on observed instantaneous three-dimensional basic flows. Shortcomings are in the relatively smaller growth rates and larger amplitudes obtained in our model with a T20 truncation. A more quantitative agreement with the results of Frederiksen and Bell (1990) implies the use of the full T31 truncation. The sensitivity studies to the normal modes growing on flows that preceeded the onset of the block revealed that the information concerning the phase of the normal mode was essential in determining the effect of the normal mode on the response function. Consequently, a Random Phase Ensemble Average, which essentially assumes an equal probability of all phases, can lead to erroneous conclusions. It was also found that modes distant in the spectrum could induce changes in the response function that are comparable or even larger than those due to the leading modes. In particular, even though the reduced truncation in the eigenanalysis implies a note of caution, this result suggests that ensemble forecasts that rely on the first few growing normal modes to construct the ensemble of initial perturbations can be very deficient in accounting for the transition to the blocked state. If the normal modes are at all relevant to blocking, then the mechanism of initial growth seems to be capable of playing an important part, so that distant (growing or decaying) modes with large projectabilities should also be considered when constructing the ensemble.

We postpone until Chapter 10 the discussion of the two phases of the block onset mentioned in section 8.1.

CHAPTER 9

Case Study 2. *Block*1899

Case study 1 allowed us to study the importance of the mechanism of initial growth in comparison with exponential growth. However, in that case study further insight into the mechanisms of blocking is difficult to obtain, *since the block episode was already in the control run.* As mentioned in section 1.1, a fundamental problem of numerical weather prediction is that of correctly capturing the transition to the blocked state. It is thus more relevant to perform studies on blocks excited by some suitable perturbation during periods of time in which the control run does not exhibit any blocks. To pursue this line of attack, we identify in the time series of the maximal sensitivity and blocking index periods of time which correspond to a zonal flow with large values of the linear sensitivity. These are the periods of time where a block is likely to be excited.

We performed studies on the semi-hemisphere 0°-90°W-180°. The time series of the response function and maximal sensitivity (Fig. 5) were discussed in Chapter 7, to which we refer the reader. For reasons not clear, we found in this semi-hemisphere more cases of large maximal sensitivities associated with zonal flows than in the opposite semi-hemisphere. We note however that, because the control runs did not exceed 2100 days, we cannot reach any final conclusions regarding the relative likelihood of blocking in each semi-hemisphere.

The time series of Fig. 5 suggest that day 1896 might be a good initial state, free from

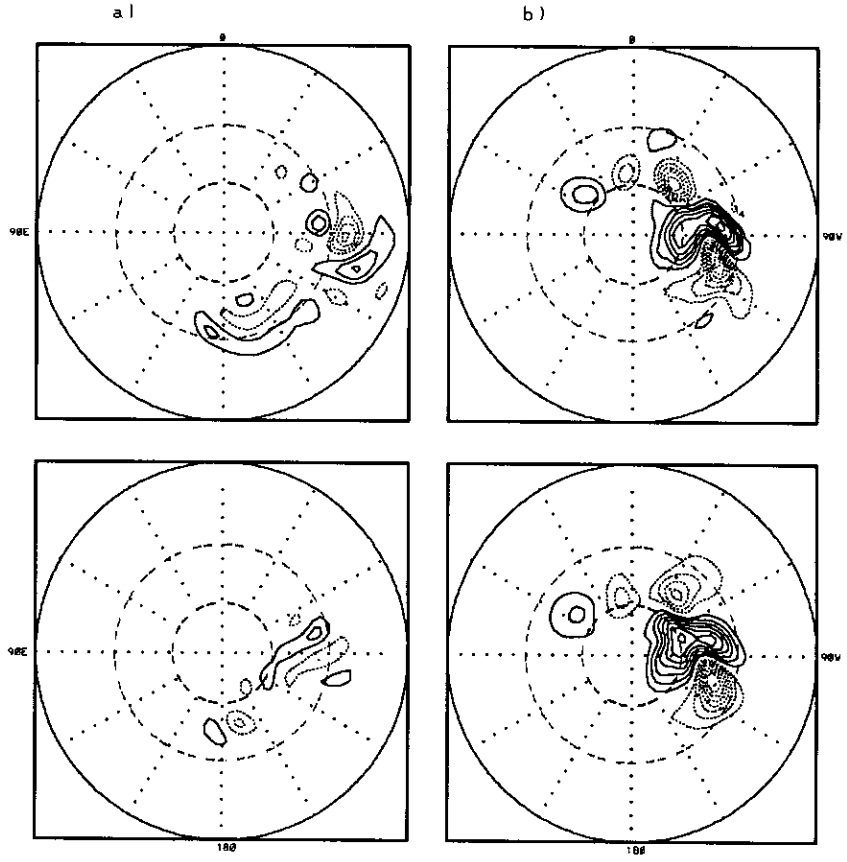

Figure 20: As in Fig. 9, except for the optimal-block-triggering-perturbation calculated on day 1896 (column a). The final day is 1899 (column b).

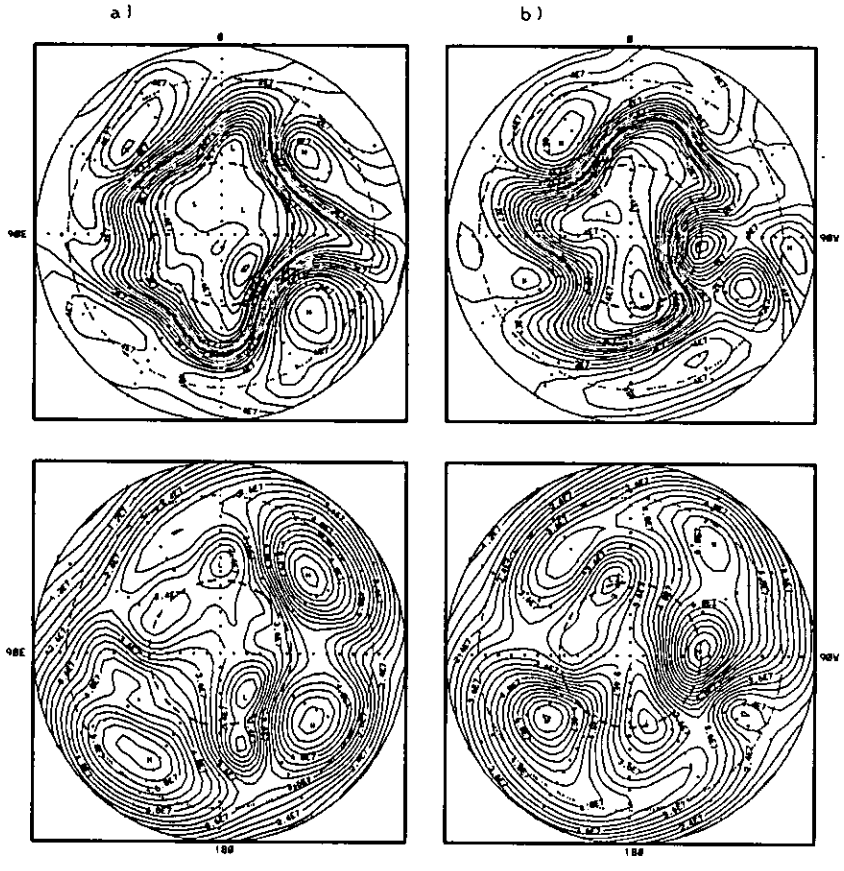

Figure 21: As in Fig. 6, except for days 1896 (column a), 1899 (column b). The initial condition was perturbed with the optimal-block-triggering perturbation, normalized to have maxima of $10ms^{-1}$ in the perturbation wind field.

any block, to perform our experiments. By perturbing the control run at this day with the optimal-block-triggering-perturbation, optimized over 3 days, we find that a block is excited some three days later. Fig. 20 shows the perturbation streamfunction at days 1896 and 1899, and Fig. 21 shows the total streamfunction of the perturbed run on days 1896, 1899, 1900 and 1903. The streamfunction of the unperturbed run (control run) is shown in Fig. 23. The initial perturbation was normalized to have maximum winds of $10ms^{-1}$. In view of the fact that the optimal-block-triggering-perturbation is able to excite a block, we hope that some of the structures of interest will be able to trigger the transition as well. *Any block excited by perturbing the model state on day 1896 will be henceforth referred to as Block*1899.

9.1 Synoptic Description of the Control Run. *Block*1899

The PV-maps (Fig. 22) show an upper-layer ridge on day 1896, at about 135° W, 45° N. The strongest PV-gradients are to the north. A strong high PV-anomaly is present at 135° W, 75° N, adjacent to the main jet, and reinforcing the strength of the latter. The lower-layer shows the development of a cyclone in the frontal zone, at about 160° W, 50° N. A closed circulation has already formed by day 1896.5 (not shown), at 150° W, 50° N. The PV-gradients are somewhat stronger on the western side of the frontal zone during this development. The lower-layer cyclone moves northeastward without intensifying. It is roughly at 135° W, 60° N on day 1897, and it becomes a cutoff cyclone by day 1898, at 100° W, 70° N. It subsequently decays, as it moves further to the east. This development is not repeated in the following days. The elongated poleward intrusion of the PV-ribbon left

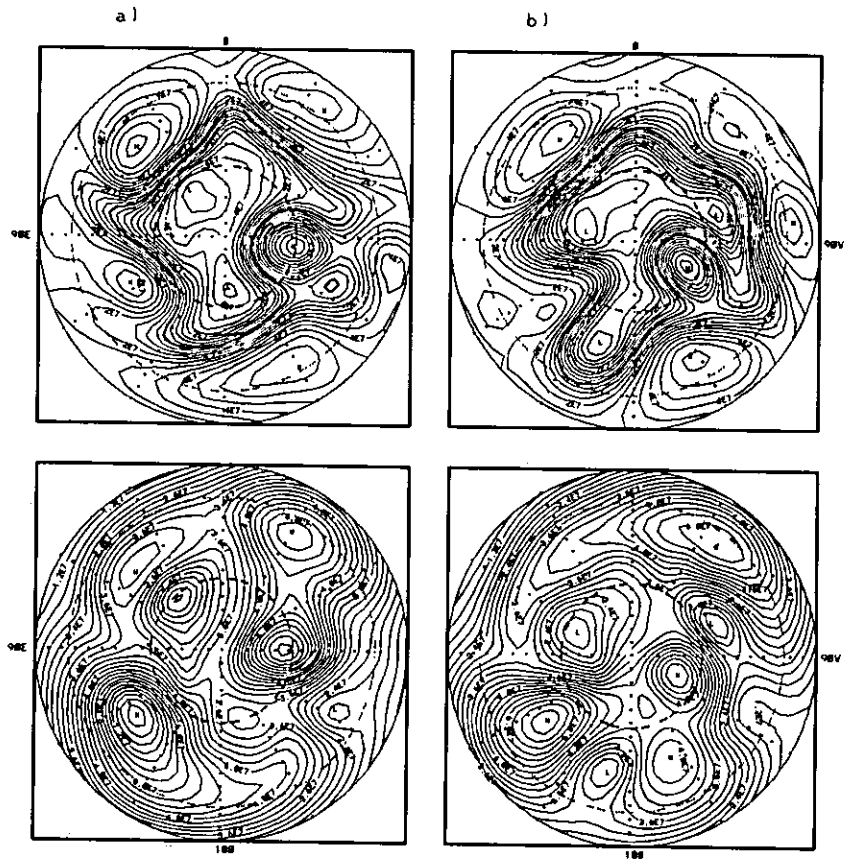

Figure 21: Continued (day 1900 (column a) and day 1903 (column b).

behind by the cutoff high PV-anomaly breaks and disappears in the following 24 hours. At day 1896, the upper-layer downstream trough, adjacent to the ridge, extends equatorward, has a slight backward tilt, and shows visible signs of thinning, very much as in the Simmons-Hoskins (1980) "basic baroclinic life cycle," termed LC1 by Thorncroft *et al.* (1994). The thinning results from cross-contour flow at the rear side of the trough and an almost perfectly contour-parallel flow at the leading edge. By day 1900 the trough is only umbilically connected to the mean jet, and 12 hours later (not shown) the breaking is completed, leaving behind the tip of a trough, clearly visible on day 1901. No block forms in this control run. Note that the structure observed in the upper-layer PV-maps in the subsequent days, in the vicinity of 60° W, 60° N, is not a block. Due to the scale effect (Hoskins *et al.* 1985), the streamfunctions associated with this PV-distribution (Fig. 23) are smoother and do not show any blocking-type splitting.

9.2 Sensitivity Analysis on *Block*1899

9.2.1 Sensitivity to the Normal Modes and Adjoint Modes of Day 1896

The relative sensitivity (RS) of the blocking index to the normal modes and adjoint modes of day 1896 was calculated at days 1898, 1899 and 1900. The results for day 1899, *i.e.*, for a time window of 3 days, were found to describe fairly well the relative impact of these structures on the response function on days 1898 through 1900. For this reason, only results pertaining day 1899 are shown. Table 4 shows the RS to the normal modes (for $|RS| > 0.1$), and Table 5 shows the RS to the adjoint modes (for $|RS| > 0.2$).

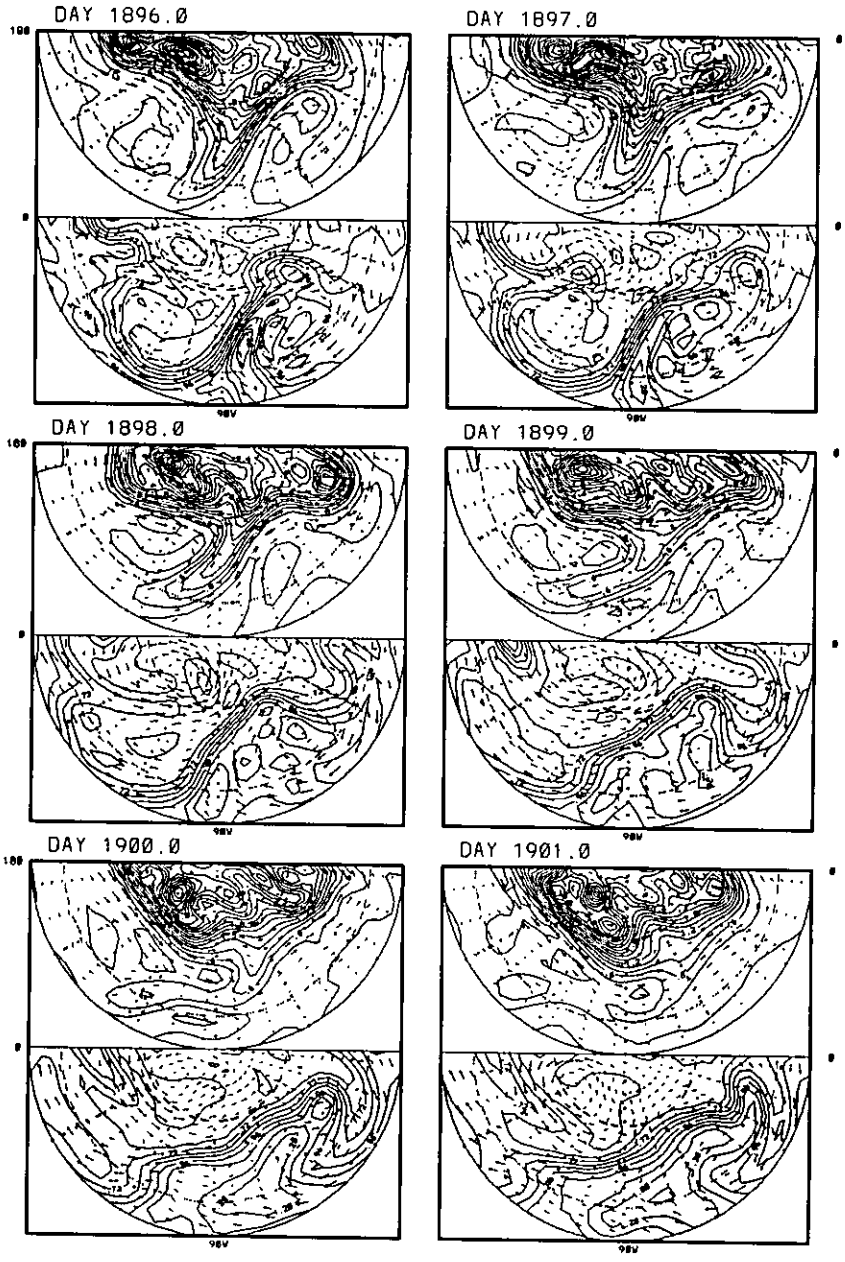

Figure 22: As in Fig. 10, except for the PV of the control run of *Block*1899. Sectors are for the semi-hemisphere 0° -90° W-180°. Fields have been rotated 90° to the west with respect to Fig. 9.

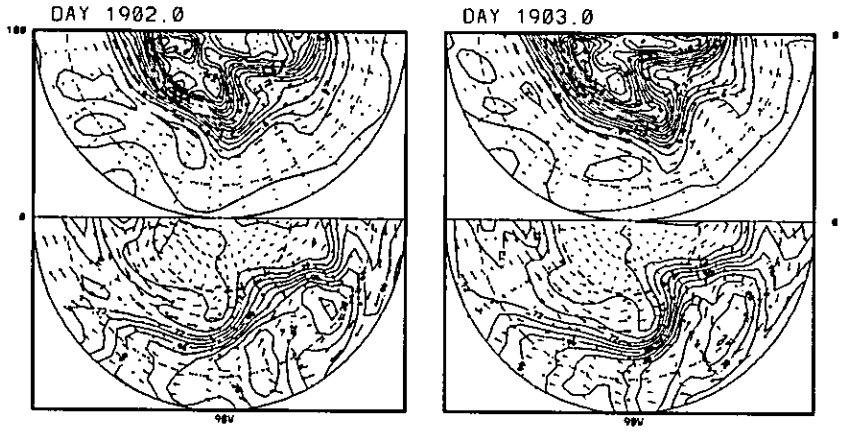

Figure 22: Continued.

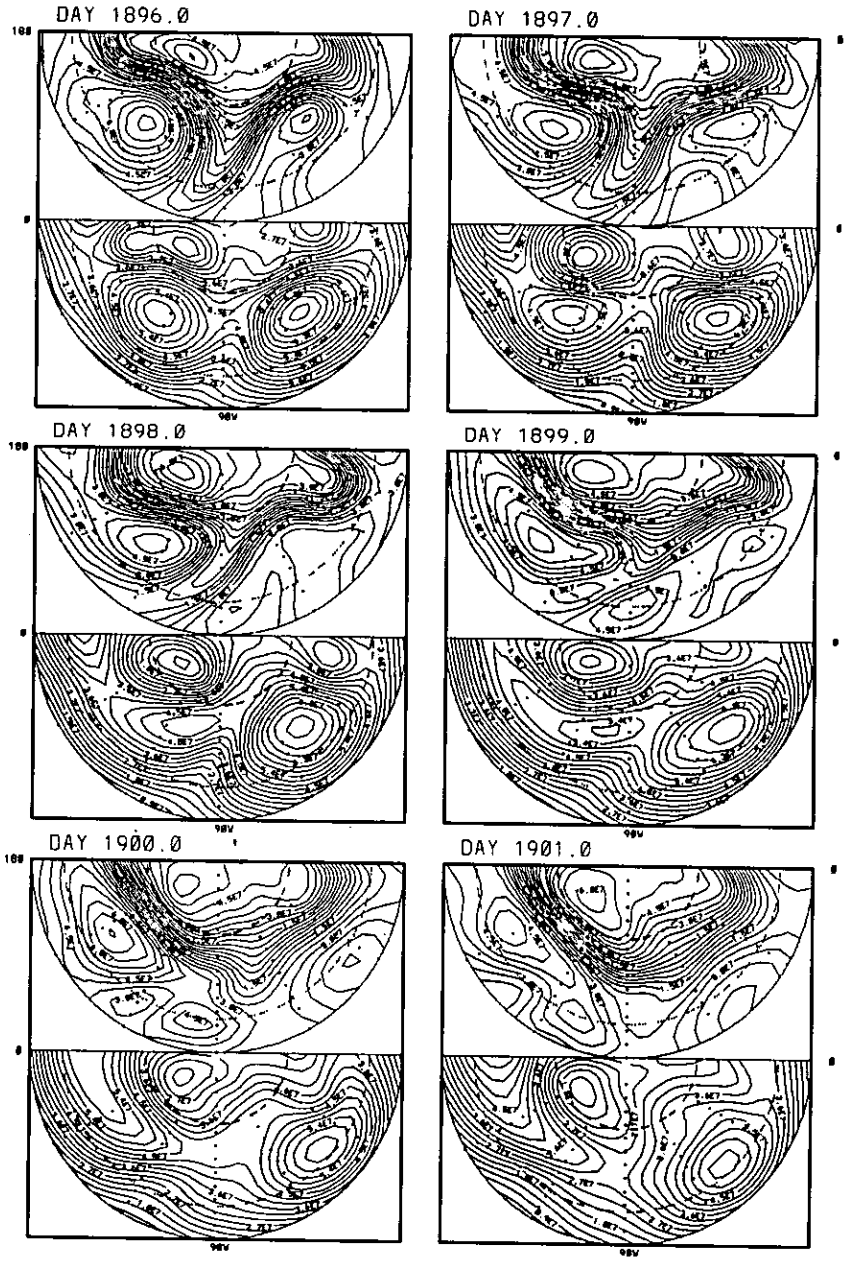

Figure 23: As in Fig. 22, except for the streamfunction. Contour interval as in Fig. 11.

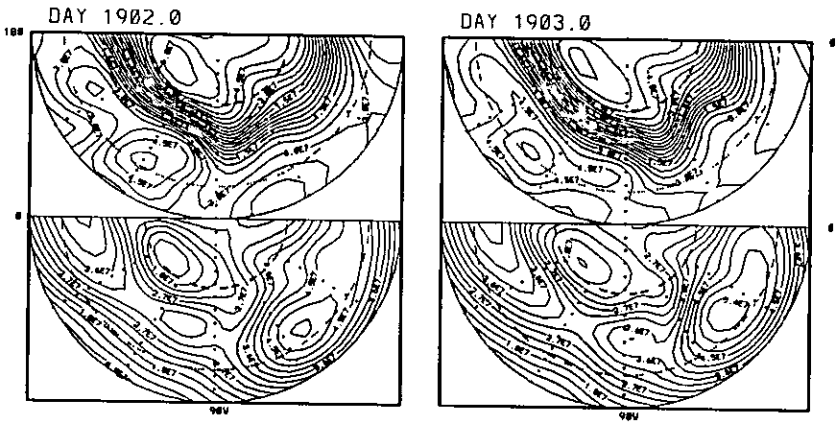

Figure 23: Continued.

A glance at the absolute values of the RS in both tables shows that the *blocking index is in general more sensitive to the adjoint modes than to the the normal modes.* A simple explanation for this fact is that since the adjoint mode can be obtained as the result of an optimization problem, namely, the problem of finding the best initial condition of unit amplitude which most effectively excites the normal mode, we then expect it to be associated with a faster growth than the normal mode. Equal growth occurs only when the projectability of the normal mode is one, implying that the normal mode and its adjoint

Table 4: As in Table 1, except for the RS to the normal modes of day 1896 calculated on day 1899. Only cases in which $|RS| > 0.1$ are shown.

Nmode	function	phase	Exp. coeff.	RS	γ
1	1	R	+18.56	+0.1186	3.71
4	8	I	+31.65	-0.1123	5.99
5	10	I	-6.14	-0.1033	5.48
6	11	R	+4.03	-0.1280	4.22
13	24	S	+23.43	+0.2554	1.73
69	135	R	+67.94	-0.1012	1.07
142	282	I	+12.41	-0.1455	4.03
315	624	R	+1.74	+0.1317	11.84
352	697	R	-19.40	-0.1044	15.22
606	1196	I	-0.16	+0.2034	6.52

Table 5: As in Table 4, except for the RS to the adjoint modes of day 1896 calculated on day 1899. Only cases in which $|RS| > 0.2$ are shown.

Nmode	function	phase	Exp. coeff.	RS	γ
1	1	R	-5.67	+0.3528	3.71
2	3	R	-6.61	-0.3033	6.56
3	6	I	+79.33	-0.4027	24.17
4	7	R	-20.93	+0.2244	5.99
5	9	R	+5.11	-0.3378	5.48
6	11	R	-5.72	+0.2964	4.22
7	13	R	-90.74	-0.3165	22.66
10	19	I	-1.95	-0.2651	5.60
12	22	R	-10.73	-0.2010	5.22
13	24	S	-1.02	-0.3561	1.73
15	28	I	-6.62	-0.2657	8.07
70	138	I	-18.86	-0.2417	3.33
104	205	R	+46.56	-0.2587	5.26
142	282	I	+18.53	-0.2608	4.03
153	304	I	-27.74	-0.2849	5.20
181	360	I	+1.40	+0.2295	3.17
350	694	I	+1.15	+0.2178	3.54
664	1308	I	+0.05	-0.6155	1.74

coincide. Assuming, on one hand, that the growth of some of the adjoint modes occurs in the right geographical regions of the onset of the block (as it will shortly be shown to be correct in an experiment with the first adjoint mode), and assuming, on the other hand, that the onset of the block can be explained as the result of the growth of perturbations superposed onto a "suitably averaged basic state," we then expect the adjoint modes to have a greater impact on the blocking index than the normal modes. A more subtle, but related justification, has to do with the connection between the adjoint modes and the singular vectors. This is discussed towards the end of Chapter 10.

Table 4 also shows that, as in *Block*1750, distant normal modes can have values of $|RS|$ larger than those of the leading modes. Fig. 24 shows the upper-layer streamfunction of the real and imaginary phases of the FGNM. This mode has a growth rate of 0.2920 day^{-1}, a period of 47.04 *days* and a projectability of 3.71. Its real phase, which is associated with an appreciable value of the RS, shows a well defined high-low dipole along meridian 120° W. At first, one would expect this mode to be able to excite a block. *Integrations of the model, with the model state at day 1896 perturbed with each one of the 10 structures of Table 4 were performed. Initial maximum perturbation winds ranged from* $2.5ms^{-1}$ *to* $10ms^{-1}$. *No transition to a blocked state was observed within a 6 day integration. In particular, the FGNM failed to excite a block.*

The structure of the adjoint modes reveals that they gain energy both barotropically and baroclinically, at least in the initial periods of development. As an example, we show in Figs. 25 and 26 the upper and lower-layer streamfunctions of the first and third adjoint modes, respectively. Both phases are represented. The third adjoint mode has a growth

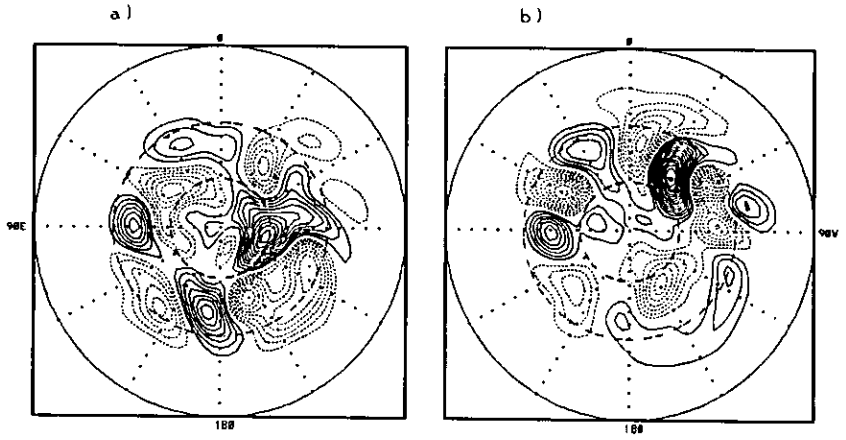

Figure 24: As in Fig. 13, except for the FGNM of day 1896. Only upper-layer shown. Contour interval $5 \times 10^5 m^2 s^{-1}$.

rate of 0.1031 day^{-1} and a period of 11.2 *days*. Both modes, besides showing a structure that varies from one layer to another, reveal, especially in the upper-layer, the "peanut banana-shape"-type structure, characteristic of barotropic growth.

As with the normal modes, we perturbed the state vector on day 1896 with some of the structures of Table 5, and integrated the model forward in time. It was found that some of the structures were able to excite a block, as described in the next subsection.

For later convenience, we show in this subsection selected normal modes and adjoint modes of days 1898 through 1900. Figs. 27 and 28 show the streamfunctions of the FGNM of days 1898 and 1899, respectively. The adjoint of the FGNM of day 1899 is shown in Fig. 29 and the FGNM of day 1900 in Fig. 30. These modes are discussed in Chapter 10.

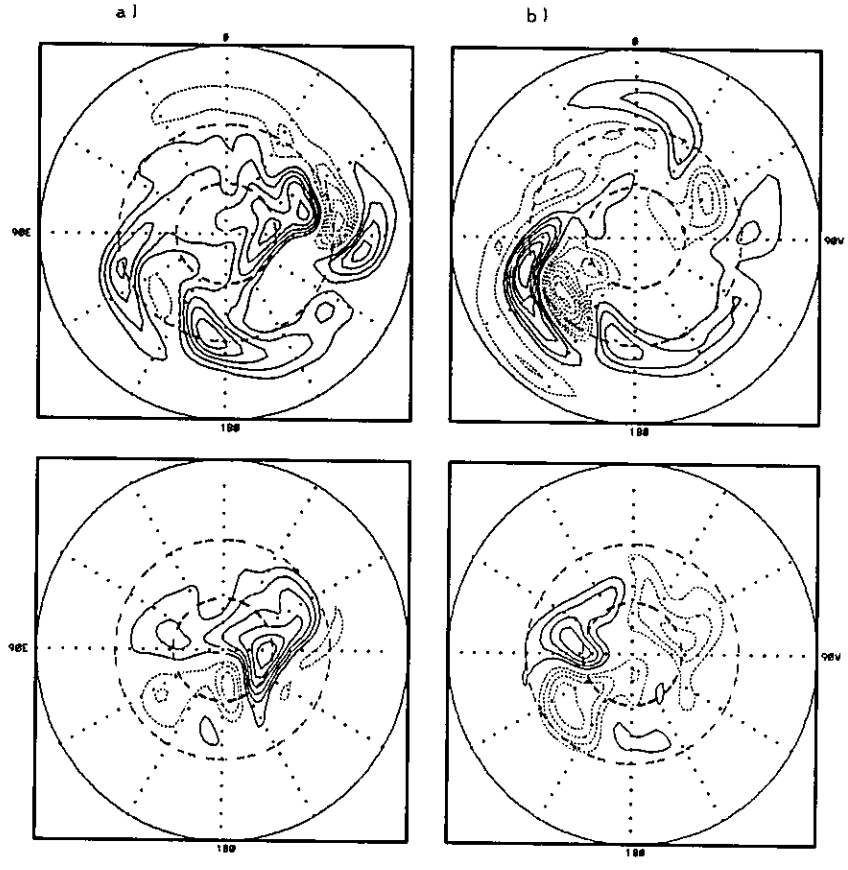

Figure 25: As in Fig. 13, except for the adjoint mode of the FGNM of day 1896. Contour interval $7.5 \times 10^5 m^2 s^{-1}$.

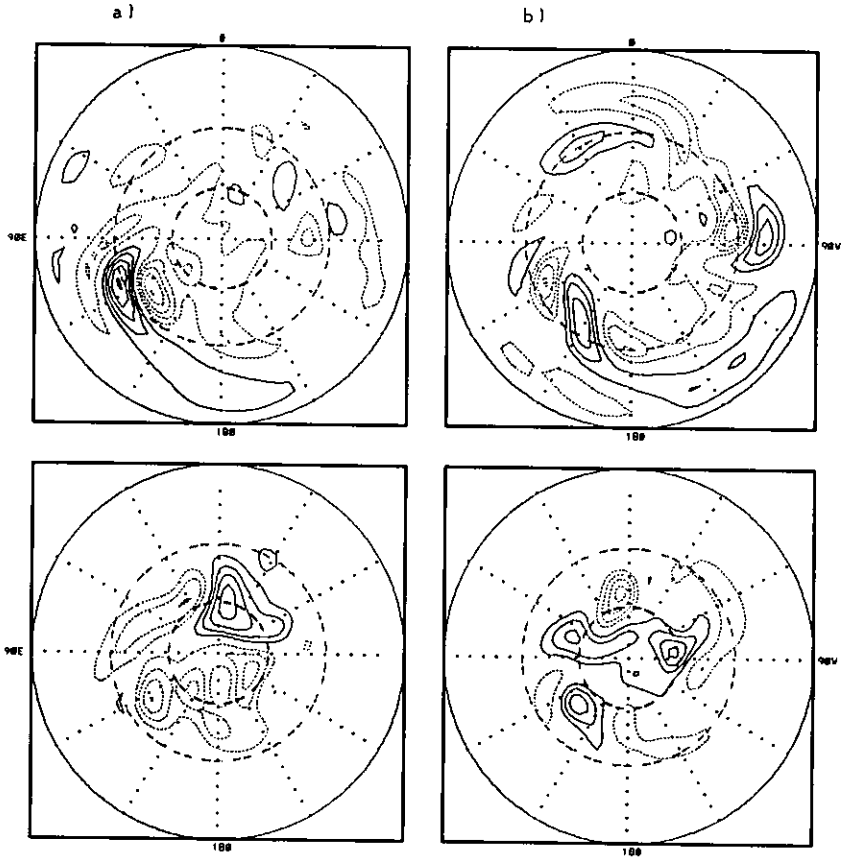

Figure 26: As in Fig. 13, except for the third adjoint mode of day 1896. Contour interval $7.5 \times 10^5 m^2 s^{-1}$ for lower-layer and $1 \times 10^6 m^2 s^{-1}$ for upper-layer.

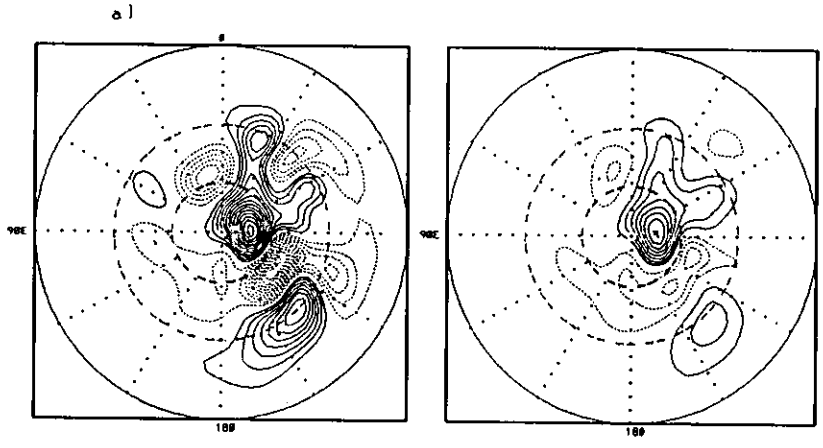

Figure 27: As in Fig. 13, except for the FGNM of day 1898. This mode is stationary. Left panel represents upper-layer and right panel displays lower-layer. Contour interval $5 \times 10^5 m^2 s^{-1}$.

9.2.2 Run Perturbed with the Real Phase of the First Adjoint Mode of day 1896

In this experiment, we perturbed the control run at day 1896 with the real phase of the first adjoint mode, normalized to have a maximum perturbation wind of $10 m\, s^{-1}$. The nonlinear model was integrated for 12 days. An initial perturbation with half the amplitude yielded comparable results.

The PV-maps of the total field (Fig. 31) show a reinforcement of the lower-layer PV-anomaly at 160° W, 50° N compared to the control run. In the upper-layer, a high PV-anomaly has been added to the region of the anticyclonically bending trough. The latter is less thin now than in the control run. As seen on the PV-maps of the disturbance at day 1896 or 1897 (Fig. 32), the upper-layer PV-anomaly is associated with a wind field that partially counteracts the cross-contour flow at the rear side of the trough, described in the control run. The disturbance behaves linearly and amplifies due to ordinary baroclinic

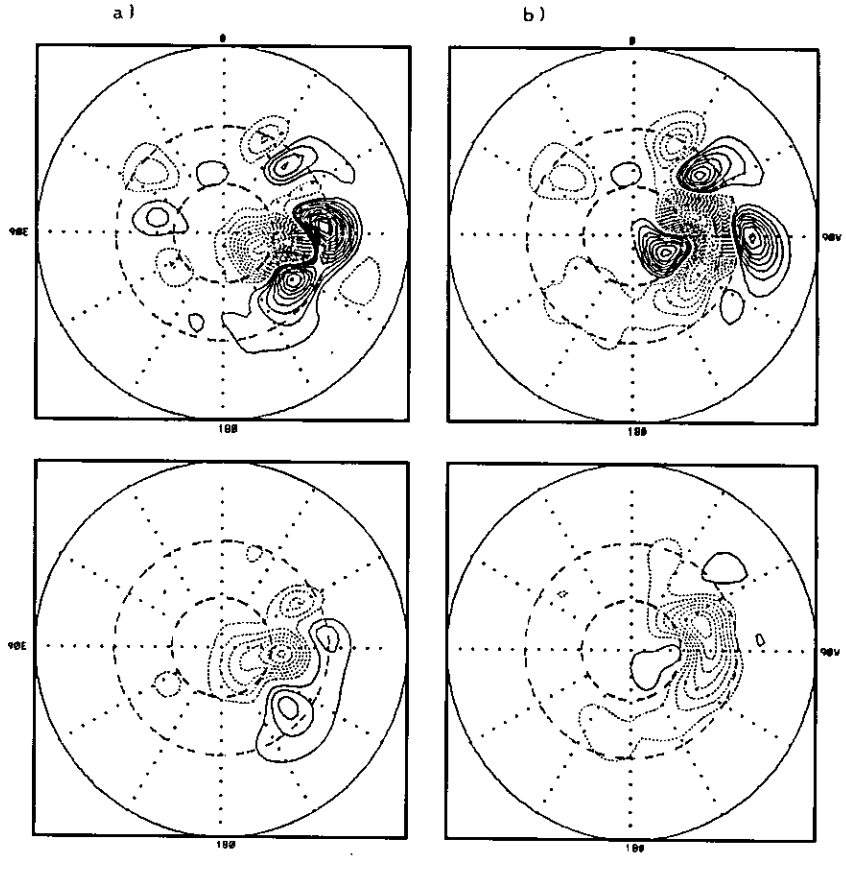

Figure 28: As in Fig. 13, except for the FGNM of day 1899. Contour interval $5 \times 10^5 m^2 s^{-1}$.

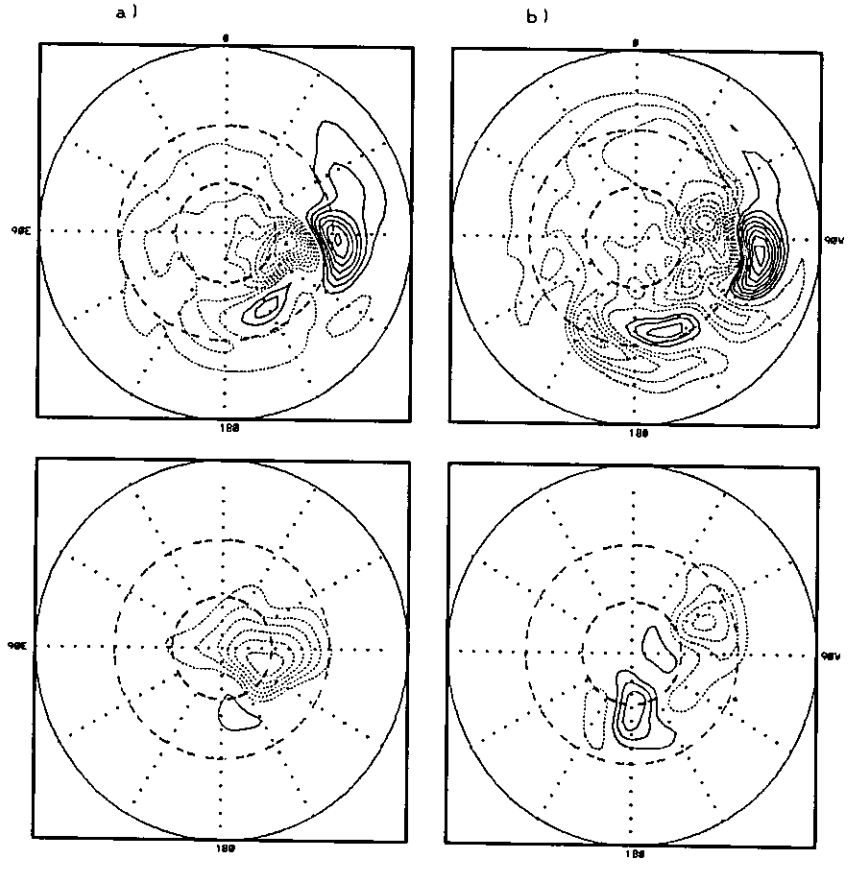

Figure 29: As in Fig. 28, except for the adjoint of the FGNM of day 1899. Contour interval $1 \times 10^6 m^2 s^{-1}$.

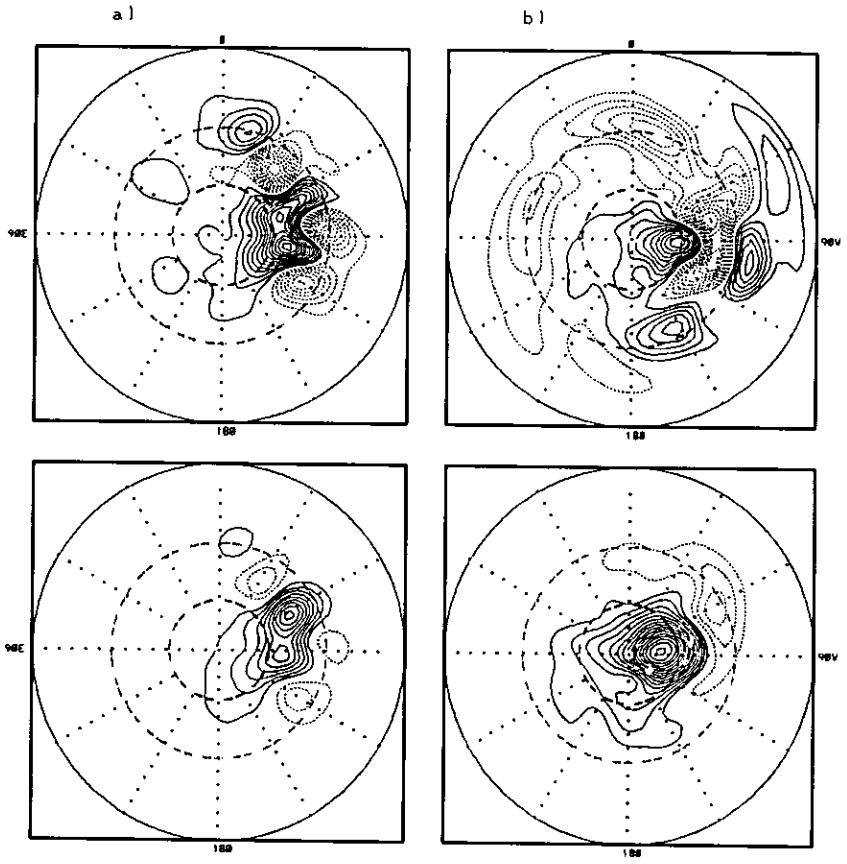

Figure 30: Left panels: streamfunction of the FGNM of day 1900. This mode is stationary. Right panels: streamfunction of the corresponding adjoint. Upper panels represent upper-layer and lower panels display lower-layer. Contour interval $5 \times 10^5 m^2 s^{-1}$.

and barotropic instability during the first 36 hours of integration. The linear behavior was checked by comparing the evolution with that on the linearized model with a time evolving reference trajectory. We see in Fig. 31 that, despite the shear induced by the perturbation in the upper-layer, a cross-contour flow is still present at the rear side of the trough, in its northernmost part. This causes a nearly cutoff upper layer cyclone by day 1898. Since the initial day of integration, both the control and the perturbed run show advection of low PV by the main jet towards the upper part of the trough, at 90° W. However, while in the control run this low PV fails to form a ridge, it forms a blocking dipole with the large cyclonic PV to the south in the perturbed run. The dipole intensifies *in situ* to a Rex-type of anomaly (*e.g.* streamfunction-maps of day 1900). This amplification of the upper-layer low PV-anomaly is accompanied by a lower layer advection of high PV beneath it. The lower-layer high PV resulted from the local growth of the perturbation. This growth causes the deformation of the PV-ribbon at 100° W, 45° N, as seen already on day 1898. Its form is that of a lower level frontal zone. Such deformation is absent in the control run.

It is interesting to note that during a later phase of the block, the upper-layer blocking cyclone is slightly advected downstream and decays, as seen on day 1904. At this time, a tip of high PV at 130° W, 50° N, steming from the polar regions, is present. It subsequently develops into a closed circulation of high PV as it wraps up cyclonically in the manner of a mixed LC1 and LC2-type development (Thorncroft *et al.* 1994, henceforth referred to as THM. The main features of the LC1 and LC2-type cycles are revisited in Chapter 10). The cyclonic wrap-up takes place with a southward displacement but without backward tilt or thinning. This high PV-anomaly intensifies and becomes favorably positioned for

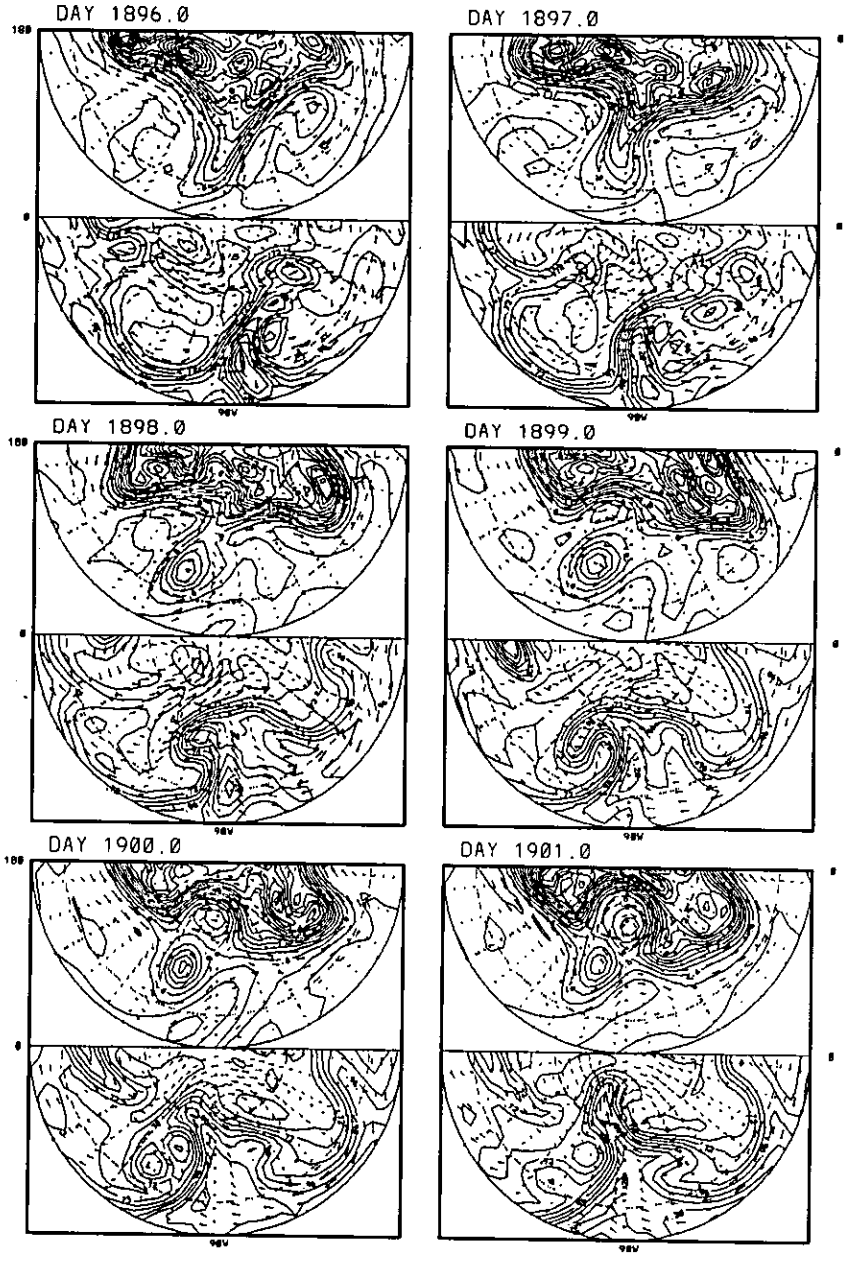

Figure 31: As in Fig. 22, except for the PV of the run perturbed with the real phase of the adjoint of the FGNM. Initial perturbation added to control run at day 1896. Initial maximum perturbation wind $10ms^{-1}$.

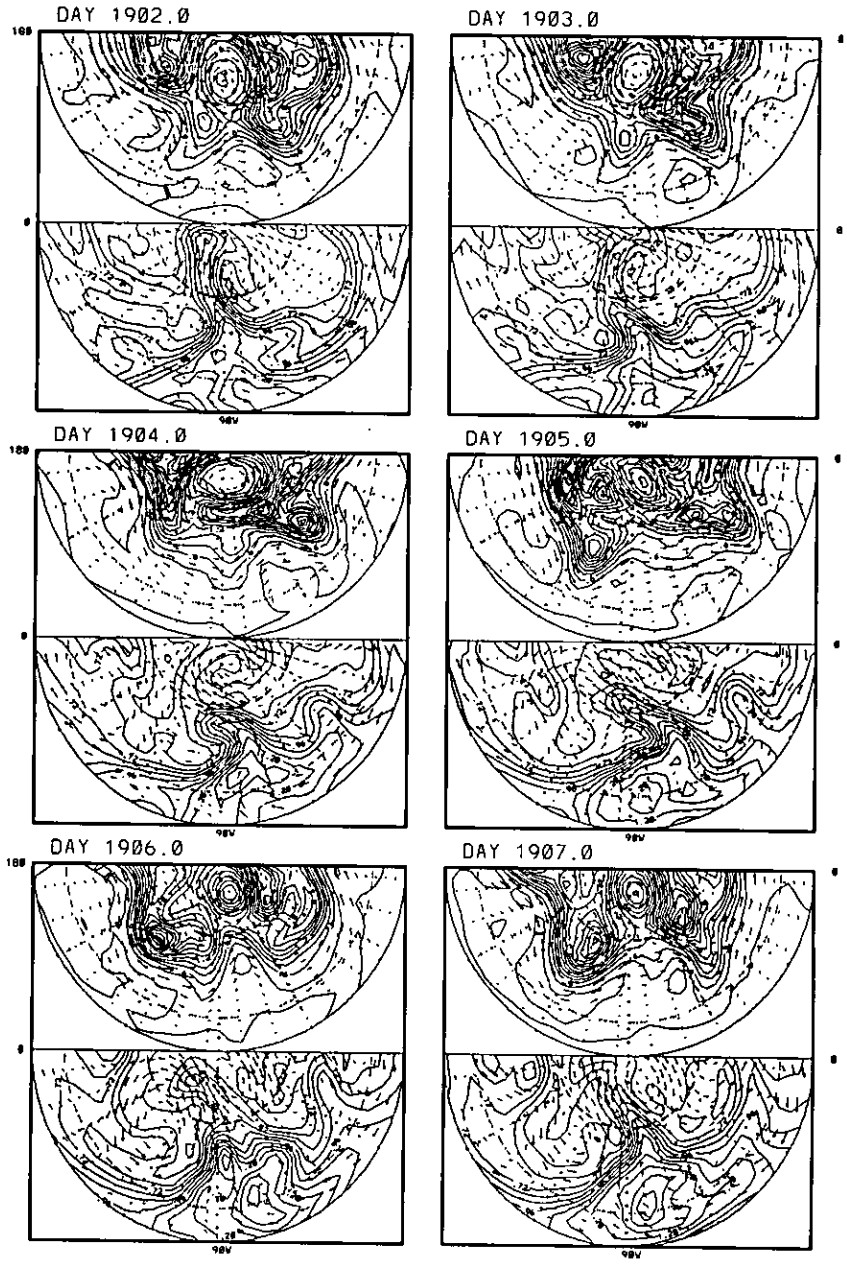

Figure 31: Continued.

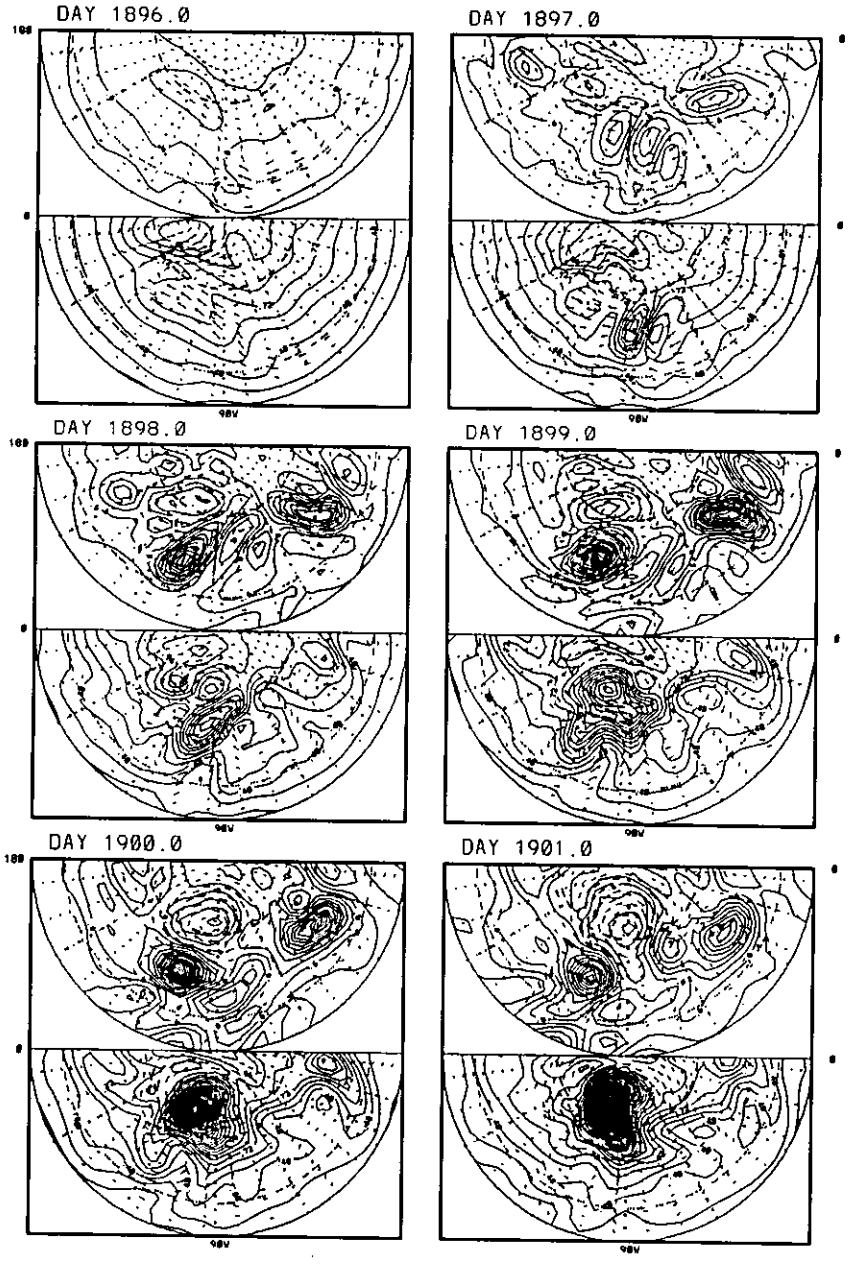

Figure 32: As in Fig. 31, except for the perturbation PV.

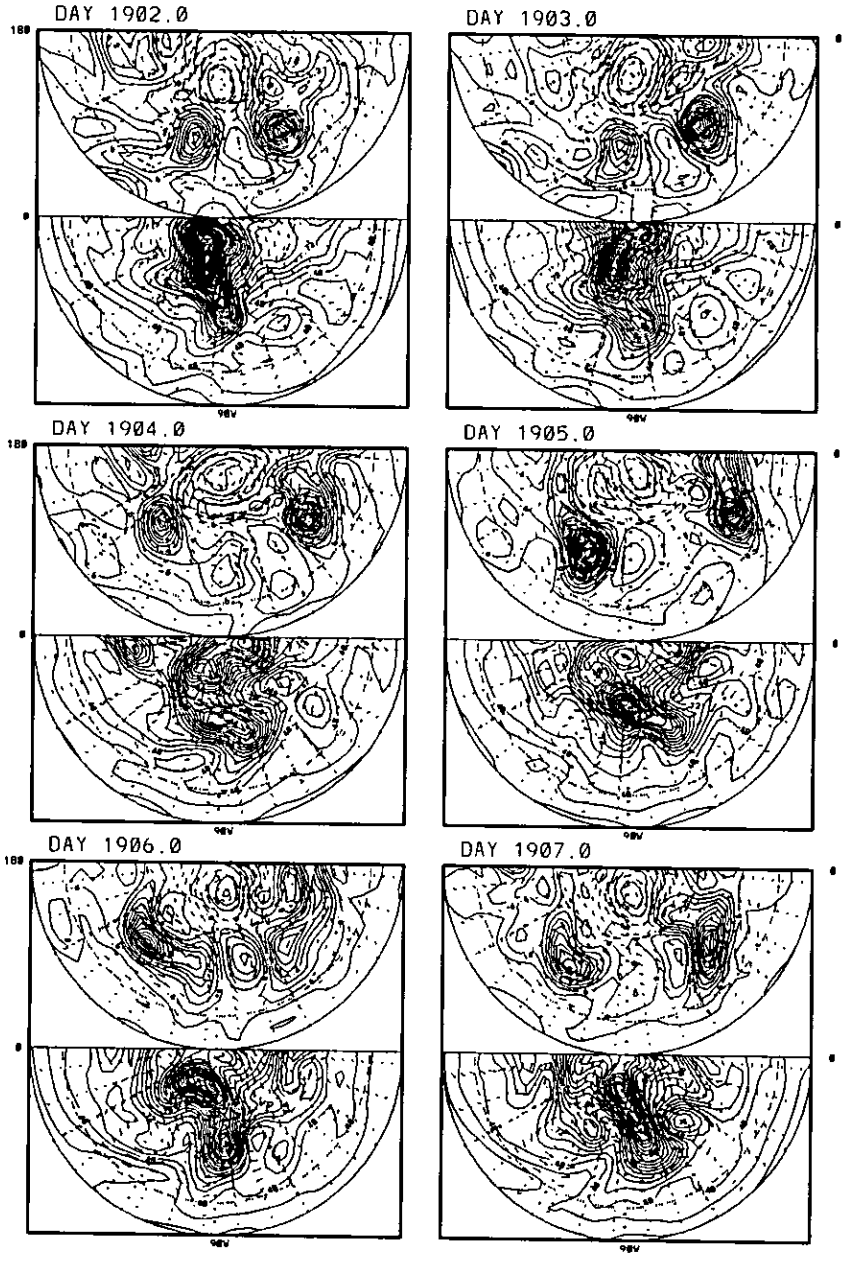

Figure 32: Continued.

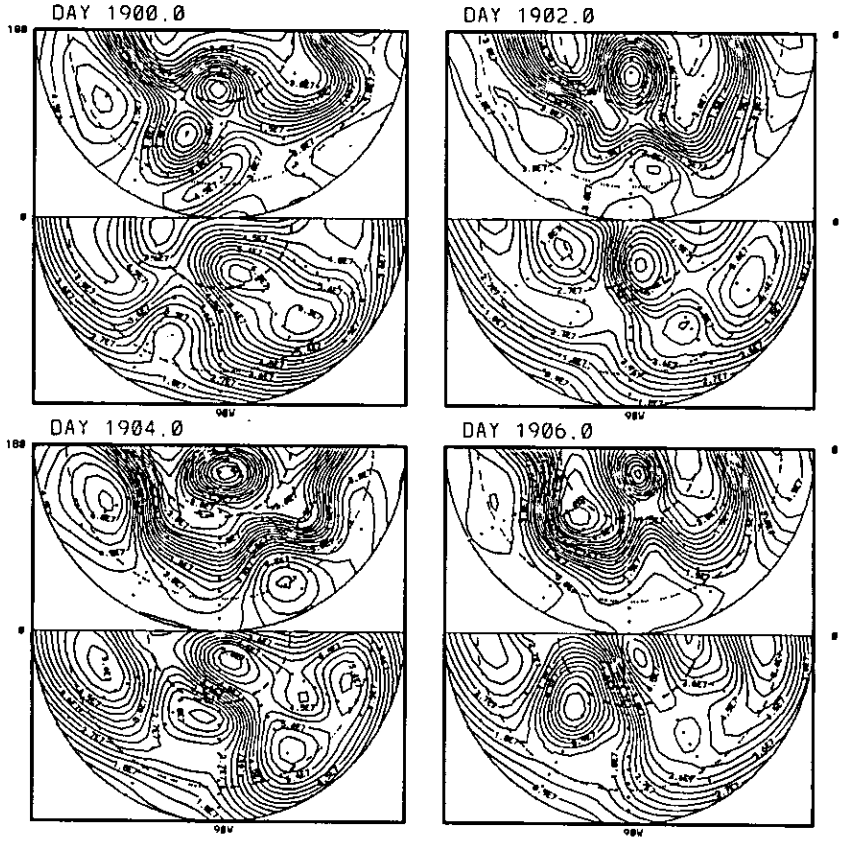

Figure 33: As in Fig. 23, except for the streamfunction of the run perturbed with the real phase of the adjoint of the FGNM.

its induced field to be advecting subtropical low PV to the location of the blocking ridge, thus maintaining the latter (*e.g.* global maps of PV of day 1907). The scenario seems to be that of subsynoptic scale high PV upstream of the blocking anticyclone being advected downstream by the large scale flow, and interacting with the lower layer baroclinic zone seen at 90° W, 60° N (day 1905). The further intensification of the high PV-anomaly could be interpreted as a finite amplitude baroclinic and barotropic growth. It results in a depletion of the lower layer baroclinic zone.

Although the perturbation grows linearly for the first 36 hours, *the entrance to the nonlinear regime is necessary for the onset of this block.* This was confirmed by performing integrations on the linearized model with time evolving basic state trajectory. No block formed in such experiments. Also, in light of the fact that other disturbances, in particular the FGNM, were unable to excite a block, we tentatively conclude that *the development is optimal during the linear part of the evolution.* These two ideas will be explored in more detail in the next subsections.

9.2.3 Optimal Growth: Sensitivity to Singular Vectors

We tested the idea of optimal linear growth by seeking perturbations that maximize the total perturbation energy in the semi-hemisphere 0°-90°W-180°after a time interval of 3 days.

Fig. 34 shows how the total perturbation energy in the semi-hemisphere 0°-90°W-180° evolves in time for the most explosive singular vector (SV), the real phase of the FGNM and the real phase of the adjoint of the FGNM. Integrations were performed on the

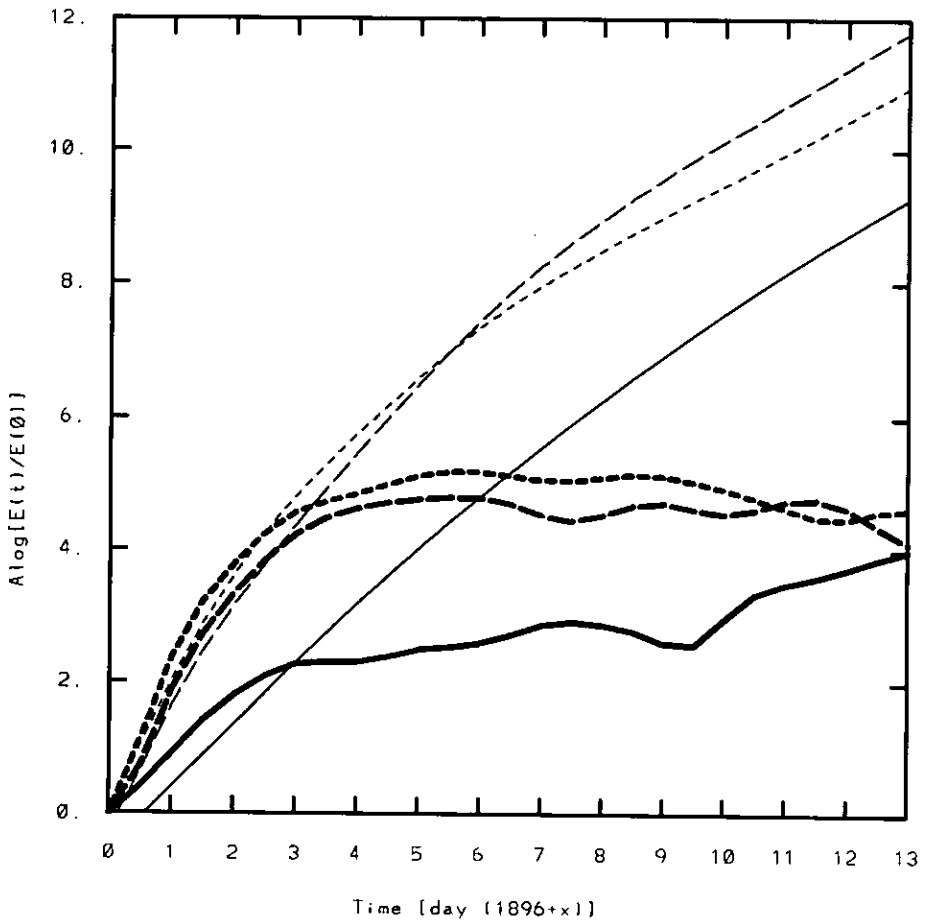

Figure 34: Time evolution of the total energy in the semi-hemisphere 0°-90°W-180°for the real phase of the FGNM (solid), for the first adjoint mode (long dashed) and for the first regional SV (short dashed). For each case, the plot represents the log_2 of the ratio of the total energy at a time t to the total energy at initial time. Light lines are for integrations on the T20-model with resting basic state, and dark lines for nonlinear integrations on the T31-model. In the nonlinear integrations the initial perturbations were normalized to have an initial regional total energy of $1m^2s^{-1}kg^{-2}$. This value corresponded to maximum perturbation winds in the range of $8ms^{-1}$ to $10ms^{-1}$.

Table 6: As in Table 4, except for the RS to the SV's of day 1896 calculated on day 1899. Note that no information regarding the phase is necessary for SV's. The sixth column (from left) contains the amplification factors of the SV's. Shown only cases in which $|RS| > 0.2$.

Nmode	function	Exp. coeff.	RS	γ	λ
1	122.34	+6.27	+0.4302	1.00	11.0610
2	54.37	+5.64	-0.3135	1.00	7.3738
3	39.99	+8.62	-0.3429	1.00	6.3234
4	32.17	-1.30	+0.2357	1.00	5.6719
5	22.34	+2.37	-0.4535	1.00	4.7263
8	12.06	-1.38	-0.2534	1.00	3.4723
18	2.65	-8.30	-0.2249	1.00	1.6272

T20-model, with resting basic state, and on the full nonlinear T31-model. In the nonlinear integrations, the initial perturbations were normalized to have an initial regional total energy of $1m^2s^{-1}kg^{-2}$. This value corresponded to maximum perturbation winds in the range of $8ms^{-1}$ to $10ms^{-1}$. *It is apparent in both the linear and nonlinear integrations that the most explosive SV produces the largest energy amplification over the optimization time (3 days).* The real phase of the FGNM is largely suboptimal. The real phase of the first adjoint mode grows almost as fast as the first SV. An explanation for this fact is given in Chapter 10. It is important to retain from Fig. 34 that the nonlinear integrations (with the initial perturbations normalized as above described) yield evolutions in energy, over a period of 3 days, which are very similar to those of the linear integrations.

Table 6 shows the relative sensitivity (RS) of the blocking index to the SV's of day 1896. The RS was calculated at day 1899. We see that *the absolute values of the relative sensitivity to the SV's are comparable to the absolute values of the relative sensitivity to the adjoint modes.* We note, however, that the largest changes are unequivocally produced by less than

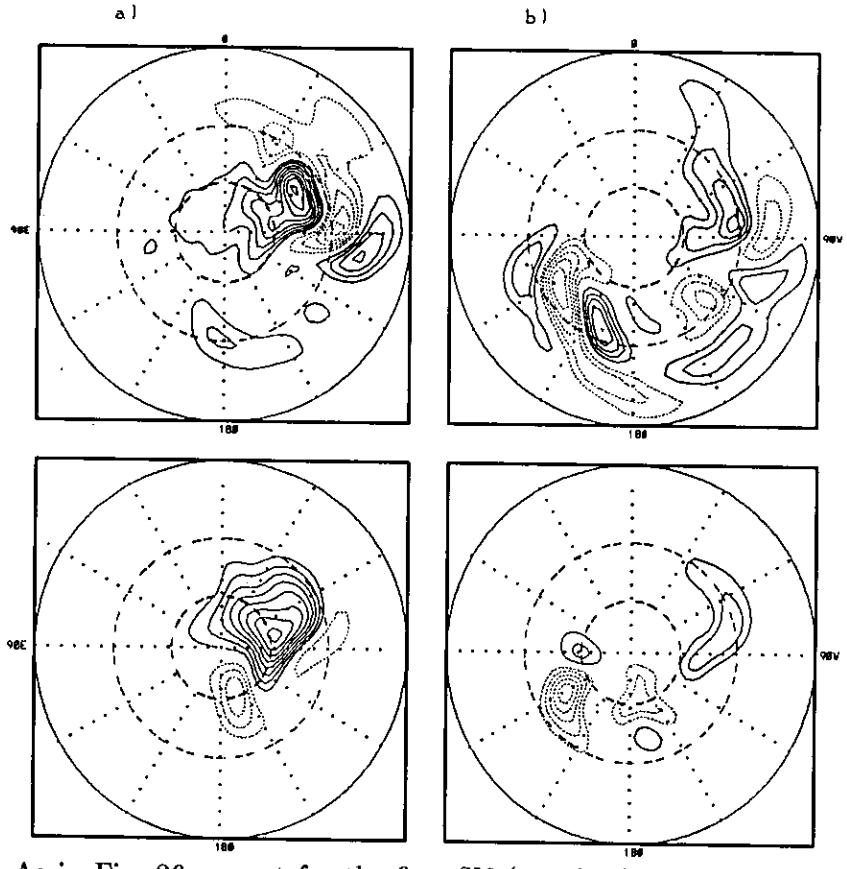

Figure 35: As in Fig. 26, except for the first SV (panels a) and the fourth SV (panel b). Contour interval $1 \times 10^6 m^2 s^{-1}$ for upper-layer and $7.5 \times 10^5 m^2 s^{-1}$ for lower-layer.

the first 20 SV's. We will come back to this point in Chapter 10. As with the adjoint modes, the SV's grow both barotropically and baroclinically in the initial moments of integration. As examples of their structures, we show in Fig. 35 the upper and lower-layer streamfunction of the first and fourth SV's. The amplification factor of the first SV is 11.0610 and that of the fourth SV is 5.6719. Notice how the most explosive SV resembles the real phase of the adjoint of the FGNM. The first SV was found to successfully induce a block.

9.2.4 Run Perturbed with the First SV

The initial perturbation was normalized to have a maximum perturbation wind of $10ms^{-1}$. The maps of the perturbation streamfunction (Fig. 36) show that the disturbance amplifies with very little phase propagation during the first 4 days. A very well defined barotropic high-low dipole is already present on day 1898, at longitude 110° W, north of 30° N. After day 1899, the anticyclone becomes more centered around 90° W, 60° N. The low, west of 90° W, connects to an already existing low cell upstream of the high, forming a zonally elongated low-structure that surrounds a perfect high to the north. In the semi-hemisphere 0°-90°W-180°, the perturbation grows until day 1902, and then starts to decay slowly . Barotropicity dominates the evolution of the perturbation after less than 24 hours of integration. The (barotropic) blocking dipole, persists throughout the integration even after day 1907 (not shown).

Fig. 37 shows the upper and lower-layer total streamfunction for the well established block at days 1901 and 1904. The PV-maps of the total field and of the perturbation reveal evolutions that are very similar to those described in section 9.2.2 for the run with the real phase of the first adjoint mode. For that reason they will not be shown. In particular, such maps reveal that during the buildup of the block, the lower-layer PV-ribbon is deformed and features a northward intrusion of high PV around 100° W, 60° N. In the upper layer, the perturbation counteracts the thinning and decay of the trough, and low PV again is advected downstream towards the location where the ridge will form. This low PV subsequently amplifies *in situ*.

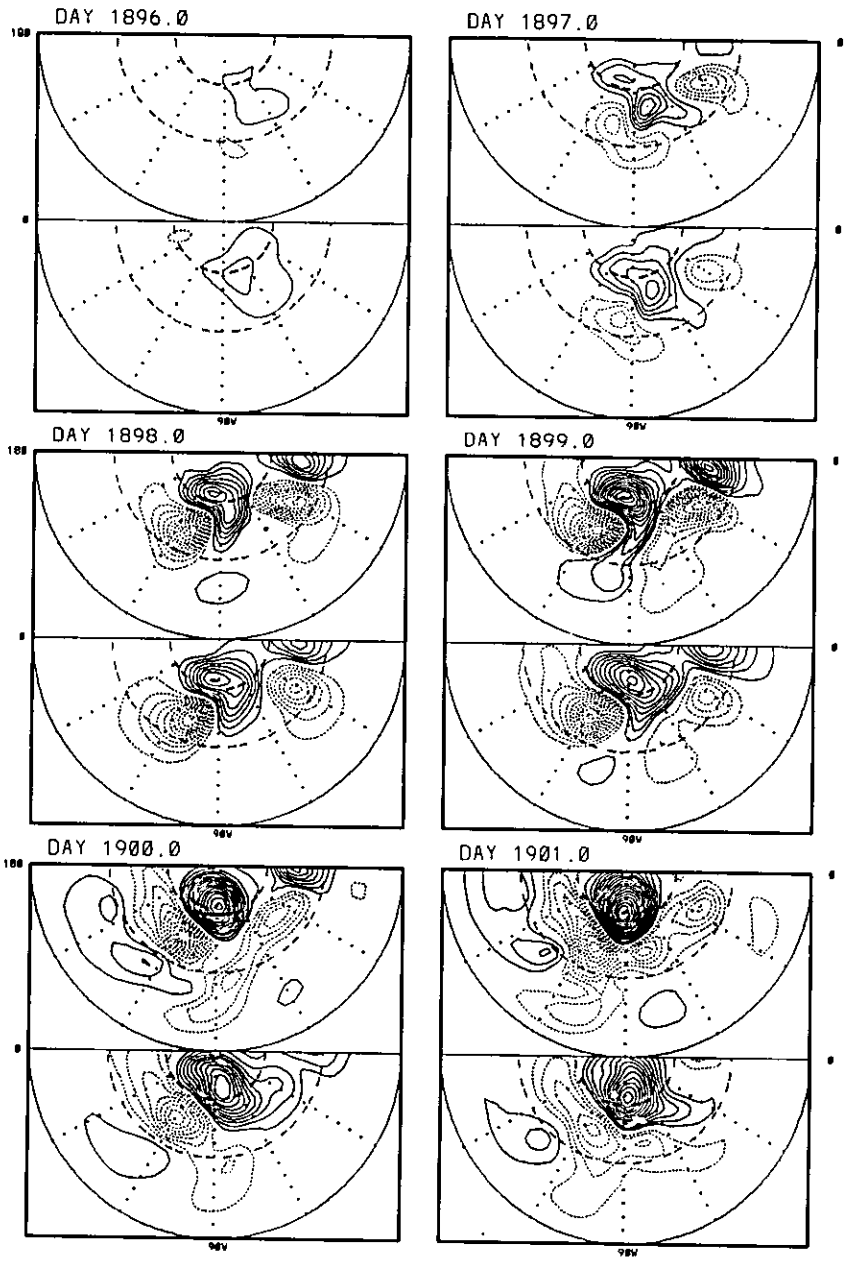

Figure 36: As in Fig. 32, except for the perturbation streamfunction. The perturbation is the first SV of day 1896. Boundary circle is the equator and inner circles are 30° N and 60° N.

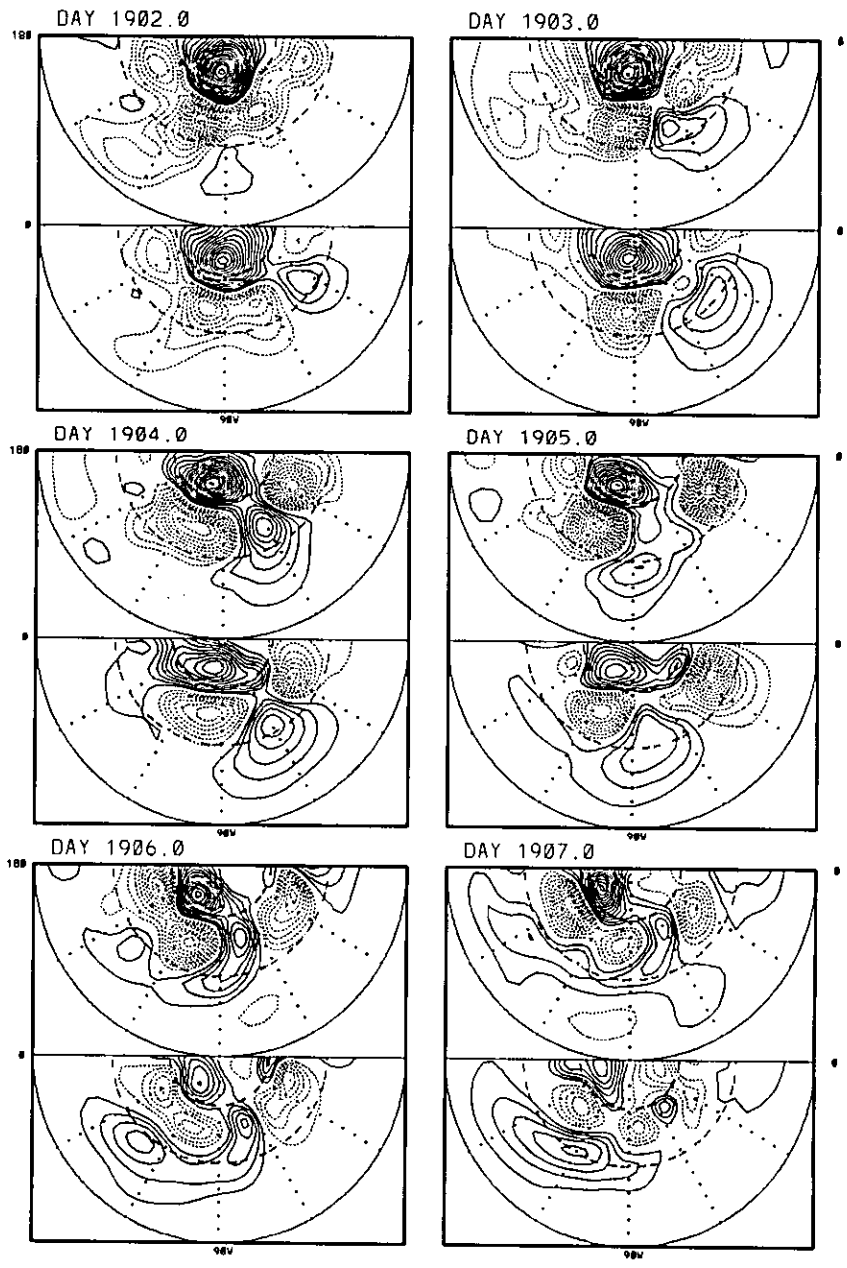

Figure 36: Continued.

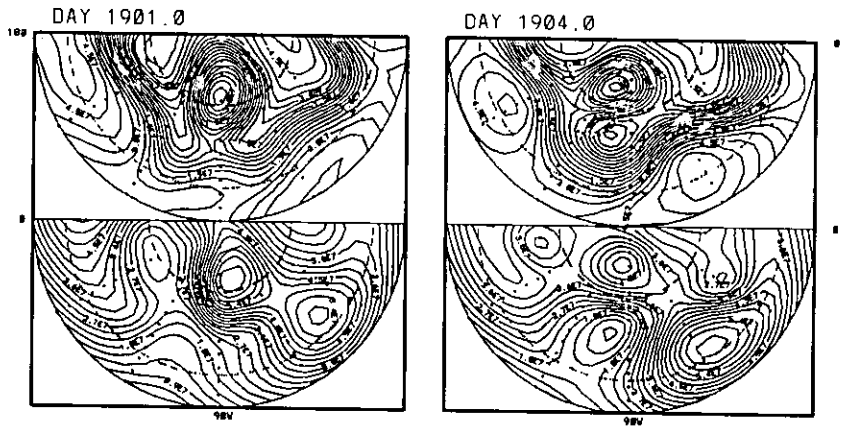

Figure 37: As in Fig. 33, except for the streamfunction of the run perturbed with the most explosive SV.

CHAPTER 10

Discussion of *Block*1750 and *Block*1899. Dynamical Framework

We referred in section 8.1 to two distinct phases of the buildup of *Block*1750. In the first phase, an equatorward extension of the two troughs accompanied by thinning, anticyclonic bending and eventual formation of two cutoff cyclones occurs in the upper-layer. In the lower-layer, we witness a poleward intrusion of the PV-ribbon beneath the location where the blocking ridge is to appear. The second phase is characterized by rapid intensification of the blocking ridge, accompanied by lower-layer advection of high PV beneath it.

The same two phases are observed on *Block*1899, whether it is excited with the first adjoint mode or with the first SV of day 1896. One difference that must be mentioned, however, is that only one upper-layer trough is observed on *Block*1899. It develops upstream of the location where the blocking ridge is to appear. In fact, these two phases were found in most of the blocks contained in the 2000 day control run with $\pi_\beta = 0.9$.

Thorncroft *et al.* (1994) (referred to as THM in this work) performed studies of two different baroclinic wave number 6 life cycles, named LC1 and LC2 (see also Simmons and Hoskins 1980). *The LC1 life cycle is characterized by thinning troughs that penetrate equatorward and bend anticyclonically, much as in the breaking of planetary-scale mid-stratospheric Rossby waves. The LC2 life cycle features forward-tilted, broadening troughs*

that wrap themselves cyclonically and poleward. In both life cycles, these main features occur in the nonlinear regime. In particular, it is argued by THM that the LC1 development can be interpreted in terms of a nonlinear critical-layer absorption, while the LC2 development represents a nonlinear critical layer reflection. These two extreme types of behavior were simulated on a multi-level model with zonal basic state flows, and the initial condition consisted of a 1 mb surface-pressure perturbation in both cases. In the LC2 cycle, however, a barotropic contribution was added to the basic state zonal wind, such that the *cyclonic* shear of the zonal-mean wind between 20°N and 50°N increased by about $6 \times 10^{-6} s^{-1}$. Fig. 38, taken from THM (their Fig. 12) shows schematically two examples of a high PV-contour (say PV=$2 \times 10^{-6} m^2 s^{-1} K kg^{-1}$) on a θ-surface indicating the two different cycles, as they might occur across the North Atlantic. The development starts with the advection of high PV air from polar regions. Near the east cost of North America, this air tends to tilt into the jet in a $NW - SE$ direction. Although the two life cycles start similarly, their nonlinear evolution produces remarkably different structures. The mean jet can be thought of as representing a barrier in the LC2 development. The cyclone wraps itself up under the influence of the strengthened ambient cyclonic shear in the northern portion of the jet. During this process, a trough broadening takes place, and a high PV cutoff can result in higher latitudes. In contrast, the mean jet shows absorption properties of nonlinear wave activity in the LC1 development. The PV-contours have an equatorward excursion and experience the ambient anticyclonic shear in the southern part of the jet. A thinning of the trough takes place during this development and can result in a cutoff high PV-anomaly in the subtropics. For more on the influence of lateral barotropic shear on

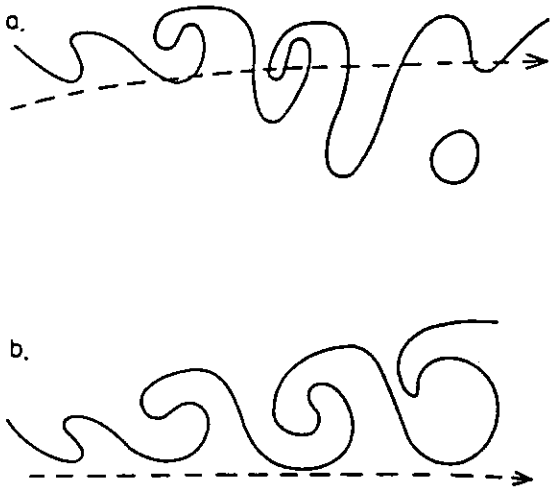

Figure 38: Schematic of a PV-theta contour in an Atlantic storm track sharing its main characteristics with (a) an LC1-type life cycle and (b) an LC2-type life cycle. The dashed line marks the approximate position of the mean jet at each stage (taken from THM).

the life cycle of growing cyclones the reader is referred to the work of Davies *et al.*, (1991). Note that the backward tilt of troughs, typical of an LC1-type cycle, follows from simple PV considerations on equatorward propagating Rossby waves. Also, as discussed in THM, the thinning (broadening) of troughs is a dynamically robust effect that can be explained completely by considering the superposition of the PV of a cyclonically (anticyclonically) sheared perturbation trough on the PV of the large scale wavy flow.

*It is apparent that the blocking cyclone, both on Block*1750 *and Block*1899, *originated from a LC1-type development in the total field.* Such development resulted in high PV cutoff (or near cutoff). In particular, *Block*1899 shows that a buildup is possible with just one of such LC1-developing troughs. The fact that the upper-layer trough decayed in the control run of *Block*1899, after an excessive thinning and anticyclonic bending, shows that

the lateral anticyclonic shear to the south of the jet must have the right magnitude in order for a blocking cyclone to form. The perturbation added to the control run (adjoint mode or SV) provided the necessary cyclonic shear to cancel the excess ambient anticyclonic shear.

A very interesting aspect is that the perturbation added to the control run (adjoint mode or SV) behaved itself in a way reminiscent of a a LC2-type development. This inference is supported by the plot of the perturbation kinetic energy in the semi-hemisphere 0°-90°W-180°as a function of the integration time. Fig. 39 corresponds to the experiment with the most explosive SV of day 1896. Integrations on the linearized model with a time evolving basic state show that the disturbance behaves linearly for the first 2 days in the semi-hemisphere 0°-90°W -180°. The kinetic energy, in the semi-hemisphere, increases until day 1899.5. It decreases slowly between days 1899.5 and 1900.5, and then almost levels off, reminiscent of the characteristic behavior of the kinetic energy in the LC2 development of THM (their Fig. 4). Also shown in Fig. 39 are the potential and total perturbation energy in the semi-hemisphere. The potential energy increases monotonically until day 1902, so that the total perturbation energy, although experiencing different rates of growth, also increases monotonically until day 1902. It then starts to decay. Further studies are required in order to understand the behavior of the potential energy during the onset. The perturbation energy in the whole hemisphere (total, kinetic and potential) is also shown for comparison. We see that the behavior is in general similar to that for the semi-hemisphere, but that the final decay of the total perturbation energy starts roughly 36 hours later, on day 1903.5, and that the potential energy increases faster after day 1898.5.

Fig. 40, taken from THM (their Fig. 4) shows the kinetic energy as a function of time

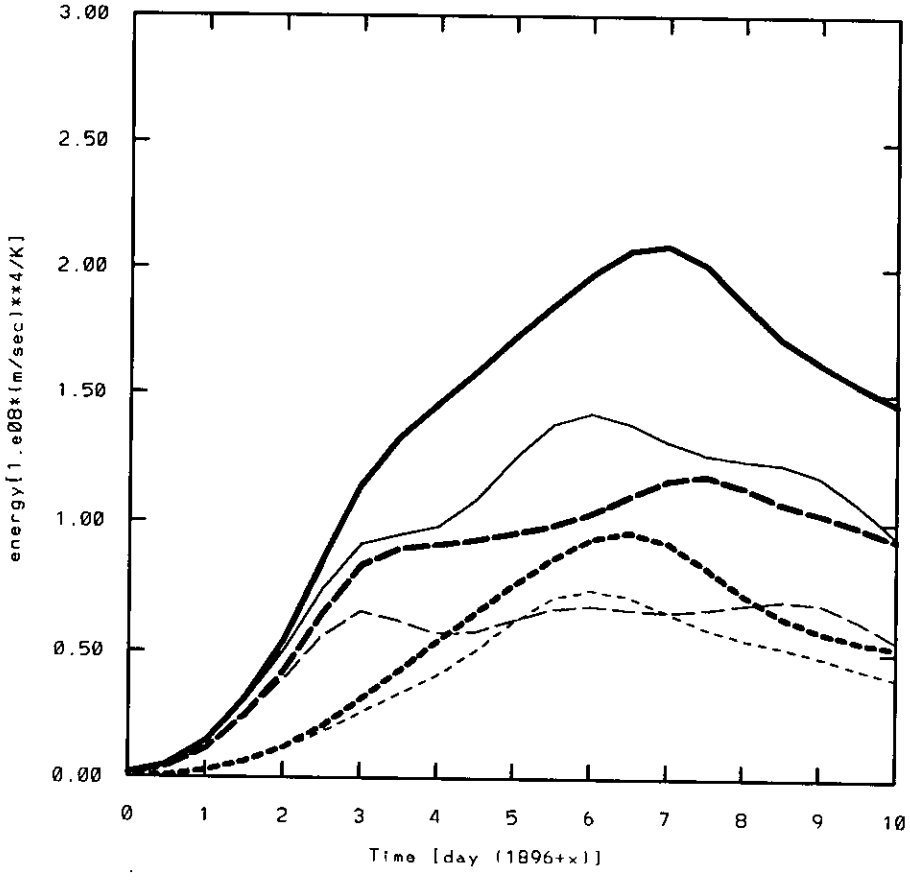

Figure 39: Time evolution of the perturbation kinetic energy (long dashed), potential energy (short dashed) and total energy (solid) in nonlinear integrations. The perturbation is the first SV, normalized at initial time to have a maximum wind of $10ms^{-1}$. Light lines are for the energies in the semi-hemisphere 0°-90°W-180°and dark lines for the hemispherical energies. In order to take into consideration the time evolving basic state Exner-layer thickness, $\Delta\overline{\pi}_{ok}$, we have used E' (formula (86) of page 160) instead of E (formula (87)).

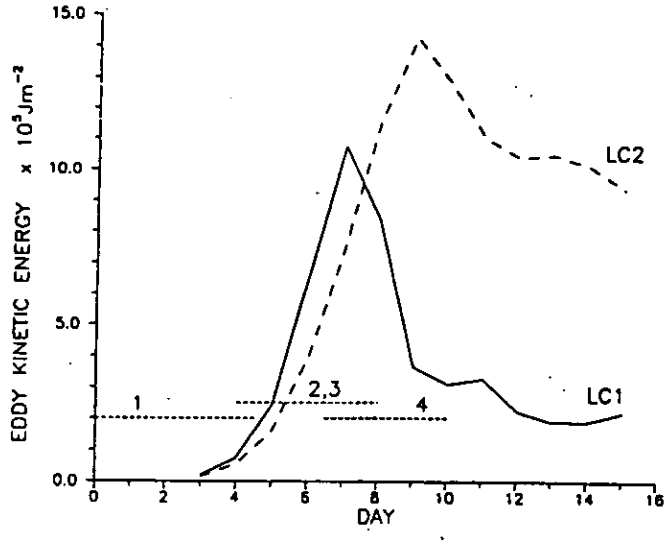

Figure 40: Eddy-kinetic energy evolution for LC1 (solid) and LC2 (dashed) (taken from THM).

for the LC1 and LC2 developments. The growth is linear in both cases, until about day 4, when nonlinear effects take over. As in our case, the kinetic energy continues to increase for some days. It then decreases rapidly in the LC1 development, reflecting the absorption of wave activity by the mean jet; in the LC2 development the kinetic energy levels off to a much higher value consistent with the existence of wave reflection by the mean jet. THM explain the growth in the nonlinear regime in terms of upward propagation of Rossby wave activity into the strongest mean westerlies. Whether or not the same picture is valid in our model is a question which needs further investigation, whereby the lack of vertical resolution in our model needs to be taken into consideration.

*We conclude that the first phase of the buildup of Block*1750 *and Block*1899 *features a LC1-cycle in the developing troughs seen in the total fields.* Also important to retain is that the anticyclonic shear to the south of the jet must have the right magnitude in order for

blocking cyclones to form at the end of the LC1-cycle.

Fig. 41 shows how the growth rate of the FGNM varies with time on *Block*1750 and *Block*1899. In both cases, it is seen that the flow becomes more unstable than usual, right after the process of trough thinning and formation of the blocking cyclone is concluded (day 1749 for *Block*1750 and day 1899 for *Block*1900). The relatively large growth rates achieved right after the first phase suggests that *the second phase consists of the excitation of one or more (leading) normal modes which reach high amplitudes by exponential growth.*

A reasonable working hypothesis that emerges from Frederiksen's theory of three dimensional instability for the onset-of-block, and from the meaning of the adjoint mode, as seen from the optimization perspective referred to in section 9.2.1, is that the first few growing modes calculated on the flow, around the day of the onset, might have adjoints which resemble the growing normal modes of the preceding days. In such a case, the onset of the block could, in a sense, be viewed as an optimized growth, whereby, the optimization time is theoretically infinity. Our calculations show that the FGNM's around the day of the onset have adjoint modes which very closely resemble the FGNM of the preceding day. Figs. 15 and 16 show the streamfunction of the first and second normal modes of day 1749, respectively. The FGNM has a growth rate of $0.3999\,day^{-1}$, a period of 16.38 days and a projectability of 6.65, while the second mode is stationary, has a growth rate of $0.2231\,day^{-1}$ and a projectability of 9.91. The streamfunction of the FGNM of day 1750 and of its adjoint is shown in Fig. 17. The FGNM is stationary, has a growth rate of $0.5633\,day^{-1}$ and a projectability of 2.47. We see that the adjoint contains a dipole approximately in the same

region where the FGNM of day 1749 (both phases) also show a dipole. The resemblance with the second normal mode of day 1749 is even closer. For *Block*1899, Fig. 27 shows the streamfunction of the FGNM of day 1898. This mode is stationary, has a growth rate of $0.5807\,day^{-1}$ and a projectability of 5.54. The streamfunctions of the FGNM of day 1899 and of its adjoint are shown in Figs. 28 and 29, respectively. This mode has a growth rate of $0.5944\,day^{-1}$, a period of 22.60 days and a projectability of 1.69. Both phases of the adjoint of the FGNM of day 1899 show dipole structures near the region of block formation. The same is true for the FGNM of the preceding day. The FGNM of day 1900 and its adjoint are shown in Fig.30. This mode is stationary, has a growth rate of $0.4370\,day^{-1}$ and a projectability of 28.03. We note how well its adjoint resembles both phases of the FGNM of the preceding day.

In fact, this empirical relationship was found to hold until 3 to 4 days back in time, before the onset. In other words, the FGNM of a day t_n was found to have an adjoint which resembled one of the leading normal modes of day t_{n-1}. However, due to the relatively large *e*-folding times of the normal modes calculated before the flow reaches a more than usual unstable configuration, it is very unlikely that the exponential modes will reach appreciable amplitudes. To substantiate our claim we note, for instance, that for *Block*1750 the FGNM of day 1747 has an *e*-folding time of 2.92 days, and for *Block*1899 the FGNM of day 1896 has an *e*-folding time of 4.43 days. When the instability reaches its peak, however, the *e*-folding times of the FGNM's are reduced to values close to 1.5 days. For example, it is 1.77 days for the FGNM of day 1750 and 1.68 days for the FGNM of day 1899. Values of the *e*-folding time of these magnitudes are consistent with the observations of Dole (1896),

concerning the rapidity with which anomalous centers develop right prior to the onset of the block. For this reason, *we suggest that the rapid intensification of the blocking ridge, which occurs right after the formation of the cutoff or near cutoff upper-layer cyclones, is originated by intense instability of normal mode form.* It is also interesting to note that the mechanism of initial growth can help in imparting amplitude to the leading normal modes, in this second phase of the buildup of the block. Notice, for instance, the large projectability (28.03) of the FGNM of day 1900.

It must be stressed that barotropic growth dominates in the exponential growth, as seen by the highly barotropic structure of all growing normal modes computed in this work. Baroclinic growth, most predominantly of non-exponential form, is however present in the model. The conceptual framework to understand structure development in this model is that of PV-thinking. In particular, the lower-layer, with its constant potential temperature and a structure in the PV, can be thought of as the result of substituting a baroclinic structure on a constant pressure surface by a thin layer of PV and a $\theta = constant$ surface (Bretherton, 1966). As mentioned in case studies 1 and 2, when the process of formation of the upper-layer blocking cyclones takes place, structures resembling low-level baroclinic zones are observed in the lower-layer PV. This suggests that baroclinic growth, although of non-exponential form, is present in this model. A more quantitative statement regarding the relative role of barotropic and baroclinic instability in this model has to involve writing the equation for the tendency of the total perturbation energy in terms of barotropic and baroclinic contributions, and evaluating these terms.

The sensitivity analysis performed on *Block*1899 also shows that normal modes and

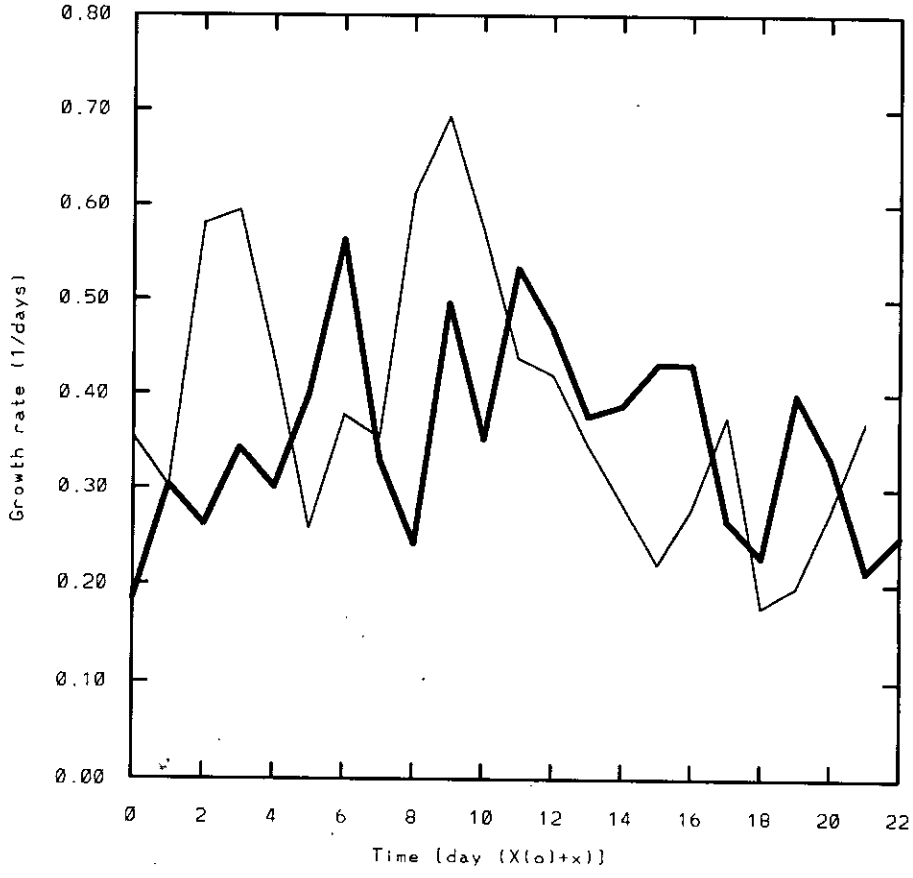

Figure 41: The growth rate of the FGNM as a function of time for *Block*1750 (dark line) and *Block*1899 (light line). The latter was excited with the first SV of day 1896. X(o) is day 1744 for *Block*1750 and day 1896 for *Block*1899.

adjoint modes distant in the spectrum can produce significant changes in the flow in the direction of phase space corresponding to a block. In some cases, these changes can be larger than those due to the leading modes. It is also true, however, that the first 15 or so adjoint modes represent a large portion of the adjoint modes that induce the largest changes in the response function. The reason for this will be discussed shortly.

The sensitivity analysis to the SV's shows clearly that the largest changes in the response function are produced by less than the first 20 SV's, and that the first 5 or so capture most of the largest changes. For *Block*1899, Fig. 42 represents a histogram of the percentage of total perturbation energy of the optimal-block-triggering-perturbation explained by each SV at the initial time (day 1896). The method of calculation follows immediately from equation (49). If $\mathbf{x}_o$, in equation (49), has a unit norm, then c_j^2 represents the fraction of norm explained by the j^{th} SV. Since the optimal-block-triggering perturbation was calculated with the same truncation in wavenumber space as that for the SV's, one does not need to be concerned about a residual term like $\Delta\mathbf{x}$, in equation (49).

We see that the most explosive SV's dominate the expansion. The combined first 5 SV's contain 34.11% of the variance, and the combined first 40 contain 46.57%. In the remaining SV's (1300 out of 1340), the individual maximum was found for the 1318^{th} SV. It amounts to only 1.24%.

This also helps us understand why the first 15 or so adjoint modes capture most of the largest changes in the response function. Theoretically, as discussed towards the end of section 5.2, an optimization time that approaches infinity must yield SV's that have an initial structure coincident with that of the adjoint modes. Clearly, in practice, what

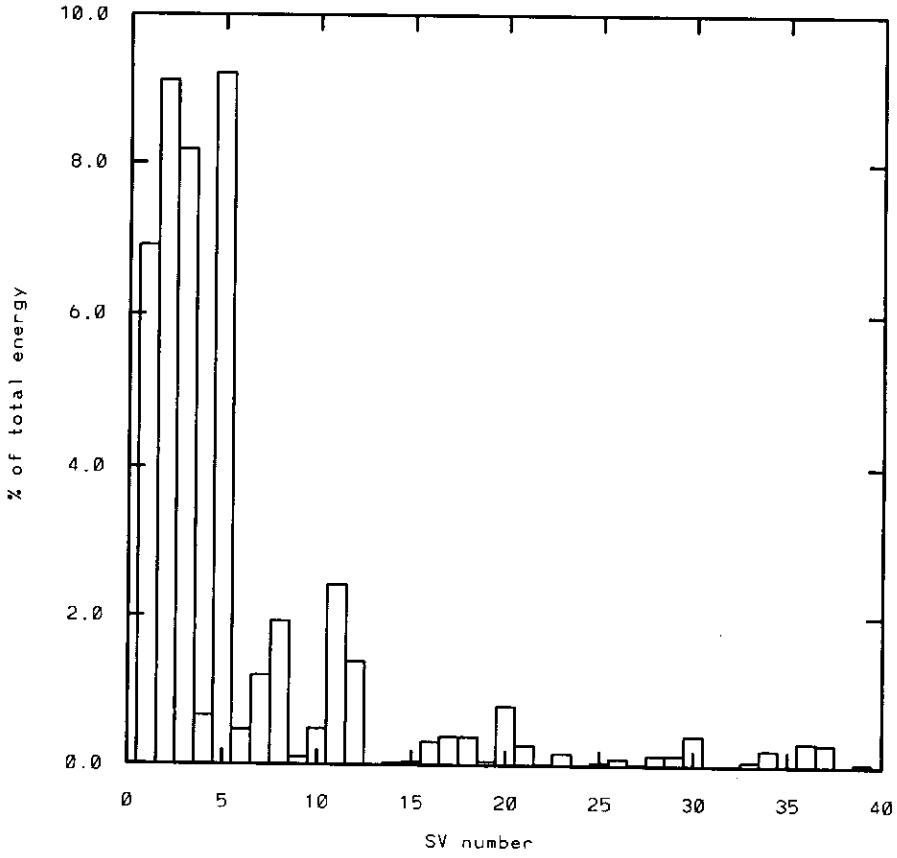

Figure 42: Percentage of the total perturbation energy of the optimal-block-triggering perturbation explained by each of the first 40 SV's of day 1896.

is to be understood by "infinite time interval" depends on the synoptic situation, on the perturbation, and on the particular model used. We found in our model with resting basic states that some of the growing normal modes could be excited in about 7 days, if the initial conditions were the respective adjoint modes, and that after 4 to 5 days of integration the structure of the normal modes was already recognizable. This time scale should be compared with the more than 25 days necessary to excite the FGNM if the initial perturbation is chosen through a random generator. The point is that for initial conditions which are adjoint modes, *an "infinite time interval" can mean 4 to 7 days*, so that the spatial variance of some of the leading adjoint modes should be captured fairly well by SV's optimized over 3 days.

From a practical point of view, this study shows that the use of the first most explosive SV's to construct a system of perturbations in ensemble forecasting is likely to capture important aspects of the dynamics associated with the transition to the blocked state. From a theoretical point of view, it shows that studies of the actual development of cyclones is necessary in order to understand the onset of some blocks.

CHAPTER 11

Initial Conditions 6 Days Before the Onset

The experiments described in sections 9.2.2 and 9.2.4 led to the onset of block some 3 days after the perturbations were added to the control run. It is both of theoretical and practical importance to go back in time and search for block triggering initial conditions some 6 days prior to the onset. For such periods of time, nonlinear effects are no longer negligible. Three different experiments were performed on *Block*1899:

1. It seemed natural at first to use a response function of the form (55) (see page 50), defined on day 1896. A "new mean pattern" had to be identified. We chose it to be the optimal-block-triggering-perturbation calculated at day 1896 (initial time), and optimized over 3 days (see Fig. 20). We then sought the best initial condition on day 1893 that at day 1896 had the largest projection onto the "new mean pattern." We hoped that such a perturbation, by virtue of having an optimized structure at day 1896, would produce a block on day 1899. The idea consisted of going back in time and performing a "step-wise" linear theory procedure. Such experiment did not succeed, however. This certainly shows that a non-linear optimization over a period of 6 days cannot be substituted by the two linear optimizations performed here. We believe that the failure is traced to the "new mean pattern" used, rather than to the idea of the "step-wise" linear theory. We suspect that because the "new mean pattern" is of sub-synoptic scale it cannot be used in the definition

of the response function. Indeed, there is a scale mismatch in the dot product between the daily-anomalies and the "new mean pattern." One should probably appeal to observational data and derive a "mean pattern" corresponding to the pre-blocking phase. Such phase is referred to by Colucci (1995) as the *"preconditioning phase of the large-scale waves."*

Since we realized that the optimization problem had been cast with deficiencies, there was no *a priori* reason to assume that SV's computed on day 1893 and optimized over 3 days would not produce a block around day 1899. Sensitivities to the regional SV's were computed, and integrations of the model were performed, using the SV's of largest sensitivities. No block was excited. Initial perturbation winds were varied to have maxima between $2.5ms^{-1}$ and $10ms^{-1}$.

2. The "mean blocking pattern" described in Chapter 7 was used in the response function defined at day 1896. The optimal-block-triggering-perturbation, optimized over 3 days, was then sought at day 1893. The idea was to bypass the scale inconsistency described above by maintaining the same "mean blocking pattern." Physically, we were hoping that if the perturbation was to possess the largest possible projection onto the "mean blocking pattern" already at day 1896, then, by "inertia, " it would inevitably induce a block at day 1899. However, this experiment was also unsuccessful.

Sensitivities of the blocking index to the regional SV's of day 1893, optimized over 3 days, were calculated. Integrations of the SV's associated with the largest sensitivities were again performed. No transition to the blocked state was observed.

3. We defined the response function at day 1899 (with the "mean blocking pattern" of Chapter 7), and calculated at day 1893 the optimal-block-triggering perturbation optimized

over a period of 6 days.

Such a perturbation was able to excite a block 6 days later, when the initial maximum perturbation winds were in the range of $7.5ms^{-1}$ to $10ms^{-1}$. Fig. 43 shows the PV of the total field at selected days. The initial perturbation had a maximum of $10ms^{-1}$ in the wind field. From day 1896 onwards, the process of block formation is very similar to that described in section 9 for the experiments with the first adjoint mode and first SV of day 1896.

Somewhat surprising, however, is that the regional SV's associated with the largest sensitivities of the response function were unable to trigger the transition to the blocked state. The optimization time was 6 days in this experiment. Also worth mentioning is that, in this case, some SV's distant in the spectrum were associated with leading values of the relative sensitivity.

The results in point 3 suggest that the optimal-block-triggering perturbation (linearly) optimized over 6 days probably captures most of the spatial variance of an analogous nonlinear optimal. The results also suggest, however, that the leading SV's optimized over such a long period have structures which do not relate well to the optimal-block-triggering-perturbation. The last claim is confirmed by the histogram of the percentage of initial energy of the optimal-block-triggering-perturbation explained by each SV (Fig. 44). Unlike the results shown in Fig. 42, where the first 5 SV's explained over 34% of the energy, in this case the first 5 SV's explain only 6.75% and the first 40 account for 27.51%. *From a practical point of view, this result shows that an adequate "nonlinear correction" to the SV's is necessary in ensemble forecasting, if these are to serve as possible onset of block precursors 6 days in*

advance. A crude first order correction worth investigating is the computation of the SV's on time varying basic state trajectories.

One could summarize the *main findings* of this case study and those of the previous as follows:

At least in some cases, the model shows that blocks can be excited from a zonal flow within a 3 day leadtime, if the linear sensitivity is large. This situation corresponds to the onset of the "less predictable blocks." It was found on *Block*1899 that the response function was generally more sensitive to adjoint modes and regional singular vectors (of days prior to block) than to normal modes. Also, the first five regional SV's were found to be associated with the largest values of the relative sensitivity, and to account for over 34% of integrated total energy contained in the optimal-block-triggering-perturbation at initial time. It was shown that, besides the optimal-block-triggering-perturbation, the real phase of the first adjoint mode and the first SV were also able to trigger the transition to the blocked state. No normal modes were however capable of triggering the transition. In particular, this confirms that among normal modes, adjoint vectors and singular vectors, the singular vectors are the most suitable perturbations to warn for the transition to block within 3 to 4 days in ensemble forecasting.

The onset of the blocks described in the two case studies performed here was found to consist of two main phases. The first phase featured a LC1-type development (Thorncroft *et al.*, 1994) in the total PV-field of the upper-layer. It resulted in the formation of upper-layer cutoff blocking cyclones. It was shown that the anticyclonic ambient shear on the equatorward side of the jet had to have the right magnitude in order for the blocking

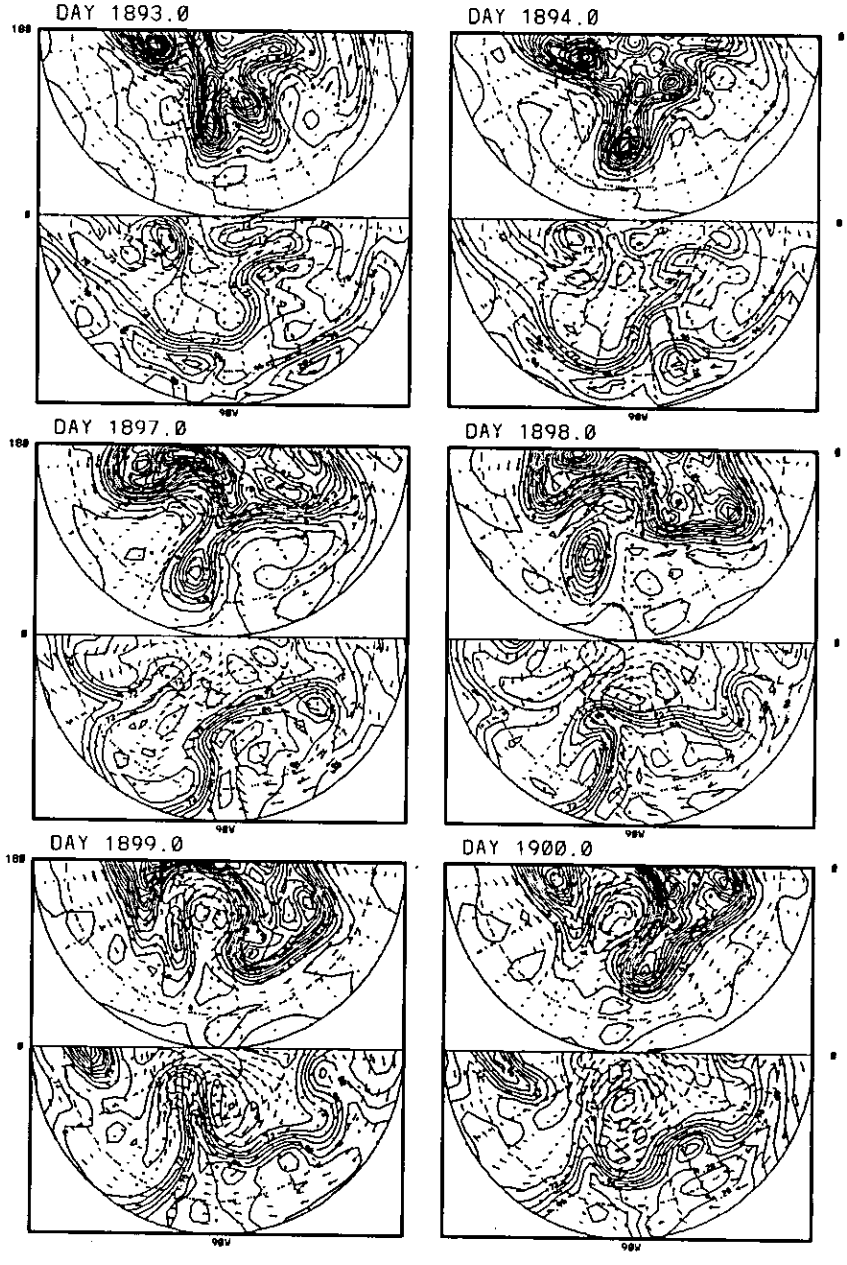

Figure 43: As in Fig. 31, except for the PV of the experiment with the optimal-block-triggering-perturbation calculated at day 1893, and optimized over 6 days.

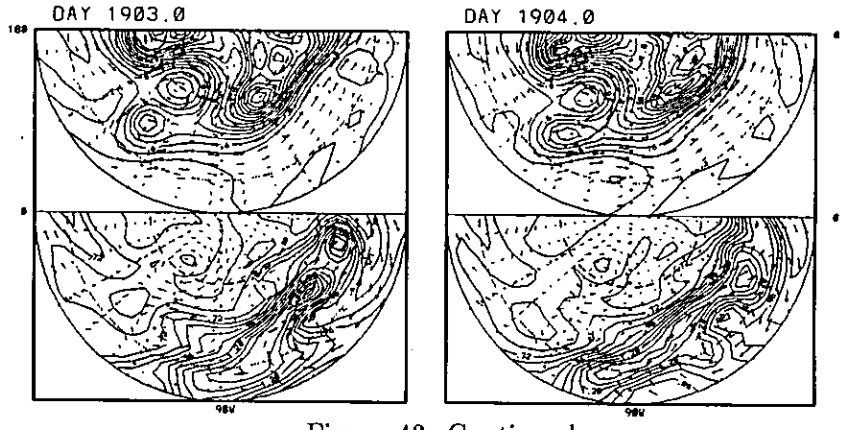

Figure 43: Continued.

cyclones to form. The second phase consisted of faster than normal exponential growth of the leading normal modes.

It was found that blocks were much harder to excite with initial conditions 6 days prior to the onset, a situation which corresponds to the experience of forecast centers. A "step-wise" linear theory, based on the idea of studying the evolution of perturbations over a period of 6 days as consisting of the evolution over two consecutive periods of three days, did not succeed. A more adequate definition of a pre-blocking state is necessary. The results also show that regional SV's optimized over 6 days are inadequate to predict the transition to the block. A proper consideration of nonlinearities in an "improved optimization procedure" seems necessary.

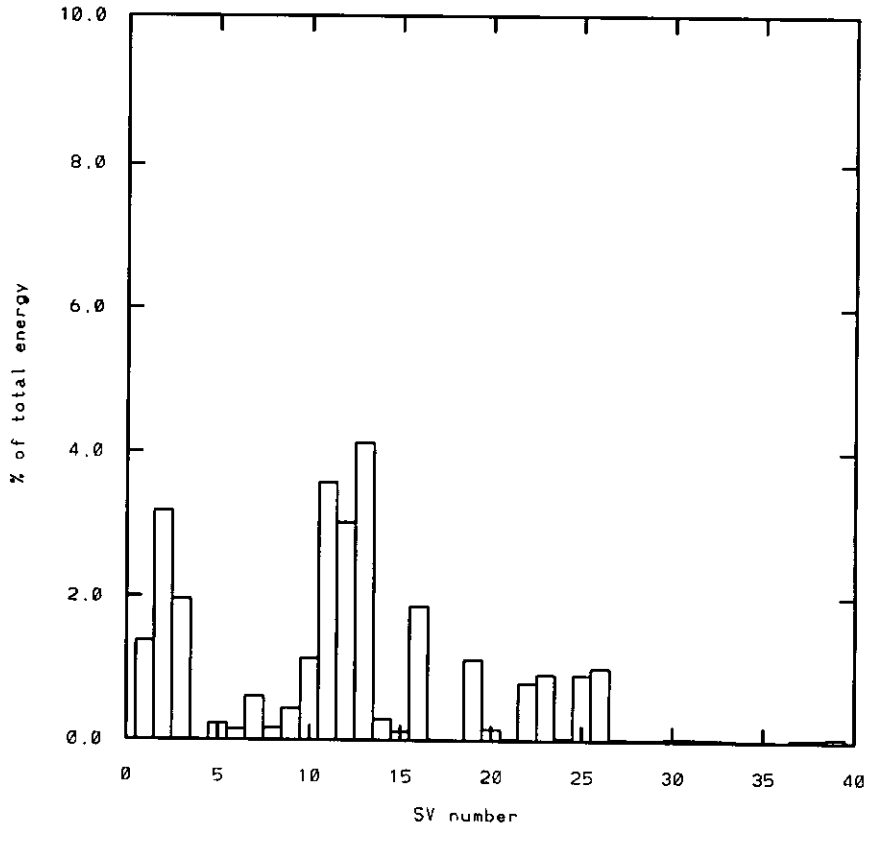

Figure 44: As in Fig. 42, except for the optimal-block-triggering-perturbation and SV's calculated on day 1893, and optimized over 6 days.

CHAPTER 12

Block with $\pi_\beta = 0.7$

As mentioned in Chapter 2, the parameter π_β controls the north-south slope of the interface equilibrium Exner function, and therefore the baroclinicity in the model. This parameter seems to also control the process by which blocks form in this model. We selected a block from the model control run with $\pi_\beta = 0.7$ to contrast with the blocks of case studies 1 and 2. The onset takes place at around day 394. We briefly describe in this Chapter the sequence of events that lead to the onset. Figs. 45 and 46 show the PV and streamfunction maps between days 390 and 395.

As seen in the upper-layer PV maps, there is no formation of cutoff of near cutoff cyclones in this case. The two steps of block formation encountered in case studies 1 and 2 seem to be absent in the present block. Rather, the upper-layer blocking ridge forms in a smooth way, apparently due to persistent advection of low PV from the southernmost part of the jet, at approximately 50°E, towards 90°E. This is already seen on day 390. Throughout the development of the upper-layer blocking ridge, we witness the advection of high PV beneath it, in the lower-layer. By day 394 a well defined blocking pattern has already formed. The streamfunction maps show a well developed upper-layer blocking ridge at around 90°E, 60°N. The block persists until roughly day 404 (not shown). It is interesting to note that the downstream upper-layer trough experiences a backward tilt (*e.g.* PV maps

of days 392 through 394), but that a thinning (characteristic of a LC1-type cycle) starts only after the onset has taken place (*e.g.* PV maps of day 395).

From the above sequence of events, we strongly suspect that this block forms through mechanisms that are different from those that led to the blocks of case studies 1 and 2. In the same way as the blocks of case studies 1 and 2 were found to be representative of the majority of the blocks obtained with $\pi_\beta = 0.9$, the sequence of events just described were found in most of the blocks with $\pi_\beta = 0.7$.

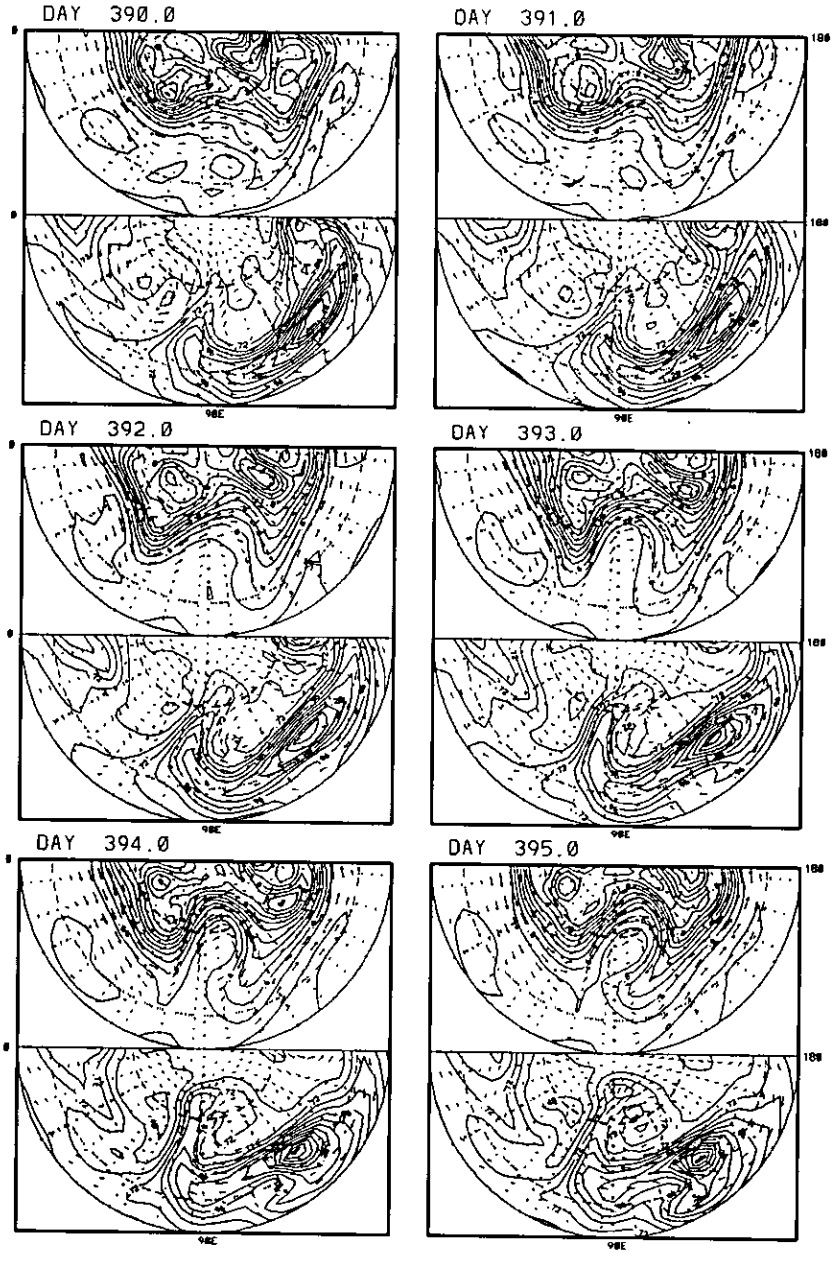

Figure 45: As in Fig. 10, except for the PV of a blocking episode that occurs with $\pi_\beta = 0.7$.

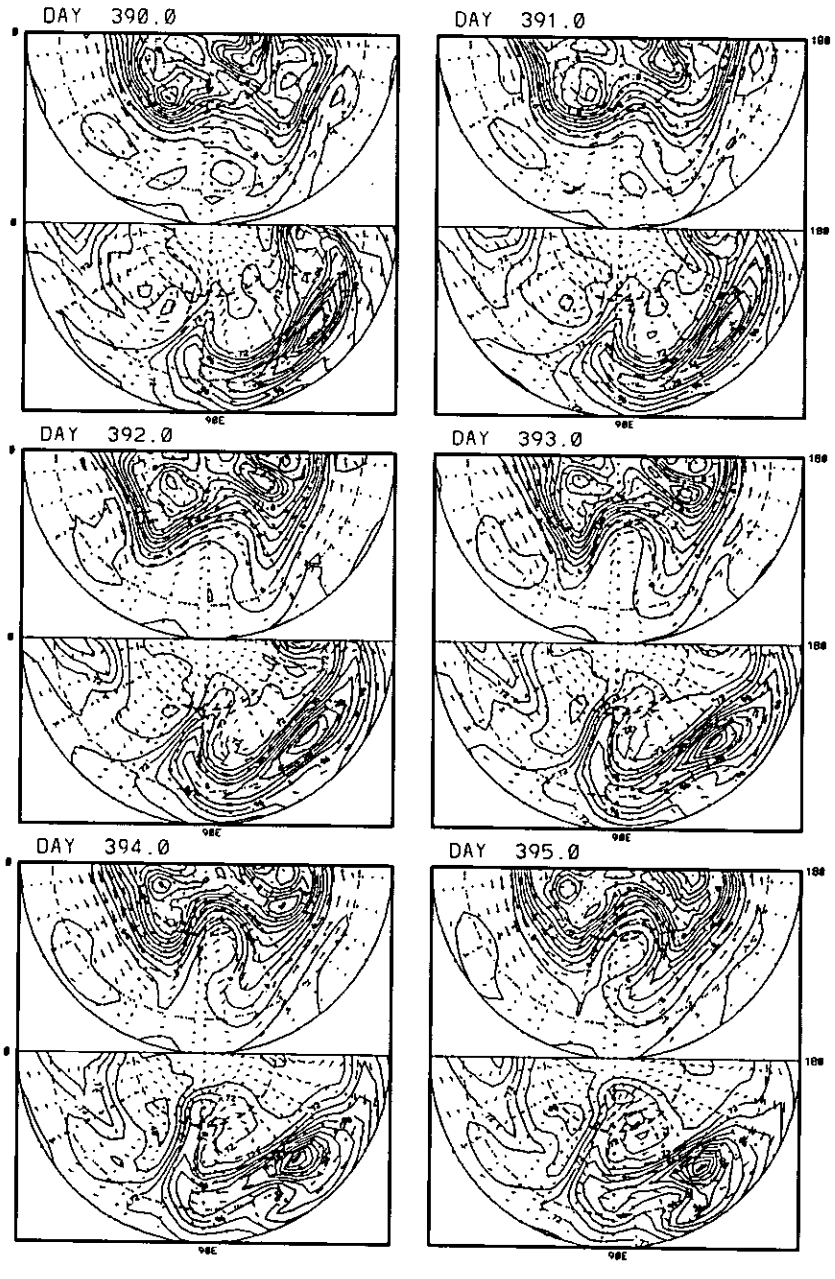

Figure 46: As in Fig. 11, except for the the streamfunction corresponding to the PV sequence of Fig. 45.

CHAPTER 13

Conclusions

We have used a two-layer isentropic primitive equation model to study the onset of blocking. Within the framework of the theory of barotropic and baroclinic instability of three-dimensional instantaneous basic state flows, we have tentatively postulated that the sets of normal modes, adjoint modes and singular vectors were instrumental in triggering the regime transition. Our investigation had a two-fold purpose. On one hand we intended to determine which of the above sets was most suitable to "warn" for possible transitions to blocks in ensemble forecasts, and, on the other hand, we intended to gain more insight into the mechanisms at work in the onset of blocks. The first goal directly relates to error growth in model forecasts, while the second goal concerns (structure) development. The two aspects (error growth and development) are, however, intertwined, as discussed by Frederiksen (1989). Indeed, the equations for error growth and development are identical in the approximation of slowly varying large amplitude part of the flow. We note that "slowly varying" means those cases when the large amplitude part of the flow changes more slowly than the perturbation (or equivalently, the error). Interestingly, however, even when the slowly varying approximation formally breaks down, it is still of practical validity if the amplitude of the perturbation is sufficiently small and it experiences a rapid growth just

prior to the alterations in the large scale flow and regime transitions. A number of studies have shown larger than usual linear instability of normal mode type just before rapid changes in the large amplitude flow configuration and regime transitions (*e.g.* Frederiksen 1984, 1989, Legras and Ghil 1985). A similar behavior was found in the present study. The flow was found anomalously unstable just prior to the onset of the blocks. As discussed by Frederiksen (1989), an empirical connection between development and error growth seems to hold in the nonlinear regime of the growth of perturbations as well.

The equivalence between error growth and development, and the assumption that the expanding and contracting directions in phase space defined by the normal modes determine the dynamically most active directions, constitute the basis for error theories rooted in normal modes. One such model is:

$$\frac{dE}{dt} = \alpha E - \beta E^2 \ , \tag{60}$$

where E is the forecast error with initial exponential growth rate α and asymptotic saturation due to non-linear effects at $E_\infty = \alpha/\beta$ Lorenz (1982). Theoretical developments in the theory of linear instability have shown, however, that singular vectors may be more suitable to capture the error growth , at least in the initial moments of the model integration (*e.g.* Lorenz 1965, Farrell 1984).

Various authors have previously considered the question of normal modes versus singular vectors in capturing the error growth in ensemble forecasts. In particular, Mureau *et al.*, (1993) have studied this problem in the more focused context of blocking predictability. However, because the method employed was always based on integrating the model with the

perturbations added to the initial condition, only small subsets of normal modes and singular vectors were actually studied. In this investigation, the relative importance of all and each one of these structures was investigated with help of the adjoint sensitivity analysis. The response function consisted of a daily projection of the upper-layer streamfunction anomaly onto a "mean blocking pattern." The latter was statistically derived from the model output. Two case studies were performed. The blocking episode was named *Block*1750 in the first case study and *Block*1899 in the second case study. *Block*1750 represented an event contained in the control run, while *Block*1899 was excited by adding selected perturbations to a control run free of blocks.

The time series of the blocking index and maximal sensitivity confirmed recent conclusions by Oortwijn and Barkmeijer (1996) that some transitions to blocks were predictable, while others were more difficult to predict. Both case studies performed in this investigation featured the "less predictable" blocks.

The synoptic description of both case studies showed that these particular blocks formed in two steps. The first step consisted of a LC1-type development of Thorncroft *et al.*, (1993) in the total streamfunction of the upper-layer. This trough development resulted in mid-latitude upper-layer cutoff or near cutoff cyclones. This development was accompanied by advection of high PV in the lower layer, beneath the region where the blocking ridge was to appear. The second step, as suggested here, consisted of a rapid intensification of the blocking ridge by exponential growth of leading normal modes.

The sensitivity analysis on both blocks showed that normal modes far distant in the spectrum, as ordered by decreasing growth rates, could be as important as the leading

(growing) normal modes in producing changes in the response function. In fact, in some cases, such distant normal modes were found to be relatively more important than the leading modes. A drawback usually associated with theories based on normal modes is that the question of how such structures could be achieved is rarely addressed. Zhang (1988) performed studies aimed at filling this gap. In particular, he introduced the concept of projectability, which is a measure of the degree of orthogonality of the normal modes. Shears in the flow cause the system to move away from self-adjointness, so that the normal modes can become strongly non-orthogonal to each other. This, in turn, allows the exchange of energy among the normal modes as well as small perturbations having large initial projections onto some of the normal modes. The projectability is a measure of the amplification of the initial projections of perturbations due to non-orthogonality. Modes that are orthogonal to the rest of the spectrum have a projectability of one. Large projectabilities indicate large deviations from orthogonality, and therefore large potential for initial growth. As discussed by Zhang (1988), the realization of the growth of any such modes with a large projectability requires a certain amount of time. That time can be estimated by the distance between that normal mode and its closest interfering mode in the complex eigenvalue space. It is however a firm conclusion that such modes may be as important as the leading exponentially growing modes, in initial value problems. For this reason, and in view of the results of the sensitivity analysis in this investigation, we suggest that error theory based on the first few exponentially growing normal modes are likely to yield poor results in blocking predictability.

Another important result obtained through the sensitivity analysis is that the phase

of the normal mode is crucial in determining its impact on the response function. Hence, the random phase ensemble average (RPEA) of quantities derived from the normal modes does not seem to be a very useful concept in blocking predictability, for it assumes an equal probability for every phase.

*Block*1899 was excited by superposing different perturbations onto the control run at day 1896. The results presented in this work suggest that the perturbation is optimal in the linear regime. The normal modes of day 1896 were not able to trigger the transition, while the first regional singular vector (SV) and the real phase of the adjoint of the fastest growing normal mode (FGNM) succeeded in producing the block. The structure of the real phase of the adjoint of the FGNM and the first SV were found to be remarkably similar. We will come back to this fact shortly.

From a dynamical point of view, we learned that the first step of the excitation of the blocks presented here featured LC1-type developing troughs in the upper-layer total streamfunction. The results for *Block*1899 showed, however, that an excessive thinning of the equatorward extending troughs was detrimental to block formation, for the trough in the control run eventually broke down without any cutoff cyclone having formed. This shows that the anticyclonic shear on the equatorward side of the jet has to have the right magnitude in order to prevent the decay of the trough, and to form a blocking high PV anomaly. This was made possible on *Block*1899 by adding a perturbation to the control run which behaved in a mostly LC2 manner. This perturbation canceled the anticyclonic ambient shear in excess, so that the formation of a cutoff blocking cyclone could materialize.

The importance of the interaction between synoptic-scale disturbances and the planetary

waves in atmospheric blocking has been suggested by various authors (*e.g.* Berggren *et al.*, 1949, Sanders and Gyakum 1980, Reinhold and Pierrehumbert 1982, Shutts 1983, Colucci 1985). The idea is that synoptic scale disturbances can act as sources of energy and potential vorticity that trigger a transition to a block or maintain a blocked flow. In particular, Colucci (1985) hypothesized that explosive surface cyclogenesis, with a corresponding upper level baroclinic disturbance, could be the key element in triggering the transition to the blocked state. His observational studies suggested that the specific initial position of the upper level disturbance and relative movement with respect to the large amplitude wave were crucial to the way the blocking pattern formed. When the surface cyclone was coupled with a 500mb synoptic scale wave migrating from a long-wave ridge to a long-wave trough a blocking cyclonic vortice formed. When the migration was from a long-wave trough to a long-wave ridge, however, a blocking anticyclonic vortice was observed. In our model, no development that satisfied the "boom" criteria of Gyakum and Sanders (1980) was observed in the total field, but yet blocks were able to form. We therefore strongly suggest that rather than simply concentrating on the deepening rate of surface cyclones and relative motion of the accompanying upper-level disturbances, one should also study the specific way the (upper and lower-level) cyclones are likely to develop. As a reference frame, it seems to be useful to concentrate on developments of the type LC1 and LC2 (Thorncroft *et al.*, 1993). The developments of the type LC1 presented in both case studies of this investigation are realistic. Supporting evidence is provided, for instance, by the UK fine-mesh analysis of potential temperature on the $PV = 2ms^2s^{-1}Kkg{-}1$ surface between $00\,GMT$ on 27 Jan. 1990 and $00\,GMT$ on 29 Jan. 1990, as reproduced in Thorncroft *et al.* (1993) (their

Fig. 14). For practical applications, we suggest that an assessment of the range of values of the ambient shear that can lead to LC1-type developments with resulting cutoff or near cutoff cyclones should be made in forecast centers.

The LC1-type development gave rise in our case studies to high PV cutoffs (or near cutoff) plus a quasi rectilinear jet, northwardly displaced from its climatological position. This configuration was found to support a stronger than usual instability of normal mode form. The relatively short *e*-folding times associated with the fastest growing normal modes around the time of the intensification of the blocking ridge supported our claim that the second step in the formation of the blocks presented here featured the rapid excitation of leading normal modes. These normal modes possessed dipole structures in the region of the block, and were stationary (*e.g.* FGNM's of days 1750 and 1900) or had periods larger than 20 days (FGNM of day 1899). Their adjoints modes were found to resemble leading normal modes of the preceding day. The resemblance between the leading adjoint modes of a given day and the leading normal modes of the previous day was found for at least four (4) days before the onset. However, the larger *e*-folding times associated with the normal modes calculated on the flow 2 days or earlier before the onset prompted us to rule out the possibility of a significant excitation of the leading normal modes at those times.

We found in case study 2 that the first regional singular vector of day 1896 resembled quite remarkably the real phase of the adjoint of the FGNM of the same day. In fact, although not shown, we found this to be a general result valid for basic states back in time until roughly 4 days before the onset. The resemblance is quite good even for singular vectors optimized over 2 days, and in some cases, for singular vectors optimized over 1.5

days. However, this resemblance disappears quite rapidly after the second or third singular vector (and adjoint mode). The resemblance is not accidental. It can be explained by the fact that the adjoint modes and the singular vectors at initial time must coincide with each other as the optimization time for the singular vectors approaches infinity. In practical terms, "infinity" can mean time intervals as small as 1.5 or 2 days. This is the case when the large scale amplitude flow becomes anomalously unstable.

The set of SV's was found to be the most adequate (among the sets of normal modes, adjoint modes and singular vectors) for predicting the onset of blocks three to four days ahead of time in ensemble forecasting. Studies of perturbations 6 days before the onset showed that nonlinearities needed to be considered in any optimization scheme, in order to appropriately capture the transition to the blocked state. We intended to circumvent the difficulties associated with a nonlinear optimization by using a stepwise linear theory. By dividing the time interval of 6 days into two consecutive time intervals of 3 days each, we were hoping to study the main features of the disturbances (6 days before the buildup) that produced the "preconditioning" of 3 days before the onset. However, a more adequate definition of a response function three days before the onset was revealed to be necessary. This seems to be the appropriate next step for the continuation of this investigation.

This work can be extended in various directions, namely:

1. Calculations of the PV balances can help in understanding why some perturbations are able to trigger the regime transition while others fail.

2. Calculations of the singular vectors on time varying basic state trajectories should be carried out in order to study whether an improvement in the 6 day forecast is achieved.

3. The study of the well predictable blocks versus the less predictable should be considered. Here, however, there is the disadvantage that the well predictable block must be found in the control run.

4. Blocks excited by different mechanisms should be studied in greater detail. Chapter 12 briefly describes an example of one such blocks.

5. The effects of using more realistic topographies must be considered. That topography is a necessary ingredient for the appearance of blocks in this model was seen by running the model without topography and plotting the response function. No block was observed in the course of 2000 day runs (with $\pi_\beta = 0.9$ and $\pi_\beta = 0.7$), although some short lived (less than 24 hours) blocked configurations were registered. We note here that the sensitivity studies of Zou *et al.*, (1993) indicated that the height of the mountain was the model parameter to which their response function was the most sensitive.

6. It is meaningful to investigate whether similar blocks form on a quasi-geostrophic version of the model, since, unlike for the primitive equation model, we understand fairly well the dynamics of the quasi-geostrophic approximation.

7. Basic state trajectories with a more " reliable connection" with the real word should be considered. By its very nature, the adjoint sensitivity technique is only applicable to response functions derived from the model state vector. One could however at least guarantee that the model yields a realistic climatology by including in the model equations forcing terms derived from observations.

Appendix A

Model Details

The model equations can be written in the continuous formulation as:

$$\frac{\partial(\zeta + f)}{\partial t} + \nabla.\mathbf{J} = 0 \tag{61}$$

$$\frac{\partial D}{\partial t} - \mathbf{k}.\nabla \times \mathbf{J} + \nabla^2\left(M + \frac{\mathbf{V}.\mathbf{V}}{2}\right) = 0 \tag{62}$$

$$\frac{\partial \sigma}{\partial t} + \nabla.(\mathbf{V}\sigma) + \frac{\partial(\dot{\theta}\sigma)}{\partial \theta} = 0 \tag{63}$$

$$\frac{\partial M}{\partial \theta} = \pi, \tag{64}$$

where ζ is the isentropic relative vorticity, f is the Coriolis parameter, $\mathbf{J} = [u(\zeta + f) + \dot{\theta}\frac{\partial v}{\partial \theta} - F_y]\mathbf{i} + [v(\zeta + f) - \dot{\theta}\frac{\partial u}{\partial \theta} + F_x]\mathbf{j}$ is the flux of vorticity per unit volume due to advective, adiabatic and frictional effects, θ is the potential temperature, $\mathbf{V} = u\mathbf{i} + v\mathbf{j}$ is the horizontal velocity on the θ-surface, D is the corresponding horizontal divergence, $M = c_pT + gz_s = \pi\theta + gz_s$ is the Montgomery potential, T is the temperature, c_p is the specific heat at constant pressure, z_s is the topography, $\pi = c_p(p/p_o)^{R/c_p}$ is the Exner function, R is the gas constant for the dry atmosphere, and $\sigma = -(1/g)(\partial p/\partial\theta)$ is the isentropic mass density. $F_{x,y}$ represents the x and y-components of the frictional force. They are made up of a term for the Ekman dissipation in the lower layer and a term that represents a numerical viscosity to avoid the accumulation of enstrophy in the smaller scales

of motion. In vector form:

$$\mathbf{F} = \left(\alpha \bigtriangledown^{\nu} - \frac{\delta_{k1}}{\tau_{drag}} \right) \mathbf{k} \times \mathbf{V}, \tag{65}$$

where α is a constant with the dimension of an inverse time, $\nu = 12$, k is the unit vector in the direction perpendicular to the surface θ=constant, δ_{k1} is the Kronecker delta symbol, and τ_{drag} is the time-scale of the Rayleigh friction.

In our notation, $k = 1$ stands for the lower layer and $k = 2$ for the upper layer. Note also that all those quantities referred above which are extensive enter the equations as "quantity per unit mass."

For simplicity, the Boussinesq approximation has been used, allowing a linear relationship between σ and M:

$$\sigma = -(p_o / R\theta_o)(\partial \pi / \partial \theta). \tag{66}$$

Relation (66) is obtained by rewriting the isentropic mass density as:

$$\sigma = \rho_a \frac{\partial z_a}{\partial \theta}, \tag{67}$$

where

$$\rho_a = \frac{p_o}{R\theta_o} \left(\frac{\pi}{c_p} \right)^{c_v/R} \tag{68}$$

$$z_a = \frac{\theta_o}{g}(c_p - \pi) \tag{69}$$

are the density and height in an isentropic atmosphere with potential temperature θ_o. Assuming that $\rho_a = \rho_o = p_o/R\theta_o$, we readily obtain (66).

With help of (66), and by integrating the hydrostatic equation (64) along θ, taking into account the boundary conditions of no mass transfer across the upper and lower boundaries, $\dot{\theta}_{5/2} = \dot{\theta}_{1/2} = 0$, we obtain the following system of (discretized) predictive equations:

$$\frac{\partial \zeta_k}{\partial t} + \nabla.(A_k, B_k) = 0 \tag{70}$$

$$\frac{\partial D_k}{\partial t} + \nabla.(-B_k, A_k) + \nabla^2[gz_s + \frac{1}{2}(u_k^2 + v_k^2)] + \nabla^2 M_k^{'} = 0 \tag{71}$$

$$\frac{\partial \Delta\pi_k^{'}}{\partial t} + \nabla.(u_k\Delta\pi_k^{'}, v_k\Delta\pi_k^{'}) + \Delta\overline{\pi}_k D_k = (-1)^k \frac{\pi_e - \pi_{mid} - \Delta\pi_2^{'}}{\tau_{diab}}, \tag{72}$$

where

$$A_k = u_k(\zeta_k + f) + \dot{\theta}_{3/2}\frac{\Delta\pi_1 + \Delta\pi_2}{2\Delta\theta\Delta\pi_k}(v_2 - v_1) - (\alpha\nabla^\nu - \frac{\delta_{k1}}{\tau_{drag}})v_k \tag{73}$$

$$B_k = v_k(\zeta_k + f) - \dot{\theta}_{3/2}\frac{\Delta\pi_1 + \Delta\pi_2}{2\Delta\theta\Delta\pi_k}(u_2 - u_1) + (\alpha\nabla^\nu - \frac{\delta_{k1}}{\tau_{drag}})u_k \tag{74}$$

$$\Delta\overline{\pi}_1 = c_p - \pi_{mid}$$

$$\Delta\overline{\pi}_2 = \pi_{mid} - \pi_{5/2}$$

$$\pi_{mid} = \frac{1}{2}(c_p + \pi_{top})$$

$$\pi_{top} = Constant$$

$$\Delta\pi_k = \pi_{k-1/2} - \pi_{k+1/2}$$

$$= \Delta\overline{\pi}_k + \Delta\pi_k^{'}$$

$$M_k = \overline{M}_k + M_k^{'}$$

$$\overline{M}_1 = (\Delta\overline{\pi}_1 + \Delta\overline{\pi}_2 + \pi_{5/2})\theta_1 + gz_s$$

$$\overline{M}_2 = \overline{M}_1 + (\Delta\overline{\pi}_2 + \pi_{5/2})\Delta\theta$$

$$M_1' = (\Delta\pi_1' + \Delta\pi_2')\theta_1$$

$$M_2' = M_1' + \Delta\pi_2'\Delta\theta$$

$$\Delta\theta = \theta_2 - \theta_1.$$

The Arakawa scheme has been used in discretizing the nonlinear terms. The subscripts 1/2, 3/2 and 3/2 denote quantities evaluated at the surface, interface and upper surface, respectively. The Newtonian drive is defined by prescribing an equilibrium interface Exner function, π_e, and a relaxation time, τ_{diab}. The following relation holds:

$$\dot{\theta}_{3/2} = \frac{(\pi_e - \pi_{3/2})\Delta\theta}{\tau_{diab}(\Delta\pi_2 + \Delta\pi_1)}. \tag{75}$$

The equilibrium interface Exner function, π_e, has been chosen to be independent of longitude λ:

$$\pi_e = \pi_{mid} - \frac{1}{2}\pi_\beta(c_p - \pi_{mid})cos\,2\phi\,(sin^2\,2\phi + 2), \tag{76}$$

where ϕ is the latitude and π_β is a parameter that controls the slope of the interface in the north-south direction. The topography is a wavenumber 2 function in the zonal direction:

$$z_s = 4h_o(\mu^2 - \mu^4)\,sin\,2\lambda, \tag{77}$$

where $\mu = sin\,\phi$.

Parameter values for this study are:

$\theta_1 = 280\,K$, $\theta_2 = 320\,K$, $p_o = 1000\,mb$, $z_{top} = (\theta_1/g)(c_p - \pi_{5/2}) = 10^4\,m$, $\nu = 12$, $\tau_{drag} = 5\,days$, $\tau_{diab} = 15\,days$, $\alpha^{-1} = 3\,hours$, $\pi_\beta = 0.9$ and $h_o = 2000\,m$.

The potential vorticity (PV) in this model is defined as

$$(PV)_k = \frac{R\,g\,\Delta\theta}{p_o}\,\frac{\zeta_k + f}{\Delta\pi_k}. \tag{78}$$

Appendix B

Total Perturbation Energy

We start by deriving the expression for the total energy in the nonlinear model. The corresponding expression for the perturbation in the linearized model is easily obtained from the first.

Since we are merely interested in the expression for the total energy, rather than in the exact equation for its tendency, we can proceed without diabatic heating and without friction. These, when included in the equation for the energy tendency, will simply yield sources and sinks of energy.

The vorticity and divergence equations presented in appendix A were derived from the nonlinear momentum equations. These can be written for a frictionless and adiabatic atmosphere as:

$$\frac{\partial u_i}{\partial t} + \frac{\partial}{\partial x_i}\frac{u_j u_j}{2} + (\zeta + f)\,\varepsilon_{imn}\,k_m\,u_n = -\frac{\partial M}{\partial x_i}. \tag{79}$$

We have used the tensor-notation in writing (79). The summation rule is assumed, and ε_{imn} is the antisymmetric tensor. Clearly, in our case $u_3 = 0$, $k_1 = k_2 = 0$ and $k_3 = 1$.

Relation (79) and the equation for the Exner-thickness:

$$\frac{\partial(\Delta\pi)}{\partial t} + \Delta\pi\,\frac{\partial u_i}{\partial x_i} + u_i\,\frac{\partial(\Delta\pi)}{\partial x_i} = 0 \tag{80}$$

are valid in both layers.

Multiplying (79) by $\Delta\pi\, u_i$, and noting in the process that $u_i\, \varepsilon_{imn}\, k_m\, u_n = 0$, we obtain, with very little manipulation:

$$\frac{\partial}{\partial t}\left(\Delta\pi \frac{u_i u_i}{2}\right) - \frac{u_i u_i}{2}\frac{\partial(\Delta\pi)}{\partial t} + \frac{\partial}{\partial x_i}\left(\Delta\pi u_i \frac{u_j u_j}{2}\right) - \frac{u_j u_j}{2}\frac{\partial}{\partial x_i}(\Delta\pi u_i) = -\Delta\pi \frac{\partial(u_i M)}{\partial x_i} + \Delta\pi M\left(\frac{\partial u_i}{\partial x_i}\right). \tag{81}$$

In view of (80), the second and fourth terms on the left hand side of (81) add up to zero. Also in view of (80), the last term on the right hand side of (81) can be rewritten as:

$$\Delta\pi M \frac{\partial u_i}{\partial x_i} = -M\,\frac{\partial \Delta\pi}{\partial t} - M u_i\left(\frac{\partial \Delta\pi}{\partial x_i}\right). \tag{82}$$

Taking (82) into account, we rewrite (81) as:

$$\frac{\partial}{\partial t}\left(\Delta\pi \frac{u_i u_i}{2}\right) + M\frac{\partial(\Delta\pi)}{\partial t} = -\frac{\partial}{\partial x_i}(\Delta\pi\, u_i \frac{u_j u_j}{2} + \Delta\pi M u_i). \tag{83}$$

By integrating on the x-y plane, summing over both layers ($k = 1$ and $k = 2$) and taking into account that $\Delta\pi_k = \pi_{k-1/2} - \pi_{k+1/2}$, $M_1 = (\Delta\pi_1 + \Delta\pi_2 + \pi_{5/2})\theta_1 + g z_s$ and $M_2 = M_1 + (\Delta\pi_2 + \pi_{5/2})\Delta\theta$ (see appendix A), it is not difficult to show that (81) yields:

$$\frac{\partial \mathcal{E}}{\partial t} = 0, \tag{84}$$

where

$$\mathcal{E} = \int \left\{ \sum_{k=1}^{2} (\Delta\pi_k \frac{|\mathbf{u}_k|^2}{2}) + \frac{\pi_{3/2}^2 \Delta\theta}{2} + \frac{M_1^2}{2\theta_1} \right\} dx\, dy. \tag{85}$$

It is clear that E is the total energy. Note the usual vector notation in (85).

Writing $\mathbf{u}_k = \mathbf{u}_k^o + \mathbf{u}_k'$, $\pi_{3/2} = \pi_{3/2}^o + \pi_{3/2}'$, $\Delta\pi_k \approx \Delta\pi_k^o$ and $M_1 = M_1^o + M_1'$, where the superscript "o" indicates quantities evaluated on a reference trajectory and the primes stand for perturbations, we can immediately pull out from (85) those terms which are quadratic in the perturbation and write for the integrated total perturbation energy, E':

$$E' = \int \left\{ \sum_{k=1}^{2} (\Delta\pi_k^o \frac{|\mathbf{u}'|^2}{2}) + \frac{\pi_{3/2}'^2 \Delta\theta}{2} + \frac{M_1'^2}{2\theta_1} \right\} dx\, dy. \tag{86}$$

Taking into account that $M_1' = \pi_{1/2}'\theta_1$ and $\Delta\pi_k^o \approx \Delta\overline{\pi_{ok}} = \Delta\pi_o$, where $\Delta\pi_o$ is constant in this model (see appendix A), we obtain:

$$E = \frac{E'}{\Delta\overline{\pi}_o} = \int \left\{ \sum_{k=1}^{2} (\frac{|\mathbf{u}'|^2}{2}) + \frac{\Delta\theta}{2\Delta\overline{\pi}_o} \pi_{3/2}'^2 + \frac{\theta_1}{2\Delta\overline{\pi}_o} \pi_{1/2}'^2 \right\} dx\, dy. \tag{87}$$

For convenience, we shall call E the integrated total perturbation energy.

Appendix C

Construction of the Weights Matrix in the Energy Norm

Taking into account that the i^{th} component of the perturbation wind velocity in each layer is given by

$$u_i^{'} = \varepsilon_{imn}\, k_m \frac{\partial \psi^{'}}{\partial x_n} + \frac{\partial \chi^{'}}{\partial x_i}, \tag{88}$$

where $\psi^{'}$ is the perturbation streamfunction and $\chi^{'}$ is the perturbation velocity potential, and by representing $\psi^{'}$, $\chi^{'}$, $\pi_{1/2}^{'}$ and $\pi_{3/2}^{'}$ in terms of spherical harmonics, its is not difficult to show that the integrated total perturbation energy E (see appendix B) can be written as:

$$E = \sum_{k=1}^{2} \left\{ \sum_{nm} \left[\frac{n(n+1)}{a^2} \left(|\psi_{nm}^{'}|^2 + |\chi_{nm}^{'}|^2 \right) \right] + \frac{\Delta\theta}{2\Delta\overline{\pi}_o} |\pi_{3/2nm}^{'}|^2 + \frac{\theta_1}{2\Delta\overline{\pi}_o} |\pi_{1/2nm}^{'}|^2 \right\}. \tag{89}$$

In (89), a is the mean radius of the earth, and quantities with a subscript "nm" are (complex) spectral coefficients.

Knowing that

$$\zeta_{nm}^{'} = -\frac{a^2}{n(n+1)} \psi_{nm}^{'} \tag{90}$$

and

$$D'_{nm} = -\frac{a^2}{n(n+1)}\chi'_{nm}, \tag{91}$$

where ζ' and D' are the vorticity and divergence of the perturbation, respectively, the constructions of the diagonal matrix $\mathcal{D}$ is a matter of triviality. It follows from the imposition that $(\delta\mathbf{x})^T\mathcal{D}(\delta\mathbf{x})$ must yield the integrated total perturbation energy. Note that the state vector of the linearized problem, $\delta\mathbf{x}$, must be given in spectral form and in real representation. Also, it must be defined in terms of $\pi'_{1/2}$ and $\pi'_{3/2}$, instead of $\Delta\pi'_1$ and $\Delta\pi'_2$.

Appendix D

Real Representation of the Propagator for Time Invariant Basic State Trajectories

The singular vectors are calculated with real matrices. We chose to compute the propagator exactly with help of the eigenvectors, adjoint eigenvectors and corresponding eigenvalues of the linear evolution operator, L.

The arbitrariness in choosing the phase and normalization of the eigenvectors and adjoint eigenvectors is used to our advantage to set up a biorthonormal system of the real and imaginary phases. The set of the real and imaginary phases of the eigenvectors is denoted by $\{|\phi_n>\}$, and that of the adjoint eigenvectors by $\{<\phi_n^{adj}|\}$. For convenience, the Dirac notation of "ket ($|\cdots>$)" and "bra ($<\cdots|$)"-vectors (*e.g.*, Schubert and Weber 1978) will be used throughout this appendix. This is legitimate, since the original (complex) vector space of the perturbations is a Hilbert space. In practice, the symbol "$<|$" is to be associated with the operation of transpose.

The biorthonormality relation can be written as:

$$<\phi_m^{adj}|\phi_n>=\delta_{mn}, \tag{92}$$

where δ_{mn} is the Kronecker delta symbol.

In our notation, if "n" corresponds to the real phase of a given eigenvector, then "$(n+1)$" is associated with its imaginary phase. The eigenvalue problem for the eigenvectors can be expressed as:

$$L|\phi_n> = \sigma_n|\phi_n> - \sigma_{n+1}|\phi_{n+1}> \tag{93}$$

$$L|\phi_{n+1}> = \sigma_n|\phi_{n+1}> + \sigma_{n+1}|\phi_n>, \tag{94}$$

where σ_n and σ_{n+1} are the real and imaginary parts of the eigenvalue, respectively.

The completeness of the base set $\{|\phi_n>\}$ can be expressed by:

$$I = \sum_n |\phi_n><\phi_n^{adj}|, \tag{95}$$

where I is the unit operator. It is sufficient to assume here that the adjoint eigenvectors are calculated in the L_2 norm. The method can however be extended to any norm by properly re-identifying the ket-vectors.

For a time invariant basic state the propagator R_τ between time $t = 0$ and $t = \tau$ can be expressed as

$$R_\tau = IRI = Ie^{L\tau}I = \sum_n \sum_m |\phi_n><\phi_n^{adj}|e^{L\tau}|\phi_m><\phi_m^{adj}|. \tag{96}$$

Three different cases can be considered:

1. $|\phi_m>$ **is associated with a real eigenvalue** σ_m . Then,

$$\sum_n |\phi_n><\phi_n^{adj}|e^{L\tau}|\phi_m> = \sum_n |\phi_n> e^{\sigma_m \tau}\delta_{nm}. \tag{97}$$

It follows that

$$\sum_n \sum_m |\phi_n >< \phi_n^{adj}| e^{L\tau} |\phi_m >< \phi_m^{adj}| = \sum_m |\phi_m > e^{\sigma_m \tau} < \phi_m^{adj}|, \tag{98}$$

for all m associated with real eigenvalues.

2. $|\phi_m >$ **is the real phase of a complex eigenvector (and** $|\phi_{m+1} >$ **is the imaginary phase).** Then, by virtue of (94) and the biorthonormality relation (92), we have:

$$\sum_n |\phi_n >< \phi_n^{adj}| e^{L\tau} |\phi_m >= |\phi_m > e^{\sigma_m \tau}(cos\, \sigma_{m+1}\tau) - |\phi_{m+1} > e^{\sigma_m \tau}(sin\, \sigma_{m+1}\tau). \tag{99}$$

We will introduce the summation over m at a later stage.

3. $|\phi_m >$ **is the imaginary phase of the complex eigenvector (and** $|\phi_{m-1} >$ **is the real phase)** . Then, by virtue of (94) and the biorthonormality relation (92), we have:

$$\sum_n |\phi_n >< \phi_n^{adj}| e^{L\tau} |\phi_m >= |\phi_m > e^{\sigma_{m-1}\tau}(cos\, \sigma_m \tau) + |\phi_{m-1} > e^{\sigma_{m-1}\tau}(sin\, \sigma_m \tau). \tag{100}$$

Combining the first term on the r. h. s. of (99) with the second term on the r. h. s. of (100), and summing over m , we obtain:

$$\sum_n \sum_m |\phi_n >< \phi_n^{adj}| e^{L\tau} |\phi_m >< \phi_m^{adj}| =$$
$$\sum_m |\phi_m > e^{\sigma_m \tau}\{(cos\, \sigma_{m+1}\tau) < \phi_m^{adj}| + (sin\, \sigma_{m+1}\tau) < \phi_{m+1}^{adj}|\}, \tag{101}$$

for all m **so that** $|\phi_m >$ **is the real part of a complex eigenvector.**

In the same way, by combining the first term on the r. h. s. of (100) with the second term on the r. h. s. of (99), and summing over m, we obtain:

$$\sum_n \sum_m |\phi_n >< \phi_n^{adj}| e^{L\tau} |\phi_m >< \phi_m^{adj}| =$$
$$\sum_m |\phi_m > e^{\sigma_{m-1}\tau} \{(cos\, \sigma_m \tau) < \phi_m^{adj}| - (sin\, \sigma_m \tau) < \phi_{m-1}^{adj}|\}, \qquad (102)$$

for all m so that $|\phi_m >$ is the imaginary part of a complex eigenvector.

Equations (98), (101), and (102) give us the representation that we were after. These expressions may seem somewhat complicated at first sight, but they are in reality easy to code, if we view them from a "matrix perspective." Suppose, for the sake of clarity, that the eigenvalues of the system are all real. Then the representation would be given by (98). In matrix form, we would write:

$$R_\tau = E \Lambda A^T, \qquad (103)$$

where E is the matrix of column (real) eigenvectors, Λ is a diagonal matrix of elements $e^{\sigma_m \tau}$ and A is the matrix of column (real) adjoint eigenvectors.

In the most general case of complex eigenvectors, (101) and (102) must be incorporated in the representation. Taking a closer look at these relations, we recognize in the expressions inside the curly brackets plane rotations of the complex vectors $< \phi_m^{adj}| + i < \phi_{m+1}^{adj}|$ by an angle $(-\sigma_{m+1}\tau)$. In matrix form, (103) is still valid, provided that Λ is modified such that at an entry corresponding to the real phase of a complex eigenvector, instead of the element $e^{\sigma_m \tau}$, we accomodate the following 2×2 submatrix:

$$\begin{pmatrix} e^{\sigma_m \tau}(\cos \sigma_{m+1}\tau) & e^{\sigma_m \tau}(\sin \sigma_{m+1}\tau) \\ -e^{\sigma_m \tau}(\sin \sigma_{m+1}\tau) & e^{\sigma_m \tau}(\cos \sigma_{m+1}\tau) \end{pmatrix}.$$

The element $e^{\sigma_m \tau}(\cos \sigma_{m+1}\tau)$ of the submatrix must occupy that entry.

References

Ahlquist, J. E. 1985: Climatology of normal mode Rossby waves. *J. Atmos. Sci.*, **42**, 2059-2068.

Andrews, D. G. 1984: On the stability of forced non-zonal flows. *Quart. J. Roy. Meteor. Soc.*, **110**, 657-662.

Baines, P. G. 1983: A survey of blocking mechanisms, with application to the Australian region. **Aust. Met. Mag.**, **31**, 27-36.

Berggren, R., Bolin, B. and Rossby, C. G. 1949: An aerological study of zonal motion, its perturbations and breakdown. *Tellus*, **1**, **2**, 14-37.

Bettge, T. W. 1983: A systematic error comparison between the ECMWF and NMC prediction models. *Mon. Wea. Rev.*, **111**, 2385-2389.

Borges, M. D. and Hartmann, D. L. 1992: Barotropic Instability and Optimal Perturbations of Observed Nonzonal Flows. *J. Atmos. Sci.*, **49**, 335-354.

Boyd, J. P. 1983: The continuous spectrum of linear Couette flow with the beta effect. *J. Atmos. Sci.*, **40**, 2304-2308.

Bretherton, F. P. 1966: Critical layer instability in baroclinic flows. *Quart. J. Roy. Meteor. Soc.*, **92**, 325-334.

Buizza, R., Tribbia, J., Molteni, F. and Palmer, T. N. 1993: Computation of optimal unstable structures for a numerical weather prediction model. *Tellus*, **45A**, 388-407.

Buizza, R. and Palmer, T. N. 1995: The Singular-Vector Structure of the Atmospheric General Circulation (submitted to the *J. Atmos. Sci.*).

Burger, A. P. 1962: On the existence of critical wavelengths in a continuous baroclinic stability problem. *J. Atmos. Sci.*, **19**, 31-38.

Burger, A. P. 1966: Instability associated with the continuous spectrum in a baroclinic flow. *J. Atmos. Sci.*, **23**, 272-277.

Buzzi, A. and Tibaldi, S. 1978: Cyclogenesis in the lee of the Alps: a case study. *Quart. J. Roy. Meteor. Soc.*, **104**, 271-287.

Cai, M. and Mak, M. 1990: On the Basic Dynamics of Regional Cyclogenesis. *J. Atmos. Sci.*, **47**, 1417-1442.

Cacuci, D. G. 1981: Sensitivity theory for nonlinear systems. I. Nonlinear functional analysis approach. *J. Math. Phys.*, **22**, 2794-2802.

Cacuci, D. G. 1981: Sensitivity theory for nonlinear systems. II. Extensions to additional classes of responses. *J. Math. Phys.*, **22**, 2803-2812.

Case, K. M. 1960: Stability of inviscid plane Couette flow. *Phys. Fluids*, **3**, 143-148.

Charney, J. G. 1947: The dynamics of long waves in a baroclinic westerly current. *J. Meteor.*, **4**, 135-162.

Charney, J. G. 1971: Geostrophic turbulence. *J. Atmos. Sci.*, **28**, 1087-1095.

Charney, J. G. and DeVore, J. G. 1979: Multiple flow equilibria in the atmosphere and blocking. *J. Atmos. Sci.*, **36**, 1205-1216.

Charney, J. G. and Strauss, D. M. 1980: Form-drag instability, multiple equilibria and propagating planetary waves in baroclinic, orographically forced, planetary wave systems. *J. Atmos. Sci.*, **37**, 1157-1176.

Charney, J. G., Shukla, J. and Mo, K. D. 1981: Comparison of barotropic blocking theory with observation. *J. Atmos. Sci.*, **38**, 762-779.

Colucci, S. J. 1985: Explosive cyclogenesis and large scale circulation changes: Implications for the onset of blocking. *J. Atmos. Sci.*, **42**, 2701-2717.

Colucci, S. and Alberta, T. L. 1995: Planetary Scale Climatology of Explosive Cyclogenesis and Blocking (submitted to the Mon. Wea. Rev.).

Davies, H. C., Shär, CH. and Wernli, H. 1991: The Palette of Fronts and Cyclones within a Baroclinic Wave Development. *J. Atmos. Sci.*, **48**, 1666-1689.

Deland, R. , J. 1964: Traveling planetary scale waves. *Tellus*, **16**, 271-273.

Dole, R. M. 1986: The life cycles of persistent anomalies and blocking over the North Pacific. *Adv. Geophys.*, **29**, 31-69.

Dole, R. M. and Black, R. X. 1990: Life cycles of persistent anomalies. Part II: The development of persistent negative height anomalies over the North Pacific ocean. *Mon. Wea. Rev.*, **118**, 824-846.

Eady, E. T. 1949: Long waves and cyclone waves. *Tellus*, **1**, 33-52.

Egger, J. 1978: Dynamics of blocking highs. *J. Atmos. Sci.*, **35**, 1788-1801.

Elliot, R. D. and Smith, T. B. 1949: A study of the effects of large blocking highs on the general circulation in the northern hemisphere westerlies. *J. Meteorol.*, **6**, 67-85.

Farrell, B. 1982: The Initial Growth of Disturbances in a Baroclinic Flow. *J. Atmos. Sci.*, **39**, 1663-1686.

Farrell, B. 1984: Modal and Non-Modal Baroclinic Waves. *J. Atmos. Sci.*, **41**, 668-673.

Farrell, B. 1988: Optimal Excitation of Neutral Rossby Waves. *J. Atmos. Sci.*, **45**, 163-172.

Farrell, B. 1989: Optimal Excitation of Baroclinic waves. *J. Atmos. Sci.*, **46**, 1193-1206.

Flierl, G., Larichev, V., McWilliams, J. and Reznik, G. 1980: The dynamics of baroclinic and barotropic solitary eddies. *Dyn. Atmos. Oceans*, **45**, 1-41.

Frederiksen, J. S. 1979: The effect of long planetary waves on the regions of cyclogenesis: linear theory. *J. Atmos. Sci.*, **36**, 195-204.

Frederiksen, J. S. 1982: A unified three-dimensional instability theory of the onset of blocking and cyclogenesis. *J. Atmos. Sci.*, **39**, 970-982.

Frederiksen, J. S. 1983: The onset of blocking and cyclogenesis: linear theory. *Aust. Met. Mag.*, **31**, 15-26.

Frederiksen, J. S. 1984: The onset of blocking and cyclogenesis in Southern Hemisphere synoptic flows: Linear theory. *J. Atmos. Sci.*, **41**, 1116-1131.

Frederiksen, J. S. 1986: Instability theory and nonlinear evolution of blocks and mature anomalies. *Adv. Geophys.*, Vol. **29**, Academic Press, 277-303.

Frederiksen, J. S. 1989: The role of instability during the onset of blocking and cyclogenesis in Northern Hemisphere synoptic flows. *J. Atmos. Sci.*, **46**, 1076-1092.

Frederiksen, S. F. and Frederiksen J. S. 1992: Northern Hemisphere Storm Tracks and Teleconnection Patterns in Primitive Quasigeostrophic Models. *J. Atmos. Sci.*, **49**, 1443-1458.

Frederiksen, J. S. and Bell. R. C. 1987: Teleconnection patterns and the roles of baroclinic, barotropic and topographic instabilities. *J. Atmos. Sci.*, **44**, 2200-2218.

Frederiksen, J. S. and Bell. R. C. 1990: North Atlantic blocking during January 1979. Linear theory. *Quart. J. Roy. Meteor. Soc.*, **116**, 1289-1313.

Frederiksen, J. S. and Webster. P. J. 1988: Alternative Theories of Atmospheric Teleconnections and Low-frequency Fluctuations. *Rev. Geophys.*, **26**, 459-494.

Garcia, R. R. and Geisler, J. E. 1981: Stochastic forcing of small-amplitude oscillations in the stratosphere. *J. Atmos. Sci.*, **38**, 2187-2197.

Garriot, E. B. 1904: Long-range forecasts. *U. S. Wea. Bur. Bull.*, **35**.

Haines, K. and Marshall, J. 1987: Eddy-forced coherent structures as a prototype for atmospheric blocking. *Quart. J. Roy. Meteor. Soc.,* **113**, 681-704.

Hall, M. C. G. and Cacuci, D. G. 1983: Physical Interpretation of the Adjoint Functions for Sensitivity Analysis of Atmospheric Models. *J. Atmos. Sci.,* **40**, 2537-2546.

Haltiner, G. J. 1967: The effect of sensible heat exchange on the dynamics of baroclinic waves. *Tellus,* **19**, 183-198.

Held, I. M. 1985: Pseudomomentum and the orthogonality of modes in shear flows. *J. Atmos. Sci.,* **42**, 2280-2288.

Hirota, I. 1971: Excitation of planetary Rossby waves in the winter stratosphere by periodic forcing. *J. Meteor. Soc. Japan.,* **49**, 439-448.

Holopainen, E. O. and Fortelius, C. 1987: High frequency transient eddies and blocking. *J. Atmos. Sci.,* **44**, 1632-1645.

Hoskins, B. J., McIntyre, M. E. and Robertson, A. W. 1985: On the use and significance of isentropic potential vorticity maps. *Quart. J. Roy. Met. Soc.,* **111**, 877-946.

Hoskins, B. J. and Sardeshmukh, P. D. 1987: Transient eddies and the seasonal mean rotational flow. *J. Atmos. Sci.,* **44**, 328-338.

Illary, L. and Marshall, J. C. 1983: On the interpretation of the eddy fluxes. *J. Atmos. Sci.,* **40**, 2232-2242.

Jeffreys, H. and Jeffreys, B. 1956: Methods of Mathematical Physics. *Cambridge University Press,* 718pp.

Ji, L. R. and Tibaldi, S. 1983: Numerical Simulations of a Case of Blocking: The Effects of Orography and Land-Sea Contrast. *Mon. Wea. Rev.,* **111**, 2068-2086.

Kaas, E. and Branstator, G. 1993: *J. Atmos. Sci.,* **50**, 3061-3077.

Kalnay-Rivas, E. and Merkine, L-O. 1981: A simple mechanism for blocking. *J. Atmos. Sci.,* **38**, 2077-2091.

Källen, E. 1982: Bifurcation of quasi-geostrophic barotropic models and their relation to atmospheric blocking. *Tellus,* **34**, 225-265.

Lacarra, J. F. and Talagrand, O. 1988: Short range evolution of small perturbations in a barotropic model. *Tellus,* **40A**, 81-95.

Larichev, V. D. and Reznik, G. M. 1976: Two-dimensional Rossby soliton: and exact solution. *Polymode News* **19**, (also Reports of USSR Academy of Sciences, 231-235).

Legras, B. and Ghil, M. 1985: Persistent anomalies, blocking and variations in atmospheric

predictability. *J. Atmos. Sci.*, **42**, 443-471.

Le Dimet, F.-X. and Talagrand, O. 1986: Variational algorithms for analysis and assimilation of meteorological observations: Theoretical aspects. *Tellus*, **38A**, 97-110.

Le Dimet, F.-X., Ngodock, H. E. and Navon, I. M. 1995: Sensitivity Analysis in Variational Data Assimilation. *Tech. Rep.*. FSU-SCRI-95T-103, Florida State University, Tallahassee, Florida 32306-4052, 21pp.

Lejenäs, H. and Økland, H. 1983: Characteristics of the Northern Hemisphere Blocking as determined from a long time series of observational data. *Tellus*, **35A**, 350-362.

Levine, H. and Schwinger, J. 1949: On the theory of diffraction by an aperture in an infinite plane screen. *Phys. Rev.*, **75**, 1423-1432.

Liu, Q. 1994: On the definition and persistence of blocking. *Tellus*, **46A**, 286-298.

Liu, Q. and Opsteegh, T. 1995: Interannual and decadal variations of blocking activity in a quasi-geostrophic model. *Tellus*, **47A**, 941-954.

Long, R. R. 1964: Solitary waves in the westerlies. *J. Atmos. Sci.*, **21**, 197-200.

Lorenz, E. N. 1965: A study of the predictability of a 28-variable atmospheric model. *Tellus*, **17**, 321-333.

Madden, R. A. 1975: Oscillations in the winter stratosphere. Part II: The role of horizontal heat transports and the interaction of transient and stationary planetary waves. *Mon. Wea. Rev.*, **103**, 717-729.

Madden, R. A. 1979: Observations of large-scale traveling Rossby waves. em Rev. Geophys. Space Phys., **17**, 1935-1949.

Mak, M. and Cai, M. 1989: Local Barotropic Instability. *J. Atmos. Sci.*, **46**, 3289-3311.

McWilliams, J. C. 1980: An application of equivalent modons to atmospheric blocking. *Dyn. Atmos. Oceans.*, **5**, 43-66.

Mitchel, H. and Derome, J. 1983: Blocking-like solutions of the potential vorticity equation: Their stability at equilibrium and growth at resonance. *J. Atmos. Sci.*, **40**, 2522-2536.

Molteni, F. and Palmer, T. N. 1993: Predictability and finite-time instability of the northern winter circulation. *Quart. J. Roy. Meteor. Soc.*, **119**, 269-298.

Molteni, F., Buizza, R., Palmer, T. N. and Petroliagis, T. 1996: The ECMWF Ensemble Prediction System: Methodology and Validation. *Quart. J. Roy. Meteor. Soc.*, **112**, 73-119.

Moore, M. A. and Farrell, B. F. 1993: Rapid Perturbation Growth on Spatially and Temporally Varying Oceanic Flows Determined Using an Adjoint Method: Applications to the Gulf Stream. *J. Phys. Oceanogr.*, **23**, 1682-1702.

Mureau, R., Molteni, F. and Palmer, T. N. 1993: Ensemble prediction using dynamically conditioned perturbations. *Quart. J. Roy. Meteor. Soc.*, **119**, 299-323.

Namias, J. 1947: Characteristics of the general circulation over the northern hemisphere during the abnormal winter 1946-1947. *Mon. Wea. Rev.*, **75**, 145-152.

Namias, J. 1950: The index cycle and its role in the general circulation. *J. Meteor.*, **7**, 130-139.

Namias, J. 1959: Recent seasonal interactions between North Pacific waters and the overlying atmospheric circulation. *J. Geophys. Res.*, **64**, 631-645.

Noble, B. and Daniel, J. W. 1977: Applied Linear Algebra, Prentice-Hall Inc. 477pp.

Oblow, E. M. 1978: *Nucl. Sci. Eng.*, **68**, 332.

O'Connor, J. 1963: The weather and circulation of January 1963. *Mon. Wea. Rev.*, **91**, 209-218.

Oortwijn, J. and Barkmeijer, J. 1995: Perturbations That Optimally Trigger Weather Regimes. *J. Atmos. Sci.*, **52**, 3932-3944.

Orr, W. McF. 1907: Stability or instability of the steady motions of a perfect liquid and of a viscous liquid. *Proc. Roy. Irish Acad.*, **A27**, 9-138.

Parks, C. V. and Maudlin. P. J. 1981: *Nucl. Technol.*, **54**, 38.

Pedlosky, J. 1964: An initial value problem in the theory of baroclinic instability. *Tellus*, **16**, 12-17.

Reinhold, B. B. and Pierrehumbert, R. J. 1982: Dynamics of weather regimes: Quasi-stationary waves and blocking. *Mon. Wea. Rev.*, **110**, 1105-1145.

Rex, D. P. 1950a: Blocking action in the middle troposphere and its effect upon regional climate (I). An aerological study of blocking. *Tellus*, **2**, 196-211.

Rex, D. P. 1950b: Blocking action in the middle troposphere and its effect upon regional climate (II). The climatology of blocking actions. *Tellus*, **2**, 275-301.

Rex, D. P. 1951: The effect of Atlantic blocking action upon European climate. *Tellus*, **3**, 100-112.

Rossby, C.-G. 1950: On the dynamics of certain types of blocking waves. *J. Chinese Geophys. Soc.*, **2**, 1-13.

Roussopolos, R. 1953: Methodes variatiollelles en theories des colisions. *C. R. Acad. Sci.*, **236**, 1858-1860.

Sanders, F. and Gyakum, J. 1980: Synoptic-dynamic climatology of the "bomb". *Mon. Wea. Rev.*, **108**, 1589-1606.

Schubert, M. and Weber, G. 1983: Quantentheorie-Grundlagen, Methoden, Anwendungen. Teil I. VEB Deutcher Verlag der Wissenschaften, Berlin. 270pp.

Shutts, G. J. 1983: The propagation of eddies in diffluent jet streams: eddy vorticity forcing of 'blocking' flow fields. *Quart. J. Roy. Meteor. Soc.*, **109**, 737-761.

Shutts, G. J. 1986: A case study of eddy forcing during an Atlantic blocking episode. *Adv. Geophys.*, **29**, 135-161.

Simmons, A. J. and Hoskins, B. J. 1978: The Life Cycles of Some Nonlinear Baroclinic Waves. *J. Atmos. Sci.*, Oortwbf 35, 414-432.

Simmons, A. J. and Hoskins, B. J. 1979: The downstream and upstream development of unstable baroclinic waves. *J. Atmos. Sci.*, **36**, 1239-1254.

Simmons, A./ J./ and Hoskins, B./ J./ 1980:/ Barotropic influences on the growth and decay of nonlinear baroclinic waves. *J. Atmos. Sci.*, **37**, 1679-1684.

Stern, M. E. 1975: Minimal properties of planetary eddies. *J. mar. Res.*, **33**, 1-13.

Stoker, J. J. 1950: Nonlinear vibrations in mechanical and electrical systems. *Interscience*, New York, 273 pp.

Thompson, P. D. 1957: A heuristic theory of large scale turbulence and long period velocity variations in barotropic flow. *Tellus*, **9**, 69-91.

Thorncroft, C. D., Hoskins, B. J. and McIntyre, M. E. 1993: Two paradigms of baroclinic life-cycle behavior. *Quart. J. Roy. Meteor. Soc.*, **119**, 17-55.

Tibaldi, S. and Molteni, F. 1990: On the operational predictability of blocking. *Tellus*, **42A**, 343-365.

Toth, Z. and Kalnay, E. 1993: Ensemble forecasting at NMC: the generation of perturbations. *Bull. Am. Met. Soc.*, **74**, 2317-2330.

Trevisan, A. and Buzzi, A. 1980: Stationary response of barotropic weakly nonlinear Rossby waves to quasi-resonant orographic forcing. *J. Atmos. Sci.*, **37**, 947-957.

Tung, K. K. and Lindzen, R. S. 1979a: A theory of stationary long waves. Part I: A simple theory of blocking. *Mon. Wea. Rev.*, **107**, 714-734.

Tung, K. K. and Lindzen, R. S. 1979b: A theory of stationary long waves. Part II: Resonant

Rossby waves in the presence of realistic vertical shears. *Mon. Wea. Rev.*, **107**, 735-750.

van Loon, H. 1956: Blocking action in the Southern Hemisphere. *Notos*, **5**, 171-177.

Wallace, J. M. and Gutzler, D. S. 1981: Teleconnections in the geopotential height field during the Northern Hemisphere winter. *Mon. Wea. Rev.*, **109**, 784-812.

White, W. B. and Clark, N. E. 1975: On the Development of Blocking Ridge Activity Over the Central North Pacific. *J. Atmos. Sci.*, **32**, 489-502.

Wigner, E. P. 1945: Effects of Small Perturbations on Pile Period. *Chicago Report*, **CP-G**, 3048.

Yeh, T. C. 1949: On Energy dispersion in the atmosphere. *J. Meteor.*, **6**, 1-16.

Zhang, Z. 1988. The linear study of zonally asymmetric barotropic flows. *Ph.D. thesis*, University of Reading, U. K.

Zou, X., Barcilon, A., Navon, I. M., Whitaker, J., and Cacuci, D. G. 1993: An adjoint Sensitivity Study of Blocking in a Two-Layer Isentropic Model. *Mon. Wea. Rev.*, **121**, 2833-2857.

Vita

Manuel S.F.V. de Pondeca was born in 1962 in Zambezia, Mozambique. He received a Bachelor of Science in Physics from the Eduardo Mondlane University, Mozambique, in 1981. In 1985, he received the degree of *Diplomphysiker*, with a specialization in Theoretical Physics, from the Technical University of Dresden, Germany.